Monitoring Rydberg Wavepacket Dynamics in Calcium Atoms

Matthew Bowden Campbell
Holliston, Massachusetts

B.A. Colby College, 1994

A Dissertation presented to the
Graduate Faculty of the University of Virginia
in Candidacy for the Degree of
Doctor of Philosophy

Department of Physics

University of Virginia
January 2000

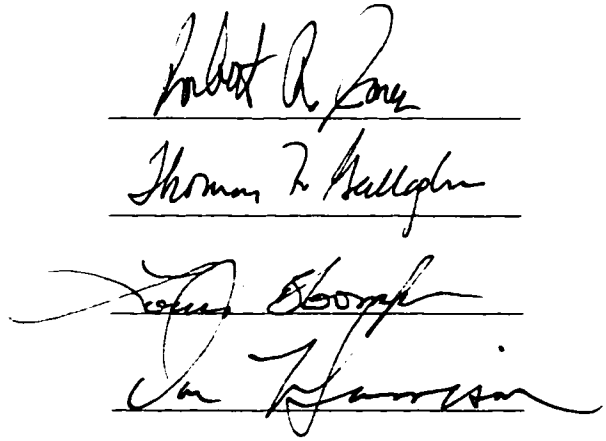

UMI Number: 9954410

UMI Microform9954410

Bell & Howell Information and Learning Company
300 North Zeeb Road
P.O. Box 1346
Ann Arbor, MI 48106-1346

Abstract

This thesis describes a series of experiments involving the excitation and detection of Rydberg wavepacket dynamics using short pulses of electromagnetic radiation. Specifically, we have directly measured the time-dependent momentum-space probability distribution in radial, Stark and continuum wavepackets in calcium by considering the response of the wavepackets to sub-picosecond half-cycle pulses (HCPs). In doing so, we have characterized our experimental technique, observed rapid electic dipole oscillations and discovered a novel way to arbitrarily shape electronic wavepackets. In addition, we have probed the dynamics of a two-electron system and observed oscillations between degenerate bound-state configurations in a rapidly autoionizing atomic state. Each experiment elicits both quantum and classical descriptions, and a discussion of this dual character of Rydberg wavepackets is presented. A newly-developed single-shot imaging detector that allows us to monitor electronic wavepacket dynamics using a single electronic pulse pair has been used throughout. Without this device, the experiments described in this thesis would not have been viable.

Contents

List of Tables

List of Figures

0.1 Acknowledgements

On the eve of my thesis defense, I find it's time to acknowledge the people who have made it possible to reach this point.

First and foremost, I owe everything to Mum and Dad. How can I thank you for allowing me to follow *any* path I desired, for unfailingly supporting the decisions I have made as a student and as a person, and for instilling in me a sense of humor that has kept me going through the tedium of graduate school. *If it is to be, it is up to me.* Well, not without your support!

Andrea, thank you for helping me keep things in perspective. You've always listened to my gripes and kept me positive when my view of physics wasn't so grand. I am very lucky to have you as a sister.

Eileen, you've become a great part of my life during this past year. Thanks for putting up with me during these past few months (and in general), and for all those trips to Schmecky's. I've never had as much fun with anyone as I have with you. La la la.....

To my friends back home, especially Steve and Bri, thanks for making sure we found some beer and golf whenever I made it back to Boston. Steve, congrats on the Ryder cup victory, little less celebration next time. Bri, thanks for taking care of me all this time. It's time I start picking up my own tab (and yours).

Robb and Wallie, thanks for letting me live vicariously through your (mostly) non-academic lives. You've given me confidence that there is life after school.

Thanks to Biff L. and Jim V. for introducing me to noontime and Saturday morning hoops. Thanks to the trailer gang of Chris H., Amanda M., Charles B., Jason K., Elizabeth C., Elena M., and Marcy S. for making the first two years almost bearable. And thanks to Pote, Chris C., Eric M. and Al T. for all the fun at the poker (aka gambling for nickels) table. I must thank Chris H. for teaming up with me to take *two out of three* hoop games from Harold Deane and his buddy.

This work was greatly facilitated by the people around the Physics Department. Thank you Suzie and Pam and Tammie and Teresa and Beverly and Faye and Brenda and Gwen and Lucille and Sybil for all your help with just about everything. There have been no bumps in the road because of your help. Thank you Bobby for helping me find anything I needed. Thank you, Jim, for your help in the library. Thank you Rodger for your help in the shop whenever I asked. Thank you Harvey for all your circuit help and for letting me use the *big* soldering iron. And thank you Tony for letting me earn a little extra spending cash and reminding me of my skill at jobs that require "strong backs and weak minds."

Nathan, thanks for introducing me to experimental atomic physics, and the ways of our lab. I never knew, however, if you were quietly amused or annoyed with my bumbling antics. And, *damn*, you make a mean apple-crisp. Also thanks to lab-mate Tom Bensky, for giving me the inside scoop on how things work in the lab (and warning me to stay clear of two HCP experiments). Your (very patient) computer help was invaluable to me, this thesis would be hand written without your assistance. And thank you Mike Noel and Robert van Leeuwen for many fruitfull discussions.

Without saying, this would not have been possible without the patient guidance of my advisor, Bob Jones. Bob epitomizes the phrase, "lead by example." His ability to figure out why an experiment wasn't working within two minutes of walking into the lab, after I had spent hours or days trying to figure it out, will always amaze me. Thank you, Bob, for your full support and expertise (even with water balloons) during my years here at the University of Virginia.

Chapter 1

Introduction

During the early stages of my scientific studies my eighth grade science teacher, Mr. Hardy, taught us about the structure of atoms. I remember thinking about the semblance between the Bohr atom he described and our solar system and wondering why he never emphasized the similarity. I'm sure my thoughts were quickly diverted by other things. But, after many years, I return to explore the atom/solar system correspondence. More accurately, I study the correspondence between the quantum mechanical nature of an atom and the classical behavior it exhibits after interactions with intense pulses of electromagnetic radiation.

The interaction of atoms with various electromagnetic fields beholds the essence of atomic physics, and progress in this field has directly corresponded to the advancement of the available radiation sources. A milestone in atomic research was the invention of the laser. Continuous wave (cw) lasers produce output that is well suited for spectroscopic studies in atoms. The development of pulsed lasers (lasers that have a time-dependent intensity) generated another surge in research involving the interaction of atoms with light. Strong field phenomena studies, including multiphoton resonances and above threshold ionization due to the AC Stark shift [1], became possible because of the extraordinarily large peak intensities produced in each laser

pulse.

In the past decade technological advances have led to the production of laser pulses with durations measured in tens of femtoseconds (fsec), where 1 fsec $= 10^{-15}$ sec. Again, a new branch of experimental atomic physics (as well as molecular and condensed-matter physics) was born because it became possible to measure dynamic physical systems in the time domain. The short pulse duration is on the order of, or smaller than, the evolutionary time scale of many interesting physical phenomena.

A field of study that has received a tremendous amount of attention from atomic experimentalists and theorists is wavepacket dynamics [2, 3]. A wavepacket is a quantum system that displays a time dependent expectation value for one or more operator [3]. Such a system can be described mathematically as a coherent superposition of two or more non-degenerate eigenstate wavefunctions,

$$\Psi(\vec{r}, t) = \sum_j a_j e^{-\imath(E_j t - \phi_j)} \psi_j(\vec{r}). \tag{1.1}$$

where a_j is the amplitude, E_j is the energy and $\psi_j(r)$ is the wavefunction and ϕ_j is the constant phase for the j^{th} contributing eigenstate. For simplicity, we consider $\phi_j = 0$. The creation of a travelling wave from a superposition of standing waves is demonstrated in Figure 1.1. Each complex phase factor, $e^{-\imath E_j t}$, evolves at a rate proportional to its energy, but the evolution of the wavepacket depends explicitly on the energy differences between contributing eigenstates. As the superposition of waves beat in and out of phase, the physical characteristics of the wavepacket change. Without losing generality, the amplitudes, a_j, and the wavefunctions, $\psi_j(\vec{r})$, are defined to be real. The time dependent probability distribution of the wavepacket is calculated by multiplying the wavefunction by its complex conjugate, $|\Psi(\vec{r}, t)|^2 = \langle \Psi^*(\vec{r}, t) | \Psi(\vec{r}, t) \rangle \propto \sum_j \sum_k a_j a_k \psi_j(\vec{r}) \psi_k(\vec{r}) \cos(\Delta E_{jk} t)$, where $\Delta E_{jk} = E_j - E_k$. The

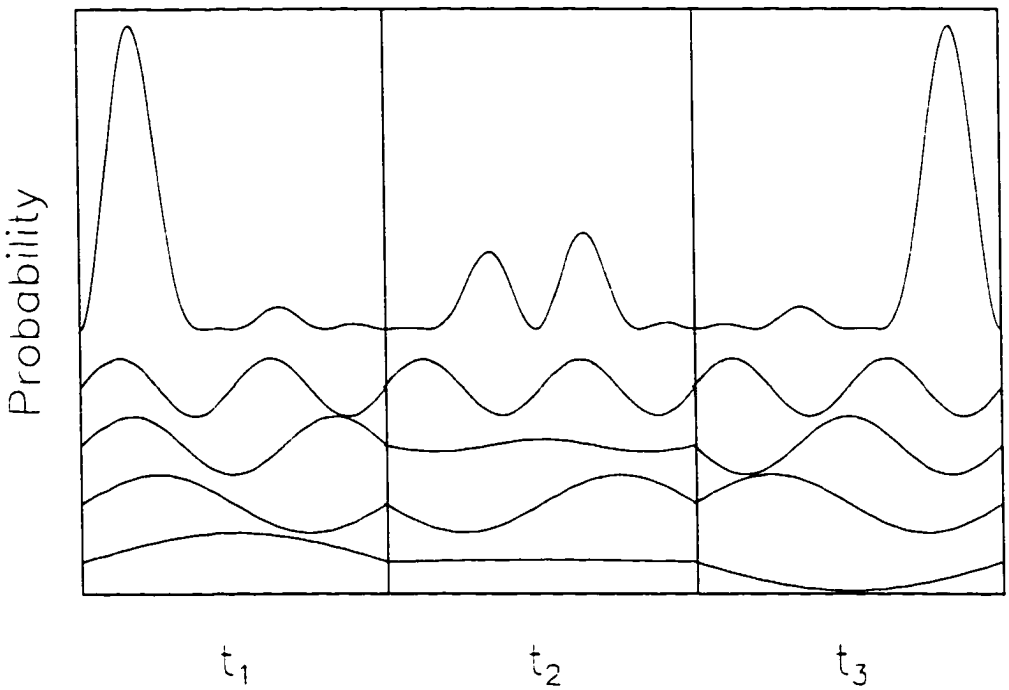

Figure 1.1: A coherent sum of standing waves produces a travelling wave that moves in time. The top curve in each plot shows the probability distribution of the sum of four standing waves at different times, t_1, t_2, and t_3 [4]. The solid lines in the lower curves show the amplitudes of each contributing state at that time, and the dotted line shows the fixed probability of each standing wave.

probability distribution demonstrates a rate of change proportional to the energy differences between contributing eigenstates.

Creating wavepackets requires population transfer from some initial state to a series of final states induced by a radiation source. The dynamics of the wavepacket depend on how many states are involved, the properties of each contributing state and the energy spacing between states. A significant amount of work has involved wavepacket excitation of atoms in (energetically) low-lying states, but the work has proven to be difficult because of the large spacing between adjacent energy levels. The spacing is generally greater than the coherent broadband spectrum of the laser pulses. Nevertheless, experiments have shown that wavepackets may be excited in such systems through resonant ladder systems via multiphoton excitation [5]. Equally spaced eigenstates are excited with a very intense laser pulse, but due to the large energy spacing, usually only two or three bound states contribute to the superposition of states. Another process, which utilizes the AC Stark shift (in which the large oscillating electric field of a high intensity laser pulse mixes states that usually lie outside the laser bandwidth), has produced some interesting results involving enhancement of ionization thresholds in coherently driven systems, but has had limited success creating and detecting bound state wavepackets [6]. In addition, low energy wavepackets have been created in non-degenerate magnetic fine or hyper-fine structure components of low principle quantum number eigenstates and have been monitored using quantum beat spectroscopy [7].

A specific type of electronic wavepacket, a Rydberg wavepacket, has similarly received significant attention, and has generated a surge of experimental and theoretical work starting in the mid-1980's [9]. A Rydberg wavepacket is an atomic system consisting of a superposition of Rydberg eigenstates, where a Rydberg eigenstate is

defined to have a large principle quantum number ($n \geq 15$). Rydberg wavepackets are excellent candidates for experiments probing the dynamics of atomic systems and investigating the manipulation of the electronic wavefunction with electromagnetic radiation. First, Rydberg states have exaggerated properties [8] (see Table 1.1), so Rydberg wavepackets are generally susceptible to strong perturbations produced by moderate-to-strong applied fields. The number of states in an atom for a given n-

Property	n-dependence	n=30	n=1
binding energy	$1/n^2$	-121.9 cm^{-1}	-109737.3 cm^{-1}
outer turning point	n^2	1800 a.u.	2 a.u.
field ionization level	$1/n^4$	400 V/cm	320 MV/cm
orbital period	n^3	4.1 psec	< fsec

Table 1.1: Scaling of different properties as a function of principle quantum number, n. Columns 3 and 4 compare values for n=30 and n=1 hydrogen eigenstates, respectively.

state increases by a factor of n^2, therefore, many more opportunities for multiple state excitation exist. Also, the energy of each eigenstate with principle quantum number, n, varies as $1/n^2$, which leads to energy differences between adjacent eigenstates proportional to $1/n^3$. The orbit period of a wavepacket made up of differing n-states, but having identical angular and azimuthal (ℓ and m) quantum numbers, scales as the inverse energy difference of the contributing states (n^3). This is identical to the Kepler orbit period ($\tau_{Kepler} = 2\pi n^3$) of a classical electron that has the energy of the n^{th} eigenstate in a $1/r$ Coulomb potential. Hence, the evolutionary time scale for Rydberg wavepackets is measured in picoseconds, which is significantly longer than the $\sim$ 100 fsec to $\leq$ 1 psec strong radiation pulses that are now easily created in the laboratory. The short pulses of radiation act as fast 'shutters' that capture the motion of these dynamic systems.

Creation of Rydberg wavepackets can be viewed in both the time and frequency

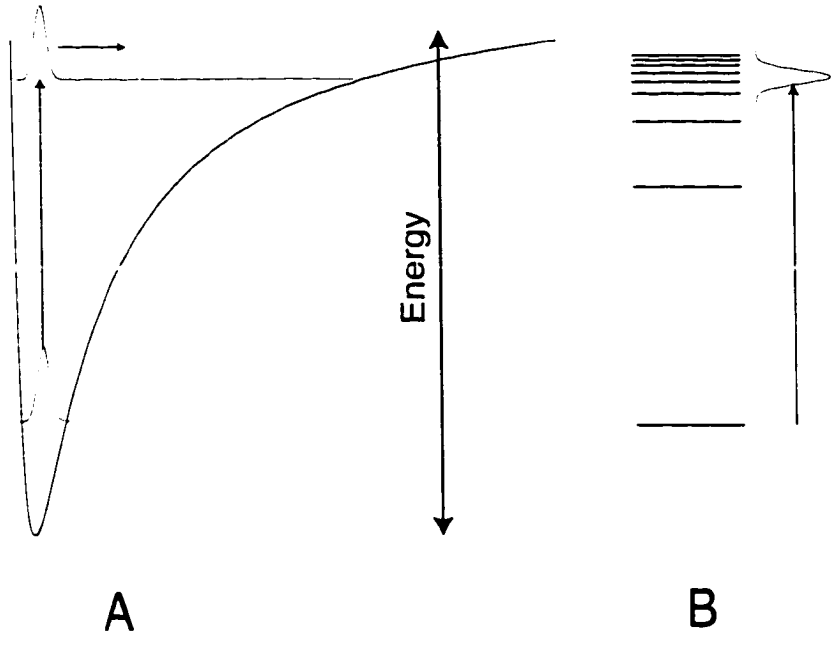

Figure 1.2: Excitation of a Rydberg wavepacket as viewed in the A) time domain, in which the initial state character is preserved due to the short duration of the excitation pulse so it is free to expand and fill this 'new' potential, and B) frequency domain, in which there is sufficient coherent bandwidth in the short pulse to excite several eigenstates, creating a non-stationary superposition of states.

domain. In the time domain, a short laser pulse rapidly excites a wavepacket from its initial state to a coherent superposition of final states. The wavepacket retains strong initial state 'character,' and has not had time to spread out into the accessible volume of its contributing eigenstates. Figure 1.2A depicts a cartoon of the excitation of a Rydberg wavepacket represented in the time domain. The manner in which the wavepacket loses its initial state character and evolves in its new potential is determined by the states that make up the wavepacket. In the frequency domain, the short laser pulse used in wavepacket excitation has sufficient coherent bandwidth to simultaneously excite several eigenstates, creating a Rydberg wavepacket. This viewpoint of wavepacket excitation is shown in Figure 1.2B.

The advent of ultrashort laser pulses has made the creation and detection of

Rydberg wavepacket dynamics possible, and there are three primary reasons why the study of Rydberg wavepacket is interesting. Studying Rydberg wavepackets helps us

- bridge the gap between the quantum and classical behavior of matter [9],
- probe strong field phenomena and complicated electronic state distributions, and
- test various methods of quantum control over dynamic systems [10, 11].

Time domain measurements follow the classical concept of observing the trajectory (orbit) of a localized wavepacket [10, 9, 11]. Spectroscopic measurements are ideal for measuring the energy of the contributing states of a quantum system, but monitoring some time dependent characteristic of the system (*e.g.* how much the system resembles its initial state at some point in time using the optical Ramsey method [3], ORM, or the time-dependent momentum-space probability distribution, using impulsive momentum retrieval [3], IMR) provides a much more complete description of the processes involved in Rydberg wavepacket creation and detection.

Many approaches to studying the similarities and differences between classical and quantum mechanics exist [10]. The correspondence between quantum and classical mechanics is observed in the example of Rydberg wavepacket ionization due to subpicosecond, unipolar strong electric field pulses [12]. Quantum mechanically, the problem is approached by solving the time-dependent Schrödinger equation with a time-dependent Hamiltonian, $H(t) = H_{atom} + F(t)z$, where H_{atom} is the one-electron Hamiltonian of the atom and $F(t)$ is the time dependent electric field. The Schrödinger equation can be solved numerically but the inclusion of a prohibitively large basis set of $n,\ell,\ m$ and continuum states is essential to determine the total energy of the electron after its interaction with the field pulse [12, 13]. My interpretation of the

interaction of a short, unipolar electric field pulse with a Rydberg electron is that the rapid turn-on of the electric field mixes the initial eigenstate of the electron with thousands of other available states. The field quickly turns off and leaves the system in a confusing distribution of final states, some of which are unbound.

In contrast, however, the interaction between a short half-cycle pulse (HCP) and a Rydberg electron can be viewed classically as uniform momentum change of the electron in the direction parallel to the field pulse. The electron-HCP interaction is analogous to the firing of a booster rocket on a satellite orbiting the earth [14]. The rocket changes the energy and momentum of the satellite, leaving it in a new orbit that is potentially no longer bound by the earth's gravitational pull. After the electron interacts with the HCP, its energy changes by an amount that depends on its momentum component along the field polarization axis at the time of the interaction, and is given by $\Delta E = A^2/2 + \vec{p}_o \cdot \vec{A}$, where $\vec{A}$ is the impulse delivered to the electron by the HCP ($\vec{A} = -\int_{-\infty}^{\infty} \vec{F}(t)dt$), and $\vec{p}_o$ is the initial momentum of the wavepacket. If ΔE is greater than the binding energy, the electron is free to leave the atom and an ion is formed.

Although both methods of analyzing the interaction between the HCP and electron involve calculations of the final energy of the electron and provide accurate results [12], the ionization process seems much more intuitive classically because we live in a classical world.

Although wavepackets can be produced with a short burst of white light (*all* you need is bright light bulb and a chopper wheel that spins at 100 MHz), reproducible creation of specific wavepackets that exhibit desired behaviors is a formidable challenge. Because Rydberg wavepackets generally have well defined initial and final bound and continuum states, they are strong candidates as systems that can be

controlled with radiation. Interactions between charged and neutral particles and atoms are controlled with electromagnetic forces, and it is now possible to mimic a wide array of particle interactions with radiation pulses. Understanding how even a small subset of dynamic atomic systems (Rydberg wavepackets) reacts to various electromagnetic pulses is essential for building the foundation of studies concerning the coherent control of atomic and molecular systems with radiation.

This thesis describes several experiments involving the creation and detection of Rydberg wavepacket dynamics. From these experiments we have learned about current experimental capabilities concerning what information can be extracted from evolving atomic systems. We have also made discoveries involving the ability to arbitrarily place charge distribution on specific points about an atom and using Rydberg wavepackets as novel sources of radiation. The work presented here attempts to add to the growing body of knowledge pertaining to the interaction of matter with electromagnetic radiation, which will someday enable the arbitrary manipulation of atomic and molecular wavefunctions with light.

The thesis is organized as follows. Chapters 2 and 3 describe the experimental apparatus used throughout the experiments, including a single-shot delay-range imaging detector that was essential in facilitating time-domain measurements. Four experiments involving Rydberg wavepackets in calcium are presented in Chapters 4-7. In Chapter 4, the evolution of radial wavepackets is studied and direct measurements of localized radial wavepacket 'breathing' are shown and explained. The experiment in Chapter 5 monitors the dynamics of a Stark wavepacket, in which radial and angular oscillations are observed along with a full quantum mechanical analysis of the system. Chapter 6 discusses an experiment in which the dynamics of a continuum wavepacket are probed, enhancing the link between the simultaneous classical and quantum na-

ture of Rydberg wavepackets. The experiment presented in Chapter 7 monitors the dynamics of a system in which both valence electrons in calcium are excited, adding to the knowledge of electron- electron interactions and configuration swapping, which may play a key role in optical control of atoms and molecules. Concluding remarks are made in Chapter 8.

Bibliography

[1] T.S. Luk, T. Graber, H. Jara, U. Johnson, K. Boyer and C.K. Rhodes, *Opt. Soc. Am. B* **4**, 847 (1987). R.R. Freeman, P.H. Bucksbaum, H. Milchberg, S. Darack, D. Schumacher and M.e. Geusic, *Phys. Rev. Lett.* **59**, 1092 (1987).

[2] L.D. Noordam and R.R. Jones, *J. Mod. Opt.* **44**, 2515 (1997).

[3] R.R. Jones and L.D. Noordam, *Advances in Atomic, Molecular and Optical Physics* **38**, 1 (1997).

[4] This figure is adapted from Robert R. Jones, *McGraw Hill 1998 Yearbook of Science and Technology*, p 429 (1997).

[5] B. Broers, H.B. van Linden van den Heuvell and L.D. Noordam, *Phys. Rev. Lett.* **69**, 2062 (1992). P. Balling, D.J. Mass and L.D. Noordam, *Phys. Rev. A* **50**, 4276 (1994). R.R. Jones, *Phys. Rev. Lett* **75**, 1491 (1995).

[6] R.R. Jones, D.W. Schumacher and P.H. Bucksbaum, *Phys. Rev. A* **57**, R49 (1993). J. Parker and C.R. Stroud, Jr., *Phys. Rev. A* **41**, 1602 (1990).

[7] W. Demtroder, *Laser Spectroscopy*, 2^{nd} ed., Springer-Verlag, New York (1982).

[8] Thomas F. Gallagher, *Rydberg Atoms*, Cambridge University Press (1994).

[9] G. Alber, H. Ritsch and P. Zoller, *Phys. Rev. A* **34**, 1058 (1986).

[10] Ivan Amato, *Science* **273**, 307 (1996). Paolo Bellemo, C.R. Stroud. Jr., David Farrelly and T. Uzer, *Phys. Rev. A* **58**, 3896 (1998).

[11] Warren S. Warren, Herschel Rabitz and Nohammed Dahleh, *Science* **259**, 1581 (1993). J. Parker and C.R. Stroud. Jr., *Phys. Rev. Lett* **56**, 716 (1986).

[12] F. Robicheaux, *Phys. Rev. A* **56**, R3358 (1997).

[13] R.R. Jones, D. You and P.H. Bucksbaum, *Phys. Rev. Lett.* **70**, 1236 (1993). G.M. Lankhuijzen and L.D. Noordam, *Advances in Atomic, Molecular and Optical Physics* **38**, 121 (1997).

[14] Bart Noordam, *Physics World*, p 22, December, 1997.

Chapter 2

Experimental Apparatus

2.1 Introduction

The experiments described in this thesis investigate the interaction of atoms with intense, short bursts of electromagnetic radiation. The apparatus and techniques used in these experiments are discussed in this chapter, with a focus on operational methods. This chapter attempts to serve as a guide to the laser systems and data acquisition systems for people being introduced to the laboratory.

Section 2.2 describes the different lasers used in the laboratory, including a self mode-locked, regeneratively amplified 120 fsec laser pulse source, as well as Nd:YAG pumped tunable dye-lasers. The lasers provide coherent ultraviolet (UV), optical and infrared wavelength pulses that are used to drive atomic transitions. Additionally, the evolution of non-stationary states in atoms can be probed with a novel source of nearly uni-polar pulses of THz radiation, or half-cycle pulses (HCPs). Section 2.3 explains the method for creating this useful radiation source. All work is performed in a vacuum system that maintains a pressure of $\sim 10^{-6}$ torr. The low pressure ensures that experiments are not contaminated with atoms or molecules other than those of interest. Sections 2.4 and 2.5 describe the make-up of the vacuum system and the

source of a thermal beam of atoms in which the experiments are performed. Essential tools used for making measurements are described in Section 2.6.

2.2 Lasers

Two important laser systems are used in the lab. The first system generates ultrashort laser pulses necessary for time-domain measurements of Rydberg wavepackets. The output of this system is a 450 mW, 15 Hz train of $\sim$ 120 fsec, 786 nm optical pulses. The peak power of each pulse is measured in TWatts and delivers the intense fields required in this research field. The second laser system is used to drive transitions between specific eigenstates in atoms. An array of tunable dye-lasers deliver 5 nsec pulses at a 15 Hz repetition rate over a broad frequency spectrum, ranging from UV to visible to infrared. This section explains the components of these two systems and provides some background which will (hopefully) make the operation and setup of each system more understandable.

2.2.1 Nd:YAG Laser

The work horses in the lab are two pulsed neodymium-doped yttrium aluminum garnet (Nd:YAG) lasers. The output of these Nd:YAG lasers provides the energy for the operation of several other lasers in the lab. One Nd:YAG laser pumps the short pulse regenerative amplifier and multi-pass amplifier used in ultrashort pulse generation, while the other pumps a number of dye lasers.

The Nd:YAG laser produces < 5 nsec, 1064 nm laser pulses at a 15 Hz repetition rate with a time-averaged power of $\sim$ 10 W, meaning $\sim$ 0.65 joules are delivered with each pulse [1]. Two Nd:YAG rods are used in laser pulse production. One rod serves as the initial gain medium for the pulse, while the other is used for pulse amplification.

Each Nd:YAG rod is positioned at one focus of an elliptical cavity and is pumped with a flash lamp located at the opposite focus.

Without the ability to control when light enters or leaves the laser cavity, the laser would emit pulses with a much lower peak power and have a longer duration that matches the flash lamps. However, the pulse duration is short, and the power is strong as a result of Q-switching. Large gain is stored in the Nd:YAG rod due to high cavity loss introduced by an electro-optical Q- switch. The Q-switch consists of a polarizer, a quarter-wave plate, and a Pockels cell. With zero voltage applied to the Pockels cell, any light in the cavity is reflected out of the cavity by the polarizer after two passes through the quarter-wave plate. When the Q-switch is triggered, the Pockels cell offsets the polarization effects of the quarter wave plate, so light remains in the cavity. The extra large population inversion is quickly depleted, and a short, high power pulse is emitted from the laser [2].

The high power Nd:YAG 1064 nm beam enables efficient second and third harmonic generation in non-linear potassium dihydrogen phosphate (KDP) crystals positioned just outside the output window of the laser. Most dye-lasers in the lab are pumped with frequency doubled 532 nm (green) light or frequency tripled 355 nm (UV) light. Ti:sapphire crystals readily absorb at the 532 nm harmonic of the Nd:YAG laser [3].

The Nd:YAG lasers are run at full power during experiments. This prevents fluctuations in the timing of the output beam. The laser intensity is controlled using beam splitters, half-wave plates and thin film polarizers as variable attenuators.

The power may be turned down most of the way for beam alignment and beam quality checks. The Nd:YAG lasers power up and run reliably in about a minute. The power output of the laser is measured with a power meter sensitive to 532 nm

wavelength light. Sudden changes in laser output indicate a problem that must be addressed. The power output of the 532 nm harmonic is monitored day to day with a power meter and is a key indicator of proper laser function. The flash lamps need to be replaced after about 700 running hours (usually every 3 or 4 months). Also, the de-ionized cooling water reservoir in each Nd:YAG laser should be checked periodically to make sure the level remains in the normal operation range.

2.2.2 Ultrashort Laser Pulse System

The driving force behind the experiments described in this thesis is the short-pulse laser system. The laser produces 786 nm, 120 fsec at a 15 Hz repetition rate with a time averaged power of up to 600 mW. The evolutionary time scale of atomic Rydberg states is on the order of picoseconds, so 120 fsec laser pulses provide a fast 'shutter' necessary to observe dynamics in the time domain. The intense fields of each laser pulse interact with atoms for a time shorter than the classical Kepler orbit period of Rydberg atoms. Therefore, the Rydberg wavepacket is (approximately) frozen during the interaction, and information about the wavepacket's orbit at that specific time is extracted with various methods (the optical Ramsey method and impulsive momentum retrieval). The extremely brief pulse duration is noteworthy. The Earth, which is hurtling through space at nearly 30000 m/sec relative to the sun, travels the diameter of large atom in 120 fsec.

Argon-Ion Laser

Ultra-short laser pulses are generated with a titanium-sapphire self mode-locked laser. Our lab uses a modified Spectra-Physics Model 3900S laser system, which is pumped with blue-green light emitted by a Coherent Argon- Ion (Ar^+) laser. The Ar^+ laser is capable of producing upwards of 10 Watts of cw light predominantly at 488 nm and

514.5 nm wavelengths [4]. In the ion laser, a large flux of electrons flowing through and colliding with a sample of argon atoms creates Ar^+ atoms in a range of ionic states. Lasing occurs between the $4p$ and the $4s$ ionic states of the argon atoms. One electron may send the argon atom to the ionic ground state or to some metastable ionic state. A second electron excites the ion to an upper level (4p) ionic state. The electron spontaneously emits a laser photon as it falls to the 4s state. The 4s state is short lived ($\sim 10^{-9}$ sec), and the electron quickly drops to the Ar^+ ground state [5]. The current density of electrons through the plasma controls the power output. Generally, the ion laser operates with an output power between 7 and 8 W, depending on the mode being used in the Ti:sapphire laser. The current flowing through the Ar^+ tube is controlled with a remote box located next to the laser on the optics bench.

The argon plasma is contained in a long ($\sim$ 1 m) thin tube with a $\sim$ 1 cm diameter. The ends of the tube are cleaved at the Brewster angle. The tube is positioned so the flat side of the output window faces up. This design makes the window easier to clean, but contiminants may settle on the window during laser operation and potentially fuse to the surface. Thus, laser beam quality is severely impaired. To determine the presence of contaminants on the window, turn the laser to low power and look at the surface of the output Brewster window of the Ar^+ tube. If there is a large amount of scattered light from the window surface, deposits may be present on the window. The window may be carefully cleaned with ammonium bi-fluoride. This rather pungent chemical eats away at the surface of the window and removes the contaminants. The chemical is destructive and must not remain on the ion tube for more than a minute or so. A couple drops of ammonium bi-fluoride are applied to an optics quality tissue that has been folded and clamped into a pair of locking forceps. Gently drag the tissue across the window of the ion tube once or twice, applying the cleaning chemical. After

one minute, remove the ammonium bi- fluoride with de-ionized water applied to a new, similarly folded optics tissue. Apply a couple drops of water to a folded tissue and carefully drag the tissue across the window. Rinse the window with water two or three times to make sure there is no ammonium bi-fluoride remaining on the surface. Finally, the window must be rinsed with optics quality methanol. Apply a few drops of methanol to an optics tissue, then wipe the window surface. The methanol wash may be applied two or three times. Replacement of an Ar^+ tube is costly (a new one can cost $20.000), so it is important not to damage the window while cleaning.

The Ar^+ laser takes about 15-25 minutes to warm up and supply a high-quality laser beam to the Ti:sapphire laser. After it is turned on, the current through the ion tube should be adjusted to the normal operation level for the desired power output (typically 53-56 A for $\sim$ 8 W). After warming up, the output quality can be enhanced by setting the remote box to 'tune' and adjusting the two knobs for the mirror at the back of the laser cavity. Once optimized, hit the 'tune' button again to return the laser to self-controlled alignment. The Ar^+ tube has exceeded its expected running lifetime of 3000 hours; however, it continues to provide a sufficient beam to achieve mode-locking in the Ti:sapphire laser. The laser may exhibit signs of age in a few ways. First, a consistent 'High Cathode' error occurs the first time the laser is turned on each day. Usually, after a couple of minutes, the laser will turn on without error. Second, more current is required to extract the needed power out of the laser. While this dissertation was being written the tube was replaced, so this discussion won't be applicable for several years.

Overheating the laser is prevented by a water cooling line connected to a self-contained heat exchange system. The heat exchanger is preferably connected to the laboratory in-house chilled water loop or (if there are problems with the chilled water)

tap water lines. The outside source of water is controlled with standard T-valves. When operating properly there should be about 3.2 gallons/minute flowing through the laser cooling line. The heat exchanger should stay on after the Ar^+ laser has been turned off until the temperature of the water leaving the laser is the same as the water entering the laser ($\sim 70^oF$), which should take about ten minutes. During operation the temperature of the water leaving the laser is about 100^oF.

Ti:sapphire Self Mode-Locked Laser

The Ti:sapphire self mode-locked laser provides a 78 MHz train of 100 fsec, 1 nJ pulses of 786 nm light. The laser consists of an optical cavity with a centrally located gain medium as well as an output coupler and group velocity dispersion correction optics [3, 6]. A schematic of the mode-locked laser is shown in Figure 2.1.

The Ti-sapphire crystal acts as the broadband gain medium in the laser and has emission lines ranging in wavelength from 600 nm to 1000 nm [7]. The crystal can sustain upwards of 100,000 longitudinal modes in the laser cavity, and the fixed cavity length ensures each mode is equally spaced in frequency [7]. If all modes, which are generated with a coherent source, are perfectly in phase, the electric fields of the waves add constructively at one point. This phenomenon is referred to as mode-locking or phase-locking. To demonstrate this effect, Figure 2.2 shows the sum of 100 cosine waves that are evenly spaced in frequency for both a random distribution of relative phases and a mode-locked phase distribution. The random phase superposition of fields is scattered, whereas the mode-locked sum of waves has large spikes spaced at $2\pi/\Delta$ ($\Delta = c/2L$ is the frequency spacing between modes defined by the laser cavity round trip length, where c is the speed of light and L is the length of the cavity), representing intense, short bursts of light. The bursts would be more discernable from

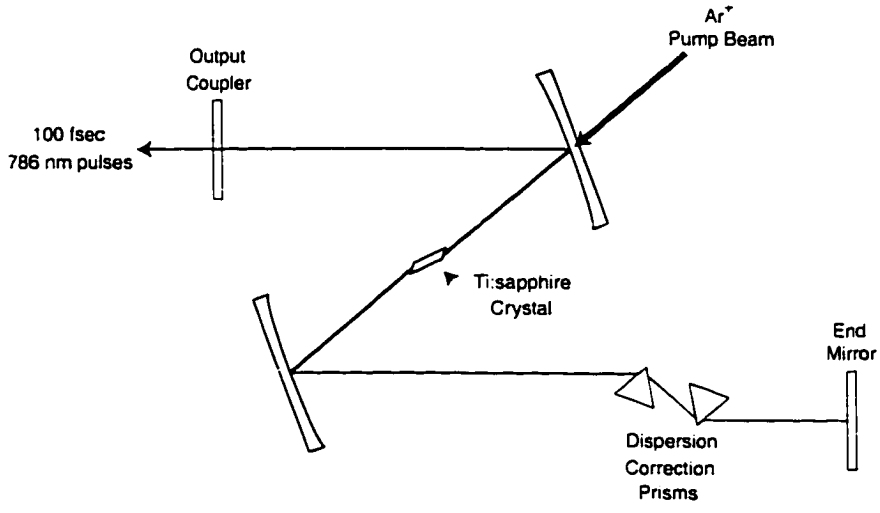

Figure 2.1: Schematic diagram of self mode-locked Ti:sapphire laser cavity [3].

the random phase field if 10^5 modes were included, especially for the intensity profile which is proportional to the sqare of the time dependent field. The output coupler of the laser cavity has been repositioned outside the laser container to extend the round trip length of the laser to about 3.8 m. A pulse of light is emitted for each round trip in the laser cavity at a $\nu = c/d \approx 78.MHz$ repetition rate, where c is the speed of light and d is the round trip cavity length.

The objective of this work is not to explain the details of mode-locking, but to simply describe the necessary components and functions of our laser system. The Ti-sapphire laser is configured to act as a self-mode-locking device, implying the laser is most energetically stable when mode-locked. The Ti:sapphire rod is pumped with the light emitted by the Ar^+ cw laser and re-emits light over a broad frequency range. Sufficient bandwidth sustains upwards of 100.000 modes in the laser cavity. When the modes are phase- or mode-locked, the combination of fields creates very brief high intensity field spikes.

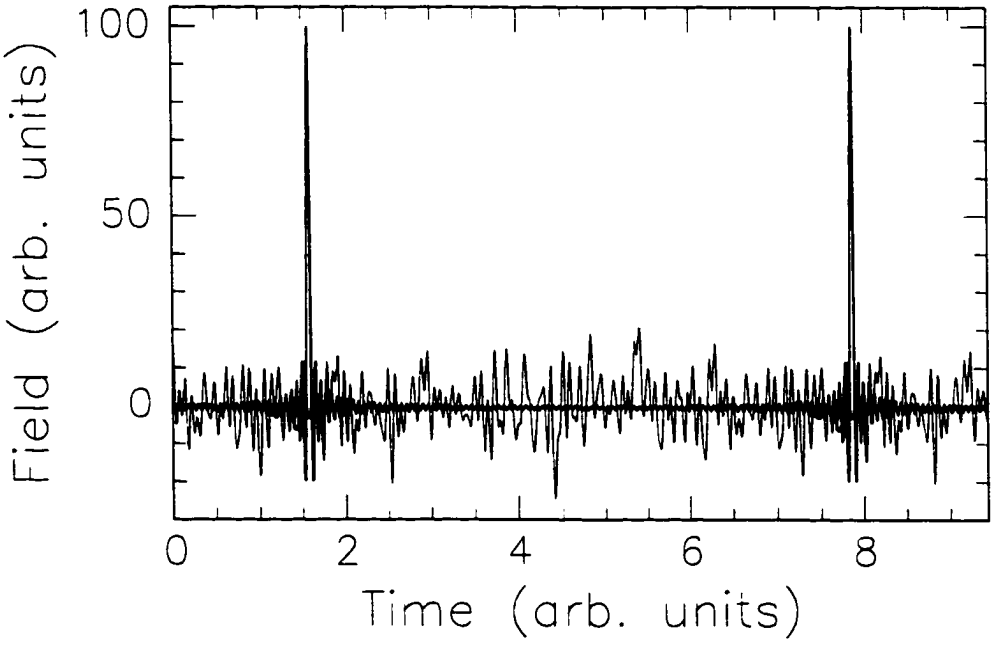

Figure 2.2: Plot of the sum of 100 different cosine waves equally spaced in frequency. The bold curve waves are all perfectly in phase producing sharp peaks spaced by $2\pi/\Delta$, where Δ is the frequency spacing and is equal to one. The phases in the second curve are randomized, producing a scattered sum.

The intensity dependent refractive index of Ti:sapphire, stemming from the large non-linear Kerr effect, has constructive and destructive effects on sustaining mode-locking in the crystal. The intensity dependence means the index of refraction varies spatially and temporally in the crystal during the short pulse. Self-phase modulation due to the time dependence of the index of refraction produces a frequency chirp in the pulse. Different components of the pulse propagate through the crystal at different rates, resulting in group velocity dispersion. A prism pair is placed in the laser cavity to compensate for this effect. Spatial variation of the refractive index causes lensing effects in the Ti:sapphire crystal and promotes self focusing. Kerr lensing makes the short pulse match the cavity for more stable operation.

The initiation of mode-locking occurs through the accumulation of oscillations in the cavity due to slight noise fluctuations in the electric field until saturation of the absorber is reached. A spike in the background noise is introduced to the cavity by gently shaking the output coupler that is mounted on an adjustable delay stage. The electric field spike oscillates in the laser cavity and the Ti:sapphire crystal preserves its characteristics with each pass. With successive trips through the crystal, the intensity of the spike increases and intensity dependent refractive index effects predominate, resulting in mode-locking.

Once mode-locked, the Ti:sapphire emits a train of 786 nm, 100 fsec pulses that leave the laser at a 78 MHz repetition rate and has a time-averaged power of $\sim$ 100 mW. Rotation of a single birefringent crystal plate in the laser cavity adjusts the central frequency of the output beam. A small portion of the mode-lock output reflects from a glass microscope slide and is sent to a fast photodiode. The output of the photodiode is displayed with an analog Tektronix oscilloscope. When the laser is properly mode-locked, a stream of uniformly spaced, fixed amplitude spikes is observed. Some-

times, the Ti:sapphire laser sustains more than one mode simultaneously, resulting in interspliced peaks from the different modes.

The Ti:sapphire laser is highly sensitive to its environment and can easily fall out of mode-lock. A sudden vibration can knock the laser out of mode-lock as easily as it can initiate mode- locking. To damp out unwanted vibrations, the laser is mounted on the floating optics bench. The most prevalent cause for the laser to stop running in a mode-locked state is temperature fluctuations. The lifetimes of the excited states in Ti:sapphire are highly sensitive to temperature, and changes in temperature lead to variations in amplitude and temporal characteristics of the sustainable mode(s) of the crystal. Also, mirror mounts change shape with temperature fluctuations, which leads to unwanted beam steering.

A water line runs through the laser to maintain a constant temperature in the Ti:sapphire crystal. A small heater maintains the water reservoir's temperature a few degrees above room temperature. The air temperature above the optics table is similarly regulated. The optics table is enclosed in a clear plastic tent and air is blown into the region above the table through two vents. The resultant air pressure gradient ensures air flows out from under the plastic walls. An electric space heater connected to a thermostat is located near the air intake of the vent nearest the Ti:sapphire laser. A thermometer centrally positioned on the optics table provides feedback to the thermostat to control heat delivery. By setting the temperature a few degrees Fahrenheit higher than room temperature, the temperature of the air above the optics table remains constant with $< 1^{o}F$ fluctuation. The temperature of the lab must be kept relatively low (a surprisingly chilly $70^{o}F$) to ensure the air temperature above the optics bench is not too high.

Laser Pulse Amplification

The power output of the Ti:sapphire self-mode-locked laser is about 100 mW, and each pulse carries about 1 nJ of energy. This type of beam is useful in many applications, but does not provide the great peak intensities desired for this research. Experiments are synchronized with the Nd:YAG lasers that run at 15 Hz. Therefore, we amplify 15 out of every 78 million short pulses generated by the Ti:sapphire laser. Using the sequence of steps described below, the pulses are amplified by a factor of $\sim 10^7$, producing very intense short laser pulses.

Pulse Expander

Amplification of the 786 nm, 100 fsec laser pulse output of the mode-locked laser is performed in a Ti:sapphire crystal. The intensity of each pulse is greatly increased during amplification because the area of the beam must remain smaller than the 4 mm $\times$ 5 mm face of the crystal. As discussed earlier, the Ti:sapphire crystal and various optical components have intensity dependent properties that may distort the short pulses' characteristics during amplification through self-phase modulation. Therefore, each short laser pulse is 'stretched in time' to preserve beam quality during amplification and prevent damage to optical components. The short laser pulse has a large frequency spectrum, and in the stretching, or expanding process, different frequency components follow different geometric path lengths. The lower (red) frequencies travel a shorter distance than the higher (blue) frequencies, creating a frequency chirp in the pulse. Using a pulse expander, the pulse duration is (reversibly) increased to about 2000$\times$ its original 100 fsec length. The increase maintains the time-averaged power of the pulse, but greatly reduces its peak power.

The pulse expander consists of a high-grade diffraction grating, lens, and two mir-

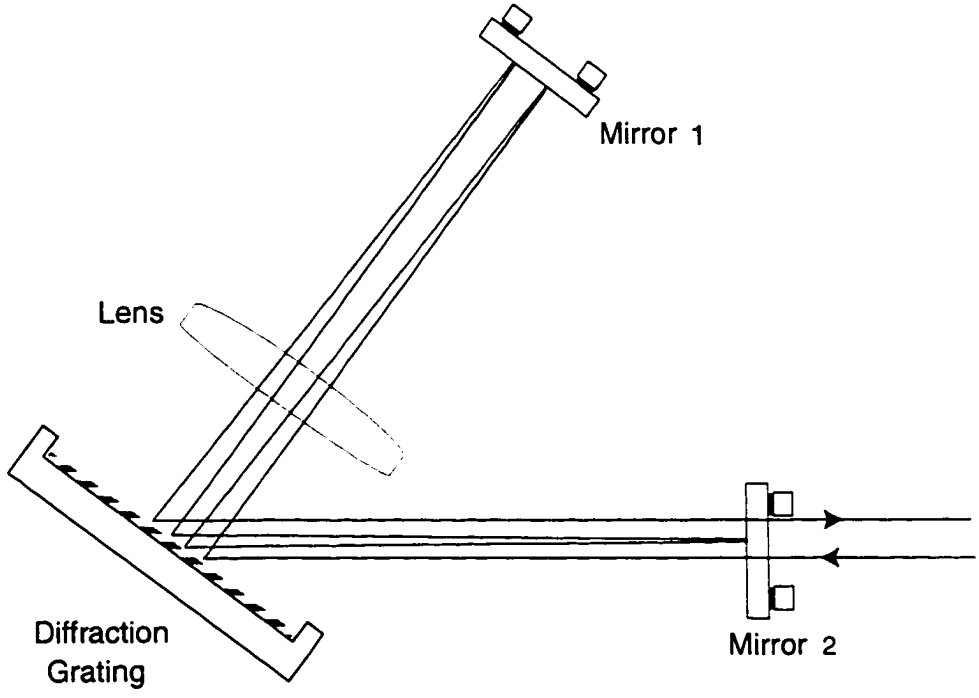

Figure 2.3: Layout of the short laser pulse expander. The beam diffracts four times off the diffraction grating. The beam path is offset in the plane of the page for clarity. Each pass off the grating spatially separates different frequencies contributing to the beam.

rors. A schematic of the expanderer is shown in Figure 2.3. Incident light approaches the expander just above Mirror 2 and diffracts from the grating positioned at $\sim 54^o$ with respect to the incident beam propagation direction. Different frequencies of light diffract at different angles ($\sin\theta = \lambda/2d$, where λ is the wavelangth and d is the spacing between lines of the grating) and travel towards Mirror 1. The lens placed between the grating and Mirror 1 produces an enlarged-chirped image of the input beam on the expanding grating and establishes a purely geometrical path difference that the extrema of the dispersed frequencies follow throughout the expansion process. The pulse is reflected back towards the diffraction grating and is diffracted back to Mirror 2. The pulse is retro-reflected towards the grating and the sequence repeats. The multiple reflection path off the diffraction grating expands the pulse in time because the geometric path length for each frequency component is different. The beam walks out of the loop and is emitted (vertically translated with respect to the incident beam above Mirror 2) after striking the grating four times. Thus, the laser pulse is frequency chirped as different frequency components of each laser pulse arrive at different times. This process stretches each pulse to about 2000 times its original length, making the pulse suitable for amplification. Once amplified, the laser pulse can be 'un-chirped' by the reverse process in a beam compressor, returning the pulse duration to $\sim$ 120 fsec.

Figure 2.4 shows a schematic diagram of the pulse compressor. The beam is diffracted off an identical grating four times to reverse the stretching process. The retro-reflecting mirror pair is mounted on a translation stage to allow adjustments of the relative geometrical path length for the different frequency components. The chirp in the exiting pulse is then easily controlled. The output pulse width is sensitive to slight adjustments to the position of the translation stage.

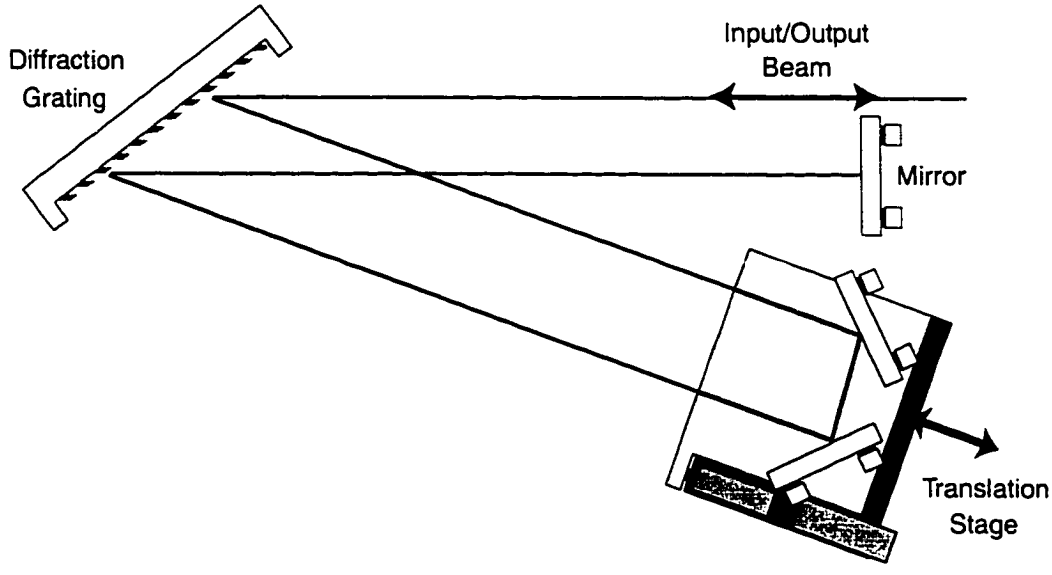

Figure 2.4: Layout of the laser pulse compressor. Similar to the expander, the beam makes four passes off the diffraction grating.

The final pulse width is measured with a single-shot autocorrelator. Portion of the beam is split and sent through a frequency doubling crystal. The two beams propagate at a small relative angle through the crystal, and doubled frequency light is produced in the crystal when the two beams are spatially overlapped in time. The width of the doubled frequency light beam corresponds to the length of the beam are overlap, which is a function of the original pulse length. A linear CCD array detects the width of the doubled frequency stripe. The width is scaled to time by observing the offset of the stripe in the crystal when a glass slide (which delays the pulse by a known amount, $\Delta t = \frac{d}{c}(n-1)$, where d is the thickness of the glass, c is the speed of light in air and n is the index of refraction of the glass) is placed in the path of one of the input beams.

Regenerative Amplifier

Experiments involving the creation and detection of wavepacket dynamics require high power, ultrashort laser pulses. A regenerative amplifier (Re-gen), combined with a multi-pass amplifier, increases the energy of the 786 nm, 1 nJ, 200 psec laser pulses by a factor of about 10^7. Peak power on the TWatt scale is available once the pulses are compressed to $\sim$ 120 fsec.

A diagram of the Re-gen is shown in Figure 2.5. Energy gain in the Ti:sapphire crystal is provided by a 532 nm, 5 nsec pulse from an Nd:YAG laser. The pulse repetition rate for the Nd:YAG laser is 15 Hz, and the energy storage time of the Ti:sapphire crystal is 3×10^{-6} sec [3]. Therefore we only amplify 15 out of every 78 million mode-locked laser pulses. The uniform disk spatial mode output of the Nd:YAG laser is imaged onto the Ti:sapphire crystal with a 500 mm lens, optimizing the uniformity of the gain to be swept out by the short pulse.

The amplification process begins when a short pulse (although expanded to $\sim$200 psec) reflects off a thin film polarizer (TP1) through a Pockels cell, PC1. The Pockels cell is triggered to change the polarization of the pulse 45^o during its initial pass, and another 45^o after it returns from mirror M1. The pulse now transmits through TP1 and oscillates in the laser cavity. PC1 is synchronized to the Nd:YAG laser and prevents additional pulses from entering the cavity at the same time.

The injected pulse repeatedly passes through the Ti:sapphire crystal, sweeping out gain with each pass. After about 17 passes, the energy in the pulse saturates. The pulse is then switched out of the Re-gen with a second Pockels cell, PC2, and thin-film polarizer, TP2, pair. The delay between the triggering of PC1 and PC2 determines how long the pulse remains in the Re-gen cavity. The intensity of the amplified pulse, hence the buildup in the Re-gen cavity, is monitored with a photodiode. The

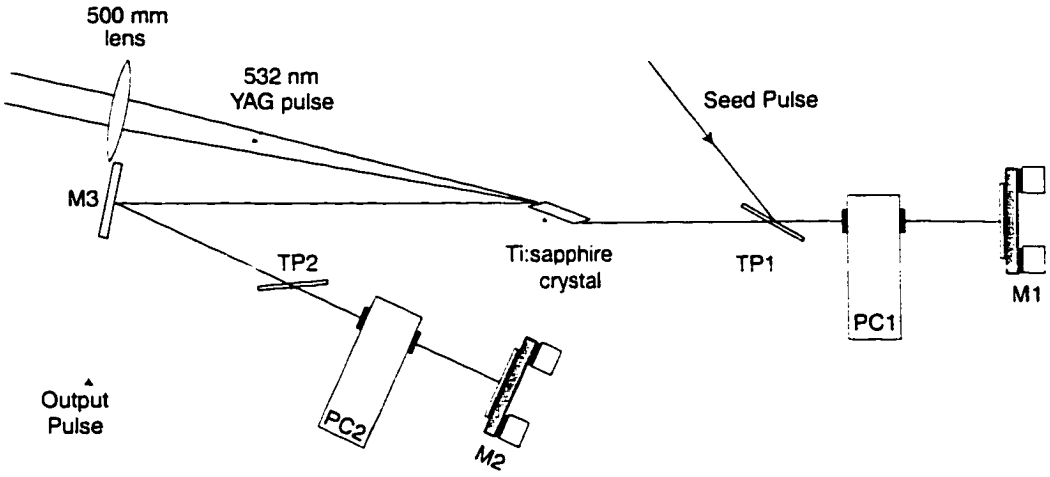

Figure 2.5: Schematic of the regenerative amplifier laser cavity. Light is directed into the cavity with a thin film polarizer (TP1). The polarization of the beam is rotated with a Pockels cell (PC1). Mirrors M1 and M2 comprise the laser cavity. The pulse sweeps gain out of the Ti:sapphire beam pumped with 532 nm light Nd:YAG light and is ejected from the cavity with a switch in polarization from a second Pockels cell (PC2) by TP2.

photodiode collects a small portion of the amplified pulse that leaks out of the laser cavity through mirror M1. The amplitude of the pulse increases with each pass through the Ti:sapphire crystal until saturation is reached. Upon saturation, the pulse can no longer extract energy, and subsequently, energy is lost from the pulse with each pass through the crystal. The oscilloscope monitors both the mode out of the Ti:sapphire laser and the gain in the Re-gen cavity. The output of the Re-gen is a 786 nm, 5.0 mJ pulse.

Timing of light injection into and ejection out of the Re-gen cavity determines the output pulse characteristics. Triggering of PC1 is controlled by trigger A of the Stanford Research Systems (SRS) timing box. This trigger is synchronized with the Nd:YAG laser to ensure the pulse is injected into the Re-gen immediately after the Nd:YAG pulse has provided gain to the Ti:sapphire crystal. Trigger D of the SRS box

controls when PC2 is triggered. A $\sim$ 180 nsec delay exists between triggers A and D, corresponding to the desired 20 passes of the pulse through the cavity of the Re-gen. The light is switched out of the cavity when the pulse has reached maximum power. Actually, the pulse is much more stable when it is ejected after the power has started to roll past the maximum. The stability occurs when the gain is less sensitive to fluctuations in the seed light. The arrival of the short laser pulse dictates the timing of experiments in the lab, and this is determined by the ejection time of the pulse from the Re-gen cavity. Therefore, to attain proper pulse amplification, alignment of the cavity is most important. Any adjustments to the timing of the cavity must be noted by anyone using the short laser pulse.

Proper alignment of the regenerative amplifier is crucial for pulse amplification. The cavity is aligned in the following manner. First, the seed light is blocked from entering the laser cavity. Then, the D-trigger timing, which determines when the laser pulse is switched out of the cavity, is increased by 3 μsec. The power of the Nd:YAG light is set to 0.2 W and is sent through the Ti:sapphire crystal. Fluorescence of the crystal should promote lasing action in the Re-gen cavity. When this occurs, a bright dot should appear on M3, as viewed with the video output of an open-aperture camera. The absence of a bright dot requires the slow adjustment of the polarizer transmitting the Nd:YAG beam, which increases the beam's power until a spot appears on the mirror. Once the spot is present, carefully adjust the alignment of M1 to maximize its brightness, reducing the power of the Nd:YAG light as alignment improves. After the laser cavity is optimized, reduce the power of the Nd:YAG light via the polarizer until the spot is barely visible. This is the threshold point for lasing in the Re-gen and is usually between 0.18 and 0.2 W. Significant deviation from these values indicates a problem either with the Re-gen or with the Nd:YAG laser that

needs to be addressed. The input and output surfaces of the Ti:sapphire crystal must be inspected while low intensity light is passing through. Scattered green light from either surface indicates the presence of dust particles that can absorb large amounts of energy and damage the surface of the crystal. Usually, the dust particles are easily removed by gently blowing on the crystal surface with compressed air.

The D-trigger time *must* be returned to its initial value before further operation of the Re-gen. This prevents damage to the Ti:sapphire crystal. Spontaneous lasing in the cavity due to fluoresence of the pumped Ti:sapphire crystal can build up to destructive levels unless the light is switched out of the cavity at the proper time. The aperture of the video camera should be reduced to limit saturation of the CCD pixels. The power of the Nd:YAG light should be increased to about 0.58 W by rotating the polarizer from $\sim 18^o$ to $\sim 30^o$. A large deviation from these angles may indicate the flash lamps in the Nd:YAG are aging and need to be replaced. After the timing has been returned to a 180 nsec relative delay between the A and D channels, the Nd:YAG light is allowed to pass through the Ti:sapphire crystal. A prominent spot should be visible on M2. Allow the seed light to enter the Re-gen. The spot on M2 should be very bright. The photodiode should indicate the amplification of the pulse through several passes through the cavity. The amplification will reach a maximum and start to turn over for the final peak before the pulse is ejected from the cavity. Adjusting the power of the Nd:YAG beam is the most effective way to fine-tune the power of the pulse when it is ejected after the cavity alignment has been optimized. The amplified pulse leaving the Re-gen follows a path nearly opposite to the seed pulse and a Pockels cell is placed in the beam path to prevent the ejected pulse from entering the mode-locked laser and destroying the laser's mode-locking capabilities. We check the alignment of seed pulse beam into the Re-gen by making

sure the output pulse returns along (nearly) the same path.

Multi-pass Amplifier

To attain peak power on the order of TWatts, energy in the laser pulse is further increased with the multi- pass amplifier. As with the regenerative amplifier, the pulse is amplified by passing it through a Ti:sapphire crystal in which gain is introduced with a portion of the 532 nm Nd:YAG light. The 200 psec chirped pulse passes through the crystal three times and its energy is increased by a factor of $\sim$10, typically bringing the total time-averaged power of the beam up to about 450 mW. The energy per pulse increases from 1 nJ to about 30 mJ in the total amplification process, but the pulse still requires compression in time. The amplification due to the three passes through the Ti:sapphire crystal correlates with the energy content of the Nd:YAG pump beam. However, to maintain laboratory consistency, the beam is amplified to 450 mW, and the half-wave plate transmitting 532 nm Nd:YAG light to the multi-pass amplifier should be rotated to $\sim 70^{o}$. The multi-pass amplifier requires very little day-to-day alignment.

The amplification characteristics of the Ti:sapphire crystal are temperature sensitive. Therefore, water lines, which maintain constant temperature, pass through the metal mounts holding each Ti:sapphire crystal in the Re-gen and the multi-pass amplifier. The water is held a few degrees above room temperature.

The amplified laser pulse is ready to be sent to the compressor. A large amount of energy is present in each pulse, however, and if all of the energy was compressed into a single 120 fsec pulse in a 1 cm diameter beam, the intensity would result in beam degradation due to self-phase modulation and self focussing. To prevent these effects, the beam passes through a 50% beam splitter and each portion of light is sent

to a separate pulse compressor. The output of each compressor is a 15 Hz train of 786 nm pulses that each delivers ~10 mJ in 120 fsec.

2.2.3 Dye Lasers

A common tool used in Rydberg state excitation is the dye-laser. This type of laser provides 5 nsec pulses that are tunable over a specified range ($\lambda_o \pm 15$ nm) and provides a stable, narrow bandwidth (0.1 - 1.0 cm^{-1}) beam. Different dyes enable lasing at UV, visible, or near-IR wavelengths. The general idea behind the operation of a dye-laser is to pump energy into an organic compound (the dye) with a harmonic from the Nd:YAG laser. The dye absorbs and re-emits energy over a broad frequency range. A portion of the frequency spectrum is trapped in a laser cavity, and successive passes of light through the dye promotes amplification at a specific color. A solution of the dye compound dissolved in methanol or ethylene glycol acts as the gain medium of the laser.

Two important characteristics of the dye molecules make dye lasers experimentally advantageous. First, the absorption cross section of each dye molecule is very large, necessitating only a relatively dilute solution of dye molecules for strong lasing action. Second, the radiative lifetime of the dye is short, on the order of a few nanoseconds [5]. The short lifetime ensures the laser pulses from our dye lasers mimic the ~5 nsec duration of the Nd:YAG laser pump pulse. Amplification of a specific frequency in a laser cavity occurs in different ways. Two types of dye-laser configurations, the Hansch style[8] and the Littman style [9], have been used for experiments presented in this thesis.

Hansch dye-lasers generate 5 nsec, ~1 mJ laser pulses that have a bandwidth of ~1 cm^{-1}. The laser cavity consists of a mirror, telescope and diffraction grating.

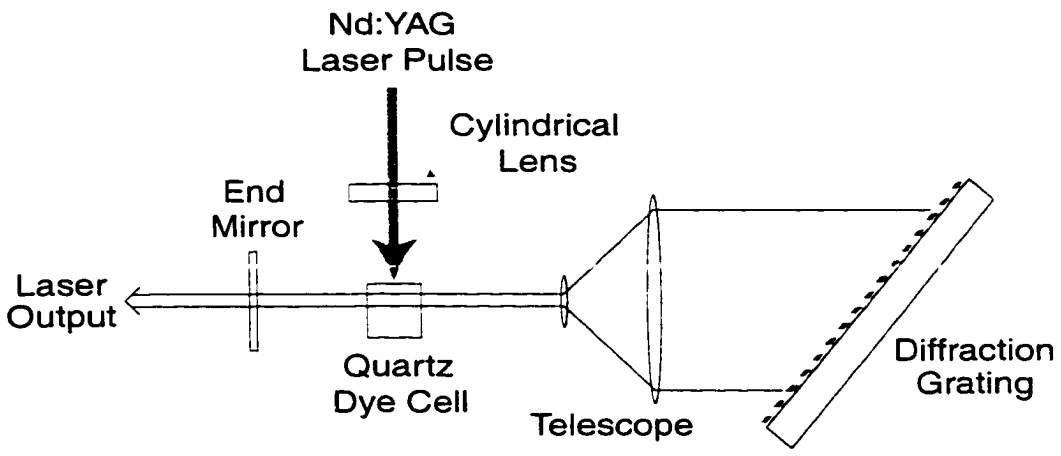

Figure 2.6: Operation schematic for a Hansch style dye-laser. A diffraction grating and mirror comprise the laser cavity.

Laser dye is pumped through plastic tubing from a reservoir to a quartz cuvette that houses the flow of laser dye through the laser cavity. A cylindrical lens focuses the Nd:YAG laser beam to a line in the dye cell. Light is absorbed and re-emitted by the dye, and a small portion of the light oscillates in the laser cavity. Light diffracts from the grating at an angle that depends on the wavelength, and only light within a small range of frequencies diffracts from the grating into the laser cavity. To reduce the bandwidth of the output beam, a telescope is placed in the laser cavity so light covers most of the grating. The line width of the beam varies as the inverse of the number of grating lines that contribute to the diffraction pattern.

A diagram of a Hansch style dye-laser is shown in Figure 2.6. Light returns from the grating and passes through the dye, and a small fraction of the light escapes through the output coupler. A second dye cell may be placed outside the laser cavity for single pass laser amplification. The bandwidth for the output pulse is $\sim$1 cm^{-1}.

To achieve even narrower bandwidth, at the expense of lower power output, a dye laser can be arranged in the Littman configuration. The operation is similar

to the Hansch style laser, except light diffracts from the grating at a much steeper angle. No telescope is present in the cavity and the light emitted by the dye strikes a diffraction grating at grazing incidence. A diagram of a Littman style dye-laser is shown in Figure 2.7. Light diffracts off the grating and scatters towards a tuning mirror mounted on a rotation stage. This mirror and the end mirror form the laser cavity. Different wavelengths scatter at different angles from the grating and only light at a specific frequency returns from the mirror and scatters off the diffraction grating a second time. Each pass off the grating further reduces the bandwidth in the pulse. Because the light approaches the grating at grazing incidence, a majority of the light is lost and the output power of a Littman style laser is small compared to the Hansch style. A single-pass amplification stage is added just beyond the laser cavity to improve the power output. However, the grazing angle ensures the bandwidth of light remaining in the laser cavity is very small, typically $\ll 1\ cm^{-1}$.

To operate dye-lasers, specific protocols must be followed. Most importantly, proper handling of the laser dye is required. The organic compounds used for the laser dye can be carcinogenic or mutagenic to humans. Therefore, latex gloves should be worn when handling the dye, and all dye mixing should be done in the fume hood. For laser operation, the dye should flow upwards through the quartz cell, minimizing the entrapment of air bubbles in the active lasing area. The dye needs to be replaced periodically. One sign of the laser dye degradation is a rapid decrease in Rydberg state signal size over a matter of minutes. Signal can disappear for many reasons, but the most common and easily fixed problem is the failing of a dye laser. Inspection of pump beam penetration into the laser dye is a good way to measure dye viability. If light is penetrating more than half-way across the cell, the dye probably needs to be changed. The laser dye can be very expensive. To extend its lifetime, block the

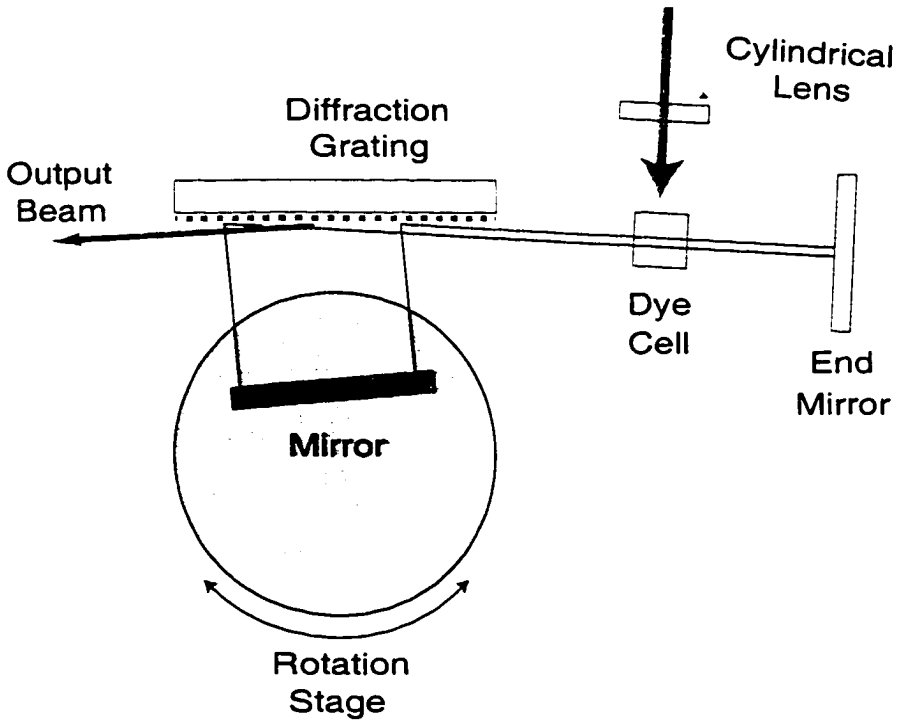

Figure 2.7: Operation schematic for a Littman style dye-laser. Grazing incidence of light off the diffraction grating ensures a small bandwidth.

pump light when the laser beam is not being used.

Proper dye laser function is monitored with an etalon, which acts as a Fabry-Perot interferometer. Due to its small diameter, the laser output is expanded with a diverging lens before being sent through the etalon to be able to resolve fringes. Just past the etalon, a smooth, circular interference pattern is a sign of a properly aligned laser. The bandwidth of the laser can be estimated from the width of the minima and maxima of the fringe pattern. The spacing between maxima is defined by the free spectral range of the etalon and is given by $1/2nd$, where n is the index of refraction and d is the thickness of the etalon. As the laser is tuned, the change in wavelength can be calibrated by monitoring the brightness level of the interference pattern at a fixed position in space with a photodiode.

2.3 Half-Cycle Pulse (HCP) Generation

Ultrashort, optical pulses are excellent for Rydberg wavepacket creation because of their large bandwidth and short interaction time with atoms. Optical pulses are also useful in monitoring wavepacket dynamics, but only when the wavepacket is near the atomic core where the probability for optical photon absorption is high. When a localized Rydberg wavepacket is far from the core, near its outer turning point, it resembles a free electron. An optical pulse will shake a free electron during the interaction, but does not transfer energy or momentum to the electron without a heavy body nearby.

In recent years, a radiation source has been developed that allows us to probe the dynamics of an electronic wavepacket, even (and especially) when the wavepacket is far from the nucleus. A nearly uni-polar, sub-picosecond pulse of radiation is produced by the sudden acceleration of electrons in a biased GaAs semiconducting wafer, which

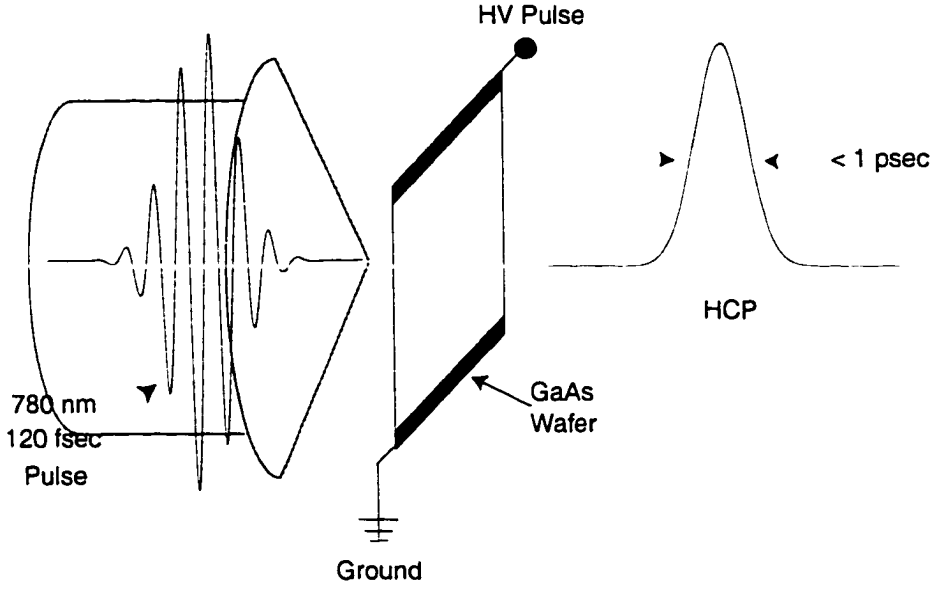

Figure 2.8: Diagram of half-cycle pulse (HCP) generation. A fat, short laser pulse uniformly bathes a biased GaAs wafer, quickly sending the wafer to a conducting state. A rush of electrons through the wafer produces a nearly uni-polar electric < 1 psec field pulse.

is initiated by a 120 fsec, 786 nm optical pulse [10, 11]. A half-cycle pulse (HCP) is useful because, unlike an optical pulse, the time-integrated electric field over the duration of the pulse is non-zero. Energy and momentum can be delivered to a free electron, or to an electronic wavepacket, when it is far from the nucleus. Final state analysis of a wavepacket after its interaction with a HCP provides information about the motion of the wavepacket at the time of the interaction. Therefore, the evolution of an electronic wavepacket can be monitored throughout its entire orbit with the use of HCPs. HCP generation and various experimental considerations are discussed in this section, whereas the interaction between an electron (or wavepacket) and a HCP is presented in later chapters.

HCPs are generated in a gallium-arsenide (GaAs) photo-conductive switch. GaAs is a semiconductor with a band-gap of 1.4 eV, and light having a wavelength $\lambda \leq$

880 nm will promote electrons from the valence band to the conduction band. The maximum radiation is produced with a laser fluence of only 40 νJ/cm^2 [10]. In the valence band, GaAs has a resistance of $\sim 10^9\ \Omega/cm$ [12] and easily holds off high voltage. Upon arrival of a 120 fsec, 786 nm optical pulse, the GaAs wafer is rapidly driven to the conduction band, in which the applied bias creates an 'avalanche' of accelerating electrons in the wafer. The charge accelerates for a short period of time and a short, nearly uni-polar electric field pulse with a width of $\sim$1 psec is produced [10]. Figure 2.8 shows a diagram of HCP production. The radiated HCP field is polarized along the biased field axis of the wafer and has an amplitude which scales proportionally to the applied field.

The HCP propagates away from the wafer, and the electrons (relatively) slowly decelerate as the wafer returns to the insulating state. The deceleration of the electrons also produces radiation, but it comes in the form of a long, negative tail trailing the initial HCP. The main HCP has a field amplitude at least 5$\times$ the amplitude of the negative tail [10]. A second artifact of HCP creation is the presence of an oppositely polarized HCP trailing the initial HCP by about 11 psec. This pulse is the reflection of HCP radiation from the back side of the GaAs wafer and has a much smaller amplitude than the main HCP. We have developed a way to attenuate the negative tail, as well as the reflected pulse, by 'cleaning' the HCP, a technique discussed in detail in Chapter 4.

The GaAs wafers are purchased from American Xtal Technology Corporation and come in 2 inch diameter circles that have a thickness of $\sim$ 0.5 mm. The GaAs wafer is undoped and polished on one side. The HCP field strength scales with the area of the wafer, but reaches a maximum when the wafer is about 10 cm^2. Saturation seems to occur because of a non-uniform acceleration of electrons across the wafer when there

is a large separation between the biased side of the wafer and the grounded side. To avoid saturation in the large wafer, each wafer is cut into four pieces. Each piece is large enough to produce large amplitude HCPs, and this practice promotes a more efficient use of costly GaAs wafers.

To cut the GaAs wafer, three clean glass slides, a soft cloth, and a diamond scribe are needed. One side of the wafer has a flat edge, defining a fault axis in the crystal. Wearing talc-free gloves to prevent contamination, rest the GaAs wafer on the cloth with the polished side face up. Place the edge of a glass slide either parallel or perpendicular to the flat edge of the wafer down the middle of the wafer. With one hand, hold the glass slide gently, but firmly, against the wafer to prevent it from sliding. With the other hand, firmly drag the tip of the scribe across the surface of the wafer a single time along the edge of the glass slide. Next, place one of the other two glass slides on the cloth and sandwich the wafer between it and the third glass slide. Position the wafer so the scratch lies just beyond, and parallel to, the edge of the two glass slides, while holding the slides firmly. Place the third glass slide over the portion of the GaAs wafer that is sticking out from between the two slides. Simply tap the glass slide. The wafer should sever smoothly along the scratch. The process is repeated until a wafer of desired size is produced. Clean the glass slides between cuts because fragments of the GaAs wafer produced in the previous cut may remain on the surface of the glass slide and damage the wafer on subsequent cuts.

Each $\sim 2 \times 2$ cm wafer needs to be mounted for HCP production. The bottom edge of the unpolished side of the GaAs wafer is adhered to an aluminum slab with conductive silver paint. A large, rectangular portion of the wafer must remain above the mount and free from silver paint. The aluminum slab is fastened to a rotation stage and is grounded with a connecting wire. A thin, uniform stripe of silver paint is

applied to the top of the wafer on the highly reflective side. It is important not to let any silver paint get on the back of the wafer, which would increase the likelihood of arcing across the semiconductor surface. The end of a well insulated wire is attached to the top conducting strip with a drop of silver paint. This wire is connected to the high-voltage source that provides the bias across the wafer. The conductive strip must be uniform. Any sharp features in the strip will have large field gradients, thus increasing the chance of the GaAs wafer breakdown and loss of its insulating capability.

The HCP is created when the GaAs wafer is sent from the valence band to the conducting band with a short pulse of 786 nm light. For proper HCP creation, the illuminating laser beam must be relatively uniform in brightness over the surface of the wafer. The short pulse is "telescoped up" to a wide, 3 cm diameter beam from the original 1 cm beam diameter. This is achieved using a diverging and converging lens pair separated by the focal length difference between the converging and diverging lenses. The ratio of focal lengths gives the relative size of the input to output beams of the telescope. The HCP propagates in the same direction as the incident light beam. Before the wafer is in place, the beam is aligned to ensure it passes through the laser/atom interaction region. Positioning and alignment of the GaAs wafer is also important. With the telescope in place, use an IR card to look at the shadow of the wafer. The shadow should be in the center of the beam and the top corners of the shadow should be near, but not touching, the edge of the beam. This check ensures the wafer is completely and uniformly illuminated by the short laser pulse. Also, the wafer must lie in the plane perpendicular to the laser beam propagation direction to ensure simultaneous promotion of the GaAs wafer to the conduction band. Misalignment of the wafer may cause the resultant HCP to be distorted in

time.

Wafer alignment is tested as follows. Remove the telescope from the beam path (remember to remove the converging lens to prevent damage to optical components through unwanted focusing) to increase the brightness of the beam. Aperture down the beam until it has about a 2 mm diameter. Look for the reflected beam from the GaAs wafer surface with the IR card and adjust the wafer position until the reflected beam sits on top of the incident beam.

Another technique is essential for good quality HCP production. Small, but not negligible, components of the short laser pulse in the form of pedestals on the leading and trailing edges of the pulse decrease HCP quality. The leading edge arrives at the HCP first and may promote a portion of the wafer to the conducting band, resulting in a poorly characterized HCP. A neutral density filter ($T \approx 0.4$) acts as a saturable absorber and attenuates the leading edge of the short laser pulse. The remainder of the pulse passes through the filter to the wafer, creating a high quality HCP of THz radiation.

2.4 Vacuum System

The experiments presented in this thesis have been performed in a cylindrical, aluminum vacuum chamber that maintains a pressure of $\sim 10^{-6}$ torr. The vacuum chamber is roughly 2 feet in diameter and 1 foot deep. A diagram of the vacuum chamber is shown in Figure 2.9. Eight flanges around the side of the chamber and five on the lid hold various devices, such as electrical feed-throughs, windows, cooling water feedthroughs and pressure guages, and are arranged according to the experiment. All seals between flanges and the vacuum chamber are made with Buna-type O-rings. Directly beneath the chamber is a gate valve, which makes it possible to

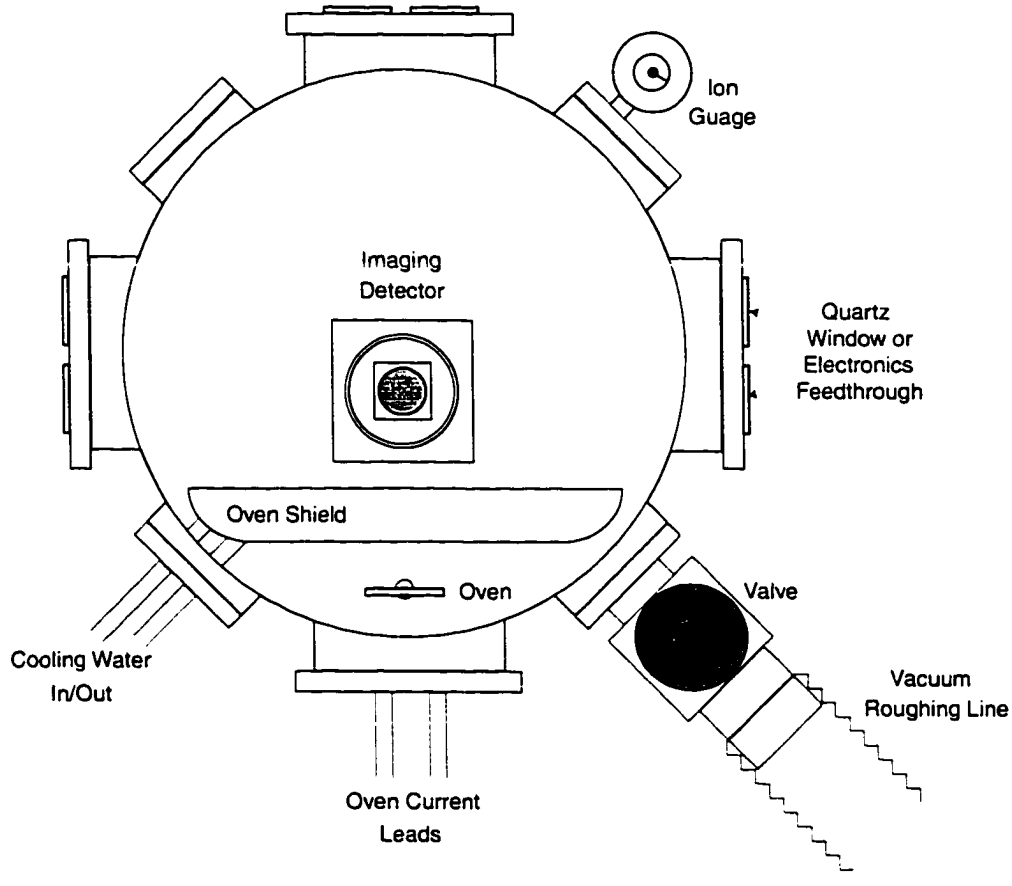

Figure 2.9: Overhead view of the vacuum chamber. Elements consistent for all experiments are shown. Different optic elements and other devices can be placed in the large open area around the detector.

isolate the vacuum chamber from the pumps below when closed.

A Varian VHS-6 model diffusion pump is currently used to reach low pressure in the chamber, replacing a smaller, less powerful pump. This pump takes 500 cm^3 of vacuum pump oil, which can be purchased from Duniway Stockroom, part number DS-7040. In the diffusion pump a reservoir of oil is heated near the bottom of the pump and cooled near the top of the pump. The downward stream of oil vapor creates a flow of air molecules from the top of the chamber to the bottom. These particles are exhausted from the vacuum system with a mechanical roughing pump. The chamber

reaches pressures as low as the mid-10^{-7} Torr range with this large volume diffusion pump.

Directly above the diffusion pump is a Varian model 336 water- baffle. This baffle acts as a cold trap and prevents large amounts of diffusion pump oil vapor from drifting into the vacuum chamber. Cooling water flows through the baffle, which contains a series of interwoven metallic fins.

The vacuum pressure is monitored with an ion gauge that is contained in a glass bulb mounted on the side of the vacuum chamber. Electrons are emitted by a hot filament in the bulb and are accelerated to a positively biased metal grid. Electrons collide with particles and create ions that are detected by a collecting element. The ion current is correlated to the vacuum pressure, which is shown on a digital LED display.

The diffusion pump is powered by the 208 VAC originating from the bus lines running along the ceiling of the lab. The power line is directed through an interlock switch for safety purposes because a continuously running 2200 Watt device can pose a hazard if left unregulated. We want to prevent the diffusion pump from causing damage to the lab as well as damage to the pump itself. The Varian VHS-6 diffusion pump has an internal temperature gauge that turns off the power to the heating element of the pump if it gets too hot. This may occur if the cooling water lines do not supply enough water. The diffusion pump remains turned off if the power in the lab switches off for any reason. Sometimes the roughing pumps do not start up immediately, or some other problem might arise in the lab, and its best for the diffusion pump to be turned back on manually. Also, the pump shuts itself off if the pressure gets too high. A leak somewhere in the vacuum chamber or roughing line may allow for a pressure greater than the diffusion pump's capacity. Over pressure in

the diffusion pump may result in oxidation, or 'cracking,' of the pump oil, which can only be remedied by dropping the pump and scrubbing it clean. The diffusion pump turns off if the pressure in the pump's roughing line exceeds 150 mTorr. When the diffusion pump switches off, it must be turned back on manually. The current relays for the interlock switch are powered by a typical 110 VAC (wall) source.

2.5 Atom Source

Neutral atoms are supplied for each experiment in an effusive beam emitted by a resistively heated oven. The oven is made with a 6 inch stainless steel tube typically 3/8 inch in diameter and $\sim$ 0.006 inch in thickness. A 0.5 mm hole is drilled half-way up the tube. A one inch segment of the tube is clamped in a vice and the tube is filled with calcium shot to a level just below the hole. The tube can be filled with any alkali atom or alkali earth atom. Some volatile materials, like sodium, must be handled with great care. All experiments presented here, however, have been performed with calcium. As the tube is filled, it is gently shaken to settle the calcium shot. Once filled, the other end of the tube is clamped and the tube is attached to the oven mount. The tube completes a loop of a high-current circuit. The current is supplied by a series of transformers and is regulated by a Variac AC voltage regulator. A diagram of the circuit is shown in Figure 2.10.

As current passes through the oven, the stainless steel heats to a temperature where calcium atoms melt and vaporize. The atom- gas pressure increases in the tube and atoms spray out the 0.5 mm hole in an effusive beam. Typically, to provide an atom density of $\sim 10^9$ atoms/cm^3 in a region 10 cm from the oven, new calcium ovens require a current of about 70 A. Ovens that have been used extensively require nearly 100 A. It is unlikely that you will be working with an oven at currents over 100

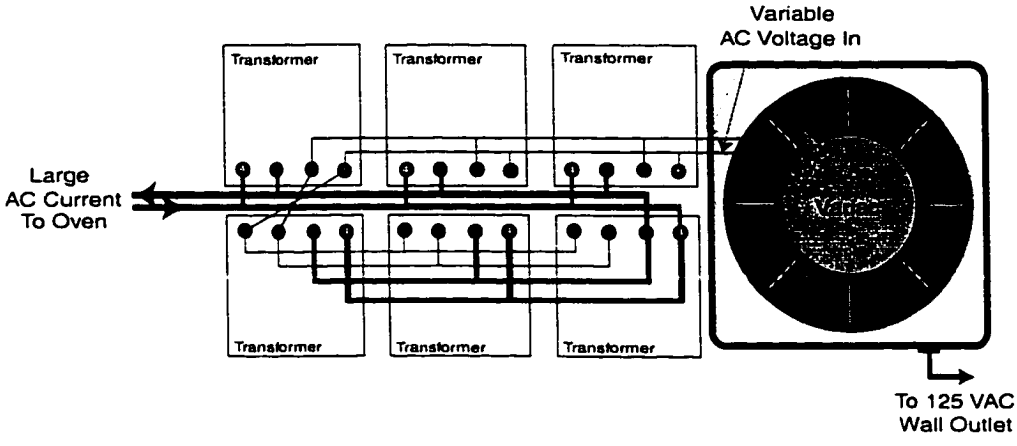

Figure 2.10: Circuit diagram for the large current supply for the atom source oven. A small fan blows air over this circuit to prevent overheating.

A for a long time, because either the atom supply drains or the oven tube splits in half because of high temperatures. The atom beam is roughly collimated with a sequence of apertures and is directed to a region where the electric field can be controlled and electromagnetic radiation interacts with the atoms.

The atom source gets very hot during operation, especially when using an atom with a high melting point, like calcium. Therefore, a heat shield is installed in the vacuum chamber to prevent global heating of the vacuum chamber and heat damage to any optics and detection devices. The shield consists of two 1/8 inch thick copper sheets sandwiching a quarter inch copper tube that carries cooling water. The water line is a continuous loop that enters and leaves the vacuum chamber through 1/4 inch feed-throughs built by Kurt J. Lesker Co. The water supply to the oven shield should be turned off approximately 30 minutes before the vacuum chamber is opened to air. This allows the cooling lines to reach room temperature and prevents water condensation from accumulating on the line and discouraging low vacuum pressure. The current feed-throughs similarly get hot when large currents are flowing, therefore

copper heat sinks are attached and cooled with a small fan. A fan also cools the series of transformers supplying the current. Excessive heat build-up might cause solders in the circuit to melt and destroy the current supply.

2.6 Experimental Tools

Many tools are used for data acquisition in the lab. Several of the most useful ones are described below.

2.6.1 Voltage Pulse Box

Ion creation and detection is an efficient technique for final state measurements of atomic systems. Rydberg atoms are readily ionized with moderately high electric fields that can be produced with a voltage pulse box. These transformer boxes require relatively low DC voltages and deliver a highly ($\sim 50\times$) amplified pulse that reaches maximum value in a few microseconds. The circuit diagram for a voltage pulse box is shown in Figure 2.11. A 5 V trigger pulse determines when the HV pulse is delivered. The polarity of the pulse is controlled with a switch and a static field can be applied so the pulse sits on top of some non-zero value.

2.6.2 Slow HV Pulse Box

Slow HV pulse boxes provide the bias to the GaAs wafers used in HCP generation. This type of voltage pulse supply is similar to the voltage pulse box described above, but it uses a relatively inexpensive car-transformer for voltage amplification. The rise time of the pulse is about 50 μsec, and the voltage is roughly $50\times$ the input voltage. The trigger is supplied by a source other than the SRS box because the trigger must arrive well before the laser system trigger to synchronize the slow rising pulse with

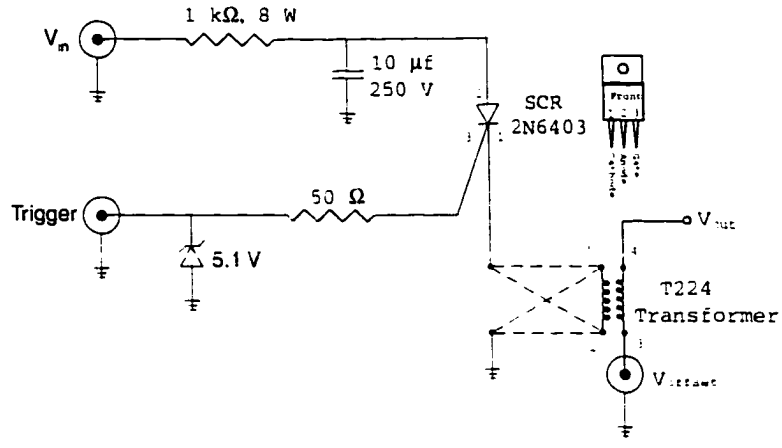

Figure 2.11: Circuit diagram for the HV pulse generators.

the laser light. Positive DC voltage provides the power, and the polarity of the output pulse is determined by an added switch.

2.6.3 Behlke Fast HV Pulse Box

Some experiments require a very rapid applied electric field. The Behlke fast switch takes a HV DC input and delivers an output pulse (that matches the input voltage) with a $\sim$ 10 nsec rise time. The output pulse has a peak voltage amplitude that matches the input voltage. The pulse remains at peak voltage for the duration of the trigger pulse and drops to zero in a time determined by the RC time constant of the circuit. This type of pulse is useful to clear ions out of the atom/laser interaction region quickly, before some final state in the remaining neutral atoms is monitored.

2.6.4 Computer/Oscilloscope Interface

Data collection requires the transfer of information from various instruments to a computer. To collect and store quantitative data, a personal computer (PC) has been supplied with a General Purpose Interface Board (GPIB) device with which

information is transferred from an oscilloscope to the PC. A series of software programs has been written by Tom Bensky, a former graduate student in the lab, that uses the GPIB interface to control the flow of data from a range of oscilloscopes. The software allows the user to average a desired number of oscilloscope traces and write the averaged trace to a file. A portion of the oscilloscope trace can be gated and integrated, enabling the user to monitor variations in voltage for a region of the oscilloscope trace. The software also provides the option to control different types of stepper motors with electric pulses sent from the parallel port of the PC. The oscilloscope is usually triggered by a photodiode, therefore the stepper motors become synched to the laser system in the lab. These programs have a root name DC (for Data Collection) and are called DCL, for data collection through the LeCroy oscilloscope, and DC410, for data collection with the video-triggered Tektronix 410A digital oscilloscope.

A variety of motors are used in the lab to automate the data acquisition process. The first type of motor is a simple, continuously running motor that has an adjustable rotation speed for the external driver. Usually, this motor is used to slowly rotate the diffraction grating of a dye-laser, so the frequency of the laser continuously changes in time. No interaction between this type of motor and a data-acquisition computer exists, therefore calibrating the number of rotations made by the drive shaft during a measurement must be performed by some other means.

Two other types of motors are used in automated measurements. The first is simply a magnetic stepper motor that contains a drive shaft that rotates a fixed amount for every trigger pulse sent to it. The trigger pulse is supplied by the parallel port of the PC, and an external DC power supply of 5 V is required. This motor has a fairly course control, therefore it is typically used to turn voltage knobs of DC power

supplies. Another type of motor used in the lab is a high- precision Burleigh motor. The Burleigh motor adjusts a translation stage in steps as small as 4 nm. and is useful for high-precision delay control of a leg of a Michelson interferometer. The motor has its own control CPU and can translate the delay stage a specified distance every N^{th} trigger pulse. The Burleigh motor and the oscilloscope are both synchronized to the laser system. to ensure a perfect correspondence between the motor operation and data acquisition.

Bibliography

[1] Spectra-Physics *Pulsed Nd:YAG Lasers User's Manual*. Spectra-Physics, Mountain View, CA (1994).

[2] Anthony E. Siegman, *Lasers*, University Science Books, Mill Valley, CA (1986).

[3] Jean-Claude Diels and Wolfgang Rudolph, *Ultrashort Laser Pulse Phenomena*, Acedemic Press (1996).

[4] Coherent, *Ion Laser Operator's Manual*. Coherent Laser Group, Santa Clara, CA.

[5] Orazio Svelto, *Principles of Lasers*, Plenum Press, New York, NY (1976).

[6] D.E. Spence, P.N. Dean and W. Sibbett, *Opt. Lett.* **16**, 42 (1991).

[7] Spectra-Physics, *Model 3900S CW Ti:Sapphire Laser Instruction Manual*, Spectra-Physics, Mountain View, CA (1990).

[8] T.W. Hansch, *Appl. Opt.* **161**, 895 (1972).

[9] M.G. Littman and H.J. Metcalf, *Appl. Opt.* **170**, 2224 (1978).

[10] D. You *et. al.*, *Opt. Lett.* **18**, 290 (1993). R.R. Jones, D. You and P.H. Bucksbaum, *Phys. Rev. Lett.* **70**, 1236 (1993).

[11] R.R. Jones and P.H. Bucksbaum. *Comments on Atomic and Molecular Physics* **28**, L457 (1995).

[12] Americal Xtals, Inc., GaAs Data Sheet.

Chapter 3

Single-Shot Delay-Range Imaging Detector

3.1 Introduction

The effort expended to create electronic Rydberg wavepackets in atoms is exceeded in the lab by the struggle to monitor the dynamics of these evolving systems [1, 2]. The experiments described in this dissertation involve time-domain measurements in which a wavepacket is created with a short pulse of electromagnetic radiation and probed with a second short pulse a finite time later. The probe sends the wavepacket into some final state. Depending on the specifics of the experiment, information about the initial wavepacket can be retrieved by observing the final state population's response to varying the relative time delay between the pump and probe pulses. Pump-probe measurements have been utilized extensively in recent years, including techniques such as photoionization [1], fluorescence [1], the optical Ramsey method [3], the impulsive momentum retrieval method [4], pulsed field ionization [5, 6], and the atomic Streak camera [7].

Each of these methods is annihilative, and the non-stationary electronic state created by the pump pulse is destroyed by the probe pulse. As a result, a wavepacket

can only be 'observed' once in its lifetime. Multiple measurements, or pump-probe pairs, are necessary to extract the evolution of a wavepacket.

The precision and accuracy of any measurement relies on experimental stability. Slight shot-to-shot fluctuations occur in both the pump and probe pulses, but signal noise can be reduced by averaging several consecutive measurements at a fixed relative delay between pulses. Traditionally, time-domain measurements are made over a range of fixed delay positions at which signal is averaged for a set number of pump-probe pairs. When using a low repetition rate laser system, a full delay scan can take several minutes. Coupling this with the (usual) need to vary some other experimental parameter necessary for extracting detailed information of wavepacket evolution makes time domain measurements lengthy endeavors. A single measurement consisting of 15 delay scans can take over an hour. Experimental drifts during that time make multi-parameter space measurements prohibitively difficult. Instabilitiess that occur on an hour time scale include the Ti-sapphire laser falling out of mode-lock, laser beam alignment and power output, and atom source fluctuations.

To drastically reduce the time needed to make time-domain measurements and avoid the effects of long-term experimental drifts, we have built a detector that records a delay scan with a single pump-probe pair. The single-shot detector works in analog with a single-shot autocorrelator [8, 9] that extracts temporal characteristics of an optical pulse. In an autocorrelator, a single optical pulse (for example) is divided and sent at a non-zero relative angle through a crystal. The crystal facilitates generation of light at twice the frequency of the incident light over the region where the two optical beams overlap spatially and temporally. The region where the crystal emits the doubled light represents the temporal convolution of the optical pulses as they pass through each other in the crystal. In the single-shot detector, ions are detected

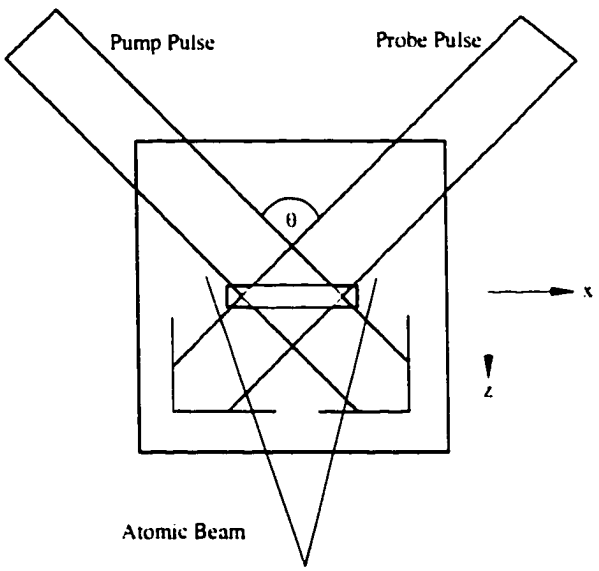

Figure 3.1: Operational schematic diagram of the single-shot detector

instead of doubled frequency light. A schematic of the operation of the single-shot detector is shown in Figure 3.1 [10]. Atoms extended over a volume are excited to some non- stationary state with a short pulse of light. A probe pulse passes through the sample of atoms at a non-zero angle, θ, with respect to the excitation pulse. The average propagation direction of the two pulses is along the $\hat{z}$ axis. Because the pump and probe pulse do not co-propagate, there is a finite relative time difference between the pump and probe pulse for spatially separated atoms. Two atoms separated by a distance d along the $\hat{x}$ axis experience a difference in delay between pump and probe pulses given by

$$\Delta\tau = \frac{2d}{c}\sin\left(\frac{\theta}{2}\right).$$

where c is the speed of light. Ion creation in the sample of atoms varies as a function of delay between pump and probe pulses. The relative delay for each atom scales with its position, therefore, a delay scan is generated with a single pump-probe pair via spatial imaging of ion formation.

3.2 Detector Construction

The single-shot delay-range imaging detector is capable of spatially imaging ion creation in a sample of atoms. As mentioned above, the relative position along the $\hat{x}$ axis of ion formation corresponds to a fixed delay between two radiation pulses passing through the sample at the speed of light. The final state of the atom, determined by the probe pulse and its delay relative to the pump pulse, may be ionized through pulsed field ionization, autoionization, or photoionization.

The layout of the detector is shown in Figure 3.2. The detector images the relative position of ion creation, and a time axis is mapped onto the spatial dimension. A sample of atoms interacts with the pump and probe beams between two 7.5 × 7.5

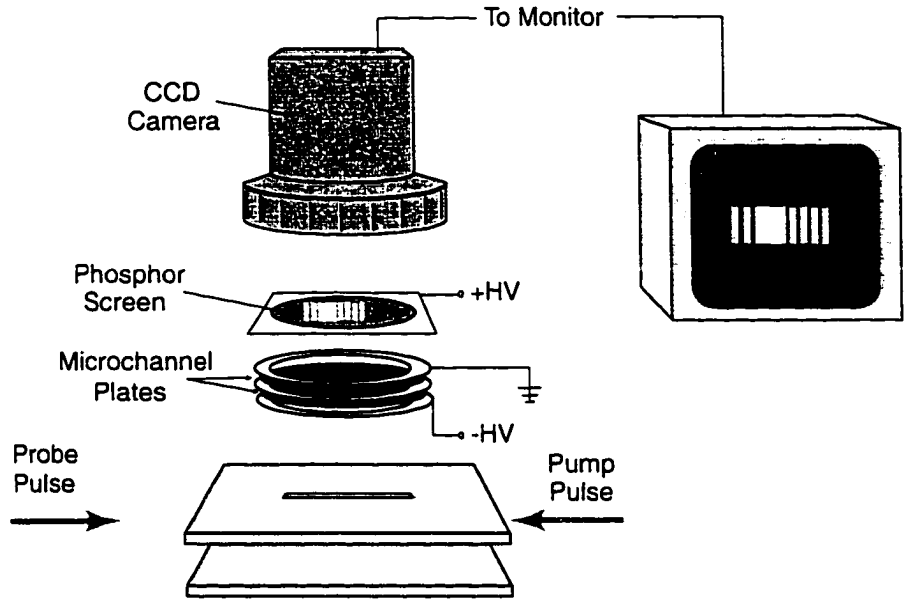

Figure 3.2: General layout of the components in the detector. The relative spacing is not to scale

cm^2 electric field plates. A 3 mm × 25 mm slit is positioned along the $\hat{x}$ axis in the top field plate through which ions are pushed by a positive field pulse applied to the bottom field plate. Once outside the laser-atom interaction region, the ions strike a microchannel plate (MCP) pair positioned roughly 2 cm from the top field plate. The two MCPs are sandwiched between three stainless steel disks. The bottom disk is held at -1400 V. Ions fall towards this potential and the amplified electron discharge from the first and second MCP is accelerated away. The middle steel disk is electrically floating and the top disk is grounded to keep a uniform potential gradient across the MCPs. Electrons from the MCP pair fall towards a phosphor screen biased at +4000 V DC. The signal gain for a MCP is 270× at a bias of 700 V and 6000× at 1000 V. Although signal amplification is enhanced with a 1 kV bias, we limit the bias across each MCP to 700 V to preserve the linear response to the phosphor's brightness to the incident ion signal. In addition, the detector can be configured to detect electrons

ejected from the atom-laser interaction region. In this case, the bottom disk of the MCP mount is grounded and the top disk is biased at +1400 V DC. The phosphor screen needs to be held at a higher potential to maintain the $\sim$ 4000 V 'drop.'

The phosphor screen, produced by the Kimball Physics Company, has a $\sim$ 2 cm diameter active area. The phosphor is mounted on glass that is braced between two 2.5 cm $\times$ 2.5 cm, 0.4 mm thick stainless steel sheets that each have a 2 cm diameter hole in the center. We detect fluorescence of the phosphor screen with a line-synched CCD camera positioned outside the vacuum chamber. The phosphor begins to fluoresce with an incident electron flux energy of 5×10^{-5} W/cm^2 with a damage threshold of 25 W/cm^2, and saturates at a current of 0.03 Amp/cm^2. The peak wavelength of light emitted by the phosphor is 450 nm, which is not optimal because the CCD camera is most sensitive to red ($\sim$ 780 nm) wavelengths. The camera is lensed such that the phosphor screen fills the active video region. The video output is sent to a television monitor, VCR, and a video-triggered Tektronix 410A oscilloscope.

The CCD camera is line triggered at 60 Hz. Therefore, because the laser system runs at 15 Hz, signal appears in every fourth video screen. The video output is characterized by a stream of changing voltages with distinct voltage dips that correspond to either a new video screen (-200 mV, 0.2 msec) or individual line (-200 mV, 0.5 μsec). The CCD camera is monochromatic, so the voltage level between dips corresponds to the brightness level. Each video screen is comprised of 220 lines, yet for the experiments presented in this thesis real-time measurements were restricted to recording a single line of the screen observed with the oscilloscope. The oscilloscope trace is averaged and recorded on a PC through a GPIB connection. Recently, data acquisition hardware and software have been added which allow for many lines to be recorded simultaneously.

The dimensions of the phosphor screen limit the delay range available for each pump-probe pair. A maximum delay range occurs for counter propagating pulses and the active area of the phosphor is about 1.5 cm across which corresponds to a maximum delay range of 100 psec. The spatial resolution of the detector is approximately 300 μm. The resolution is limited by a slight "graininess" of the phosphor and spreading of electrons between the microchannel plates and phosphor screen. Therefore, the temporal resolution is dictated by the relative angle of the pump and probe beams. Picosecond resolution for counter propagating beams and sub-femtosecond resolution for nearly co- linear beams have been observed with this detector.

3.3 Experimental Capabilities

The single-shot delay-range imaging detector is a valuable tool used for several quantitative measurements involving wavepacket evolution. Two experiments are briefly described here, whereas other experiments are mentioned here and discussed in greater detail in later chapters.

In one experiment, we resolve the phase evolution for a Rydberg wavepacket using bound-state interferometry. Following the optical Ramsey method [3, 11], we excite a wavepacket in calcium with a short laser (pump) pulse. After some delay, a second, identical laser (probe) pulse, propagating at a very slight angle with respect to the pump pulse, excites a second wavepacket in the atom. The second wavepacket interferes with the first and the 'strength' of the interference corresponds to the position of the original wavepacket in its orbit when the second pulse reaches the atom, which relates to the initial state character of the wavepacket. Strong interference indicates the wavepacket is localized near the atomic core, just as it was when it was created. Two wavepackets in phase result in a large Rydberg wavepacket population

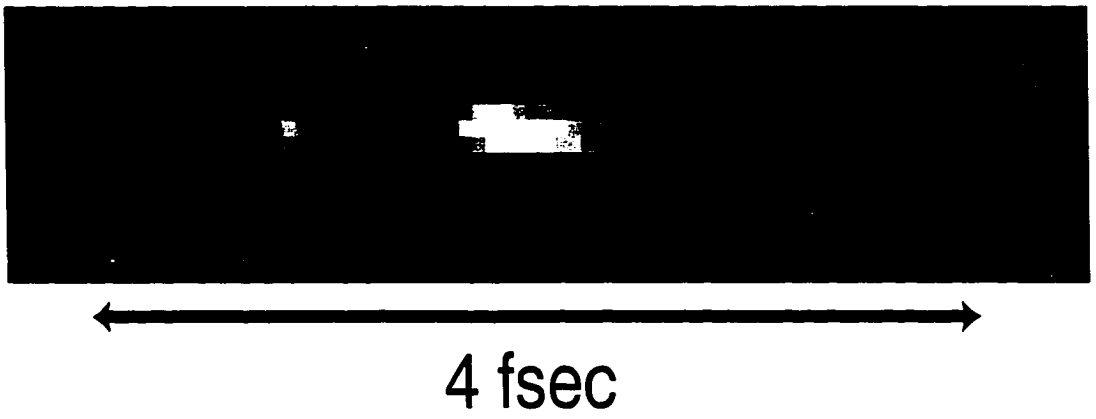

Figure 3.3: Interference pattern in the excitation probability of an electronic wavepacket. Brighter means greater probability. The image is the average of four video frames. Using nearly co-propagating pump and probe beams, sub-femtosecond resolution is achieved.

after the two pulses, whereas two wavepackets perfectly out of phase result in no Rydberg wavepacket population. The pump and probe beams are nearly co-linear and propagate along the $\hat{z}$ axis, perpendicular to the ion extraction slit. The beams are generated from a single source that is sent into a Michelson interferometer. One leg of the interferometer is on a delay stage controlled by a Burleigh stepper motor with 0.5μm precision. The beams are sent through a cylindrical lens telescope so the entire sample of atoms beneath the slit is (nearly) uniformly illuminated. Approximately 1 μsec after the probe beam passes through the interaction region an electric field pulse is applied to the bottom field plate, ionizing any Rydberg wavepacket population. The spatial distribution of ion formation is recorded with the single-shot detector.

Figure 3.3 shows the spatial distribution of ion formation due to an electric field pulse applied to the bottom field plate. Brighter shading indicates higher probability of Rydberg wavepacket population. The wavepackets interfere at the excitation frequency, hence the peaks in Figure 3.3 are separated by 1.3 fsec. The pump and

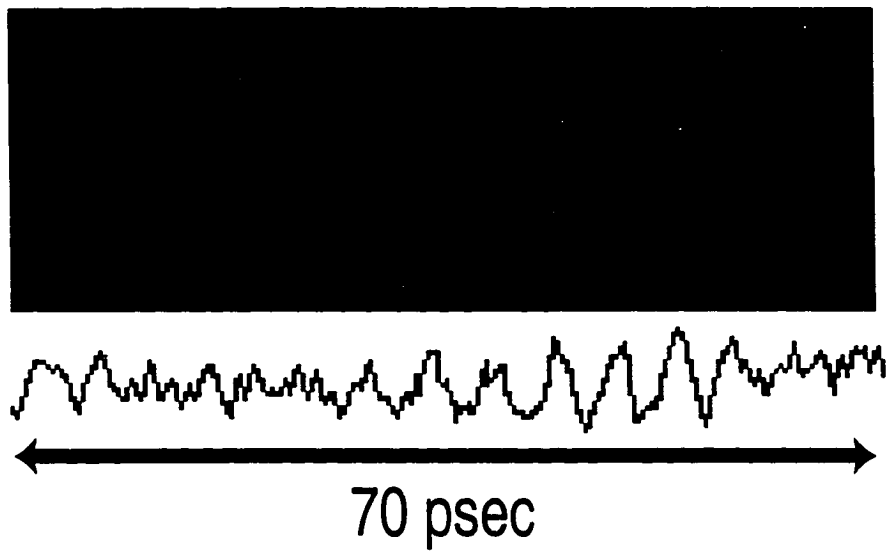

Figure 3.4: Ionization probability of a radial wavepacket due to a HCP. Counter propagating pump and probe beams generate a large ($\sim$ 100 psec) delay range with psec resolution. This image has been taken with a single pump-probe pair, and the two pulses overlap in space and time ($t = 0$) on the far left of the figure. The curve below the image represents the integrated brightness level at each time.

probe beams are separated in time by a duration much greater than their pulse length, therefore the fringe pattern is strictly the atomic response to two delayed pulses. A series of interference patterns taken over a range of large 'macro' delay steps make it possible to observe temporal dynamics of the wavepacket. This method will be discussed in greater detail in Chapter 7.

Also, we have used the single shot detector to monitor the evolution of electronic wavepackets in momentum space using impulsive momentum retrieval [4, 5]. Picosecond resolution is desired for these measurements. The pump and probe beams counter propagate through the interaction region and give the maximum total delay range with each pump-probe pair. Figure 3.4 shows ionization probability of a radial wavepacket in calcium in response to a nearly uni-polar pulse of THz radiation. Ionization due to these pulses varies as a function of the momentum of the wavepacket

along the polarization axis of the pulse, which changes in time. This image was created by a single pump- probe pair and was measured in $1/15^{th}$ of a second. The curve beneath the image represents the integrated brightness level as a function of time. A highly averaged measurement, which has a much stronger signal to noise ratio, takes about 10 seconds with this detector, compared to the $\sim$ 5 minutes needed to make the same measurements using traditional methods.

The following experiments have been performed using the single-shot detector:

1. Measuring the momentum distribution evolution of a radial wavepacket (Chapter 4),

2. Measuring the momentum distribution evolution of a Stark wavepacket (Chapter 5),

3. Measuring time-dependence of electron-ion recombination of photo-ionized electronic wavepackets using HCPs (Chapter 6).

4. Monitoring electron-ion recombination of field ionized wavepackets using HCPs [12].

5. Bound state interferometry of a Rydberg wavepacket (Chapter 7).

6. Observation of non-exponential decay of an auto-ionizing two-electron atom (Chapter 7).

Experiments 1, 2 and 4 involve counter propagating pump and probe pulses, whereas there is a $\sim 20^{o}$ angular separation between beams in experiment 3 and the beams are nearly co-propagating in experiments 6 and 7 [13].

In addition to greatly reducing the time required to make precision measurements, the imaging detector also provides real-time feedback to the temporal dynamics of

the system being studied. The dynamics are clearly displayed on the television monitor and the oscilloscope allowing quick and efficient optimization and maintenance of experimental parameters. Parameter spaces, in addition to time, can be explored in minutes, as opposed to hours, eliminating problems encountered with experimental drifts. Experiments previously thought to be too time consuming are readily performed with the imaging detector. Drastic reductions in data acquisition times and real-time feedback of time-dependent phenomena certainly make the single-shot imaging detector a potentially useful tool in coherent control experiments [14].

Bibliography

[1] L.D. Noordam and R.R. Jones. *J. Mod. Opt.* **44**, 2515 (1997).

[2] R.R. Jones and L.D. Noordam. *Advances in Atomic, Molecular and Optical Physics* **38**, 1 (1997).

[3] D.W. Schumacher, D.I. Duncan, R.R. Jones and T.F. Gallagher, *J. Phys. B: At. Mol. Opt. Phys.* **29**, L397 (1996). L.D. Noordam, D.I. Duncan and T.F. Gallagher, *Phys. Rev. A* **45**, 4734 (1992). R.R. Jones, D.W. Schumacher, T.F. Gallagher and P.H. Bucksbaum, *J. Phys. B: At. Mol. Opt. Phys.* **28**, L405 (1995). R.R. Jones, C.S. Raman, D.W. Schumacher and P.H. Bucksbaum, *Phys. Rev. Lett.* **71**, 2575 (1993).

[4] R.R. Jones, *Phys. Rev. Lett.* **76**, 3927 (1996).

[5] C.S. Raman, C.W.S. Conover, C.I. Sukenik and P.H. Bucksbaum, *Phys. Rev. Lett.* **76**, 2436 (1996).

[6] C.O. Reinhold, J. Burgdörfer, M.T. Frey and F.B. Dunning, *Phys. Rev. A* **54**, R33 (1996).

[7] G.M. Lankhuijzen and L.D. Noordam, *Opt. Comm.* **129**, 361 (1996). G.M. Lankhuijzen and L.D. Noordam, *Phys. Rev. Lett.* **76**, 1784 (1996).

[8] Jean-Claude Diels and Wolfgang Rudolph. *Ultrashort Laser Pulse Phenomena.* Academic Press (1996).

[9] John T. Fourkas, Lisa Dhar, Keith A. Nelson and Rick Trebino.*J. Opt. Soc. Am. B* **12**, 155 (1995).

[10] The single-shot detector is a combination of a single-shot autocorrelator and an atomic streak camera, in that it spatially images the relative position of ion (or electron) formation.

[11] Thomas F. Gallagher. *Rydberg Atoms.* Cambridge University Press (1994).

[12] Thomas J. Bensky, *Classical Rydberg Electron Interactions with Half Cycle Pulses.* Ph. D. Thesis. University of Virginia (1998).

[13] Spatial imaging of the relative position of ion (electron) formation can be used for experiments other than pump-probe measurements. A non-uniform electric field along the slit of the detector allows a continuous Stark map to be produced with simply an adjustment of laser frequency. This experiment is being performed by S. Pisharody and J. Zeibel.

[14] Warren S. Warren, Herschel Rabitz and Mohammed Dahleh, *Science* **259**, 1581 (1993).

Chapter 4

Radial Wavepacket Evolution

4.1 Introduction

Manipulation of the electronic configuration in an atom with electromagnetic radiation is an underlying theme motivating this research, and understanding the interaction of the atom with applied radiation fields is essential for this to happen. We choose dynamic atomic systems, or electronic wavepackets, as mini-laboratories to study the atomic response to intense laser fields. Not only are electronic wavepackets fundamentally interesting, they possess the time dependence that is intrinsic to more complicated atomic and chemical processes. Gaining a better understanding of the response of electronic wavepackets to various radiation sources builds a foundation of knowledge that can be used to help realize the ability to control chemical reactions with light [1, 2].

The radial wavepacket is a well-understood non-stationary atomic system and has been intensely studied theoretically and experimentally throughout the past 15 years [1, 2, 3, 4, 5, 6, 7], coinciding with the advent of high-intensity, short pulsed lasers. Most of these studies involve detection of the wavepacket when it is near the atomic core using bound state interferometry [1, 2, 8] and explore the creation and detection

of a wavepackets with short optical laser pulses. A newly developed radiation source, which produces half-cycle pulses (HCPs) of THz radiation [9, 10], has made it possible to probe radial wavepacket dynamics, particularly when the wavepacket is far from the atomic core. This Chapter presents an experiment that probes the dynamics of a radial wavepacket using HCPs in a novel, thorough way. Radial wavepacket evolution has previously been monitored using HCPs [4], but here the full, time-dependent probability distribution of such a wavepacket is measured. The results of the experiment allow us to gauge our understanding of the experimental techniques and determine the circumstances under which these techniques may be used with more complicated systems.

A radial wavepacket is an atomic system that is charactarized by dynamics only along the radial coordinate, with no changes in either the polar or azimuthal coordinates [1, 2]. We studied a wavepacket made up of Rydberg eigenstates having identical angular momentum and azimuthal quantum numbers, ℓ and m. Rydberg states are used for many reasons. The narrow energy spacing between Rydberg levels allows a single, broadband, short optical light pulse to simultaneously excite several eigenstates. Also, Rydberg eigenenergies and wavefunctions are very well determined [11], making the analysis quite rigorous.

The fundamental period of motion of a Rydberg wavepacket is equal to the Kepler period, $\tau_K = 2\pi N^3$, of a classical electron with energy, $E = 1/2N^2$, where N is the average principle quantum number of the constituent eigenstates. This relationship demonstrates how the study of Rydberg wavepackets walks the hazy boundary between quantum and classical physics. The period of Rydberg wavepackets is typically measured in picoseconds, that makes sub-picosecond HCPs attractive tools for the study of wavepacket evolution. Using HCPs, we directly measure the momentum-

space probability distribution of a radial wavepacket which exhibits dynamics on this time scale.

4.2 Experiment

Between two 7.5 × 7.5 cm^2 electric field plates, ground state $4s4s\,^1S_0$ calcium atoms in an effusive, thermal beam are excited to an intermediate $4s4p\,^1P_1$ state with a 423 nm, 5 nsec dye laser pulse. The dye laser is Hansch style, as described in the apparatus section, and is pumped with the 355 nm third harmonic of the Nd:YAG laser. The laser uses Stilbene 420 dye, which fluoresces in the appropriate frequency range. Fewer than five nanoseconds later, a $4snd\,^1D_0$ wavepacket is created with a 500 fsec, 392 nm laser pulse. The short laser pulse is a frequency doubled 786 nm, 120 fsec pulse generated in the mode-locked Ti-sapphire regenerative amplifier. The pulse results from a single pass through a 1 cm potassium dihydrogen phosphate (KDP) doubling crystal. Phase matching in the doubling crystal restricts the bandwidth to about 30 cm^{-1}. Both laser beams are linearly polarized along the z axis, so the z-projection of angular momentum in the *nd* wavepacket is zero. Sufficient bandwidth in the laser pulse simultaneously excites a distribution of eight $\ell = 2$, $m_\ell = 0$ states centered on $N = 32.9$. We probe the wavepacket with HCPs of THz radiation [9, 10] polarized both vertically ($\hat{z}$) or horizontally ($\hat{x}$). The interaction of a HCP with the wavepacket is discussed later in this chapter. The ionization probability of the wavepacket is measured as a function of HCP amplitude and delay for each HCP polarization direction. This measurement provides the momentum-space probability distribution along both the $\hat{x}$ and $\hat{z}$ axes.

The relative amplitudes of the contributing states in the wavepacket are measured using state-selective field ionization (SSFI) [11]. Different states contributing to the

wavepacket ionize at different electric fields. A slowly increasing (about 1 kV in 3 microseconds) ionization pulse is applied to the bottom field plate. Ions created by the pulse are pushed through an opening in the top field plate by the applied field pulse and arrive at the detector at times corresponding to the binding energy. Typically, electrons are best suited for SSFI because their time-of-flight to the detector is small compared to the time scales of the changing field pulse. Ions are much heavier and reach the detector more slowly than electrons. Problems may arise when ions must traverse long flight paths. For example, ions created by small electric fields are weakly removed from the atom-laser interaction region. Ions created in large electric field, however, are highly accelerated towards the detector. Given a long flight path, the ions created in the stronger field may surpass the initial slow moving ions, and distortion of the relative arrival times of ions from different eigenstates may occur. In the single-shot imaging detector, the interaction region and microchannel plate pair are separated by ~ 2 cm. The short separation distance temporally resolves the arrival of different n-state ions.

The highest energy states arrive first because they are stripped from the atom with the lowest electric field. A high-pass filter is connected to the phosphor screen and allows the AC voltage to be monitored with an oscilloscope. A negative voltage represents electrons striking the phosphor screen. A plot of the oscilloscope voltage (reversed for the figure) representing the ionization of the wavepacket vs. time due to a slowly rising field ionization pulse is shown in Figure 4.1. The largest peak is the $n = 33$, $n^* = 31.77$ state (n^* is the effective principle quantum number when the quantum defect, $\delta_{n=33,\ell=2} = 1.23$, is considered).

Figure 4.2 shows an overhead view of the experimental setup. Both excitation lasers propagate along the long slit in the top field plate. The HCP probe propagates

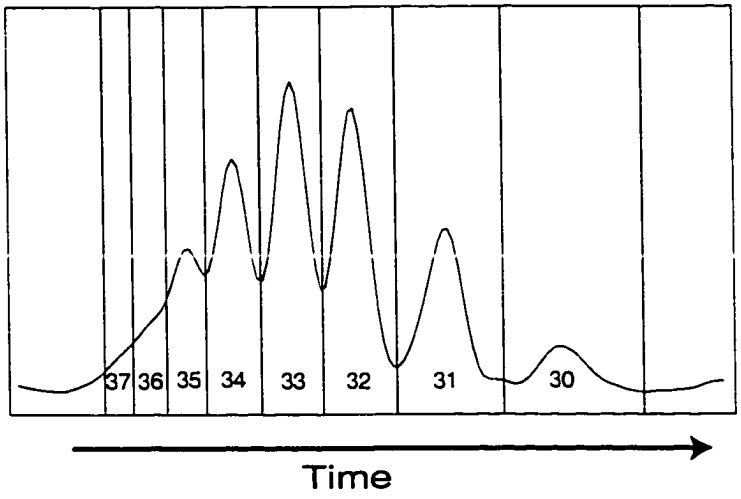

Figure 4.1: Oscilloscope trace demonstrating relative eigenstate amplitudes in a wavepacket using state-selective field ionization. The curve plots the relative voltage level as a function of time as different eigenstates arrive at the detector. The numbers correspond to the principle quantum number of each contributing $4snd$ eigenstate of the wavepacket. Higher n-states are ionized at lower electric fields and arrive at the detector earlier.

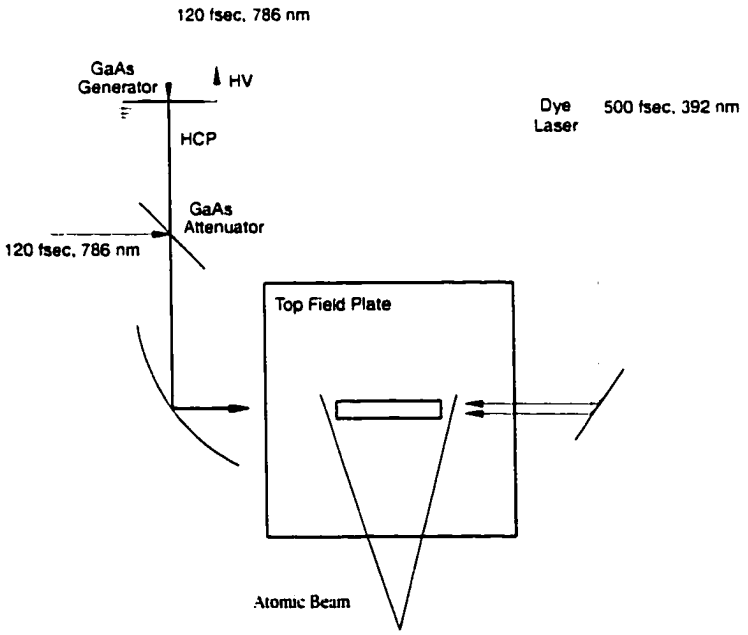

Figure 4.2: Overhead schematic of the experiment. The pump optical pulse and the probe HCP counterpropagate along the long dimension of the slit in the top field plate.

in the opposite direction and is produced by a biased GaAs wafer. The wafer is used as a fast photo-conductive switch that is gated by the short laser pulse. The generated electric field is polarized along the field axis of the wafer and scales linearly with the applied voltage. The wafer used in the HCP production is mounted on a rotation stage allowing continuous adjustment of the polarization of the pulse about its propagation axis. The upper limit on the HCP amplitude is restricted by the pickup of noise by the phosphor screen and by the durability of the GaAs wafer. We find that it is also worthwhile to apply less than 60 volts to the high voltage transformer switch to keep the wafer from shorting out.

4.2.1 HCP 'Cleaning'

Each HCP has undesirable, non-unipolar components resulting from two primary effects. First, a long negative tail occurs due to the relatively slow deceleration of the electrons in the GaAs wafer. Second, a reflection of the main HCP off the back side of the wafer produces a short, low-amplitude, oppositely polarized pulse that propagates about 11 psec behind the main HCP. Unwanted components are (mostly) removed via HCP 'cleaning' with a second GaAs wafer [12]. The unbiased wafer is positioned at a 45 degree angle with respect to the propagation direction of the HCP and its conductivity is gated by a portion of the 786 nm, 120 fsec light. The beam geometry is shown in Figure 4.2. The 120 fsec pulse illuminates the unbiased wafer approximately 2.5 psec after the HCP has passed, sending it into a conductive state. The abundance of free charge in the wafer prevents most of the late-arriving, unwanted electric fields from reaching the atom/laser interaction region.

Once illuminated, the cleaning wafer decreases the HCP field amplitude by approximately 75 percent. We measure the attenuating ability of the wafer by comparing

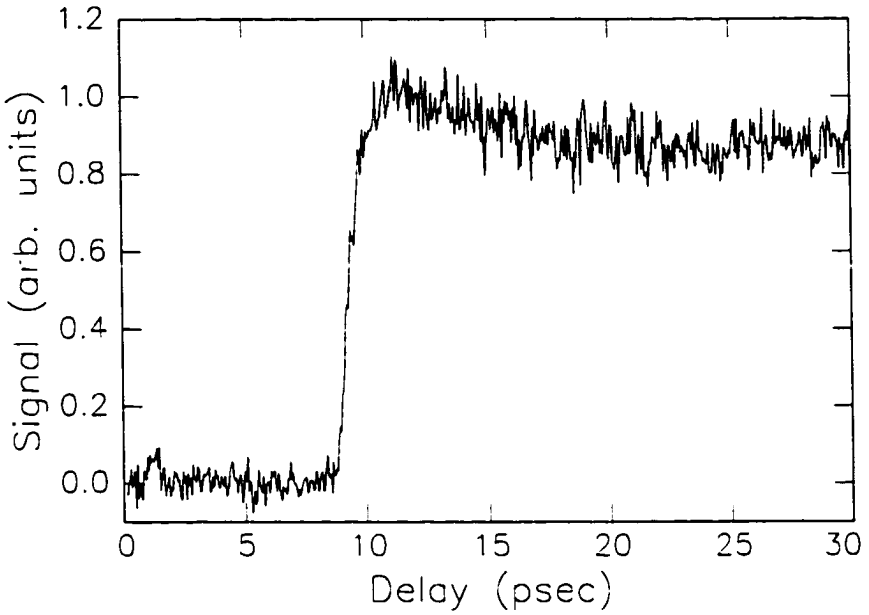

Figure 4.3: Plot of HCP ionization of a Rydberg eigenstate as a function of when the unbiased, attenuating GaAs wafer is illuminated. The large peak at about 11 psec corresponds to main HCP transmission, but non-unipolar components of the pulse are blocked.

the ionization probabilities of a Rydberg eigenstate for a fixed, large amplitude HCP when the HCP is transmitted or attenuated. The ionization of a Rydberg eigenstate due to HCPs is well understood [10, 12, 13] and the relative ionization probabilities relate directly to the relative field strengths of the HCPs.

Illumination of the attenuating wafer at precisely the right time is necessary. The trace in Figure 4.3 shows the ionization of a Rydberg eigenstate due to a HCP of constant amplitude as a function of delay of the laser pulse that illuminates the attenuating wafer. Initially, the ionization level is low, then it quickly rises to a maximum value in about 2.5 psec. The signal level drifts towards a lower level and remains constant for long (tens of picoseconds) delays. Previous measurements of the same effect have shown a return of the ionization probability up to, and even

surpassing, the initial maximum [12]. The second maximum results from the arrival of the reflected pulse about 11 psec after the initial HCP. The signal represents the integrated brightness of the phosphor as a delay stage that controls the arrival of light to the attenuating wafer is translated. In this experiment the HCP passes through the attenuating wafer before being collected by a large parabolic mirror and focused into the atom/laser interaction region, which differs from the experimental setup used by Tielking *et al.* [12]. We propose that the large distance between the attenuating wafer and the interaction region, and the attenuating wafer's reflective and dispersive characteristics prevent the secondary HCP from measurably interacting with the sample of atoms. For all measurements presented here, the cleaning GaAs wafer was illuminated $\sim$ 2.5 psec after the main HCP has passed through, at the peak in Figure 4.3. The 'turn-on' time of the ionization represents the convolution of the HCP and the transition of the unbiased wafer to the conducting band. The 2.5 psec rise of the ionization curve indicates the HCP is stretched out to about 1 psec FWHM after passing through the unbiased wafer, which may be attributed to velocity dispersion in the GaAs wafer of the THz frequencies contributing to the pulse.

The attenuating wafer alters the transmitted field of the HCP even when the wafer is not illuminated due to portion of the HCP reflecting off the GaAs surface. Because the wafer is positioned at 45 degrees with respect to the HCP propagation direction, the decrease in field amplitude strongly depends on the polarization of the HCP. Vertically polarized (σ-polarized) HCPs are significantly more attenuated than horizontally polarized (π-polarized) pulses. The relative field strengths are calculated by taking the ratio of the transmission coefficients,

$$\frac{\tau_\sigma}{\tau_\pi} = \frac{n' \cos\theta + n \cos\theta'}{n \cos\theta + n' \cos\theta'} = 0.83,$$

where $n = 1$ is the index of refraction in vacuum, $n' \approx 3.6$ is the index of refraction

of the GaAs wafer. $\theta = 45^o$ is the angle of incidence, and $\theta' \approx 11^o$ is the angle of transmittance in the wafer. Because the HCP passes through two vacuum- GaAs surfaces, the total field varies as the square of the transmission coefficient, meaning the σ-polarized pulse has a field strength of about 70% of the π-polarized pulse.

4.2.2 Data Acquisition

We measure the ionization of the radial wavepacket as a function of both HCP delay and amplitude to retrieve the momentum distribution of the radial wavepacket along the $\hat{x}$ and $\hat{z}$ directions. The single-shot detector spans this two dimensional parameter space. The pump and probe beams pass in opposite directions along the long slit in the top electric field plate. In this configuration, the relative delay between pump and probe pulses for atoms separated by a distance, d, is given by $\Delta\tau = 2d/c$ where c is the speed of light. The total delay range for counter-propagating beams for this detector is about 100 psec. With each firing of the laser system we are able to monitor the response of the wavepacket to a HCP over a 100 psec window of its evolution. Therefore, by simply scanning the HCP amplitude we measure the ionization as a function of HCP amplitude *and* delay.

50 nsec after the HCP passes through the sample of atoms, ions created by the HCP are pushed out of the interaction region by a +50 V pulse applied to the bottom field plate. With their relative spatial separation intact, the ions strike a microchannel plate pair, and the subsequent electron burst is accelerated towards a 0.75 inch phosphor screen. On impact, the phosphor fluoresces, and the relative brightness levels are recorded with a CCD camera. The image of ion formation in the interaction region spans over 40 lines of the video screen, yet the data acquisition software monitors only a single line of the video output in real time. Although the imaging detector

preserves the relative spacing of ion formation along the time axis. ion focusing in the dimension perpendicularly to the extraction slit limits the ion signal along any given line of the video image. New software is currently available that allows for the full video image to be recorded which further reduces data acquisition time.

For each of 50 HCP amplitude steps, the ionization vs. time is averaged over 300 laser shots for both horizontal and vertical HCP polarizations. The HCP amplitude is proportional to the voltage applied to the GaAs wafer. Data acquisition software regulates the high-voltage (ranging from $0 - 8$ kV), 100 μsec voltage pulse applied to the wafer that is supplied by a ($> 50\times$) car transformer. Voltage pulses sent through the computer's parallel port drive a stepper motor attached to the voltage knob on the HP power supply. The motor moves a fixed number of steps that corresponds to a set ($\sim$ 1 V) voltage change to the DC voltage input of the transformer. The change in voltage occurs in less than half of a second and is considered instantaneous relative to the 20 second measurement time at each voltage level. The camera output is sent to a video-triggered Tektronix 410A oscilloscope which has a GPIB connection with the data acquisition computer. A single digitized line of the video output is averaged 300 times at each HCP amplitude and is discretized into 300 time bins. Non-uniform ion focusing along the time-axis occurs as the ions travel from the atom-laser interaction region to the detector. A slightly different potential gradient exists near the ends of the slit in the top field plate. Therefore, ions leaving the interaction region will cause a non-perfect linearity between position and delay across the image. To correct this effect, the relative position of the 'turn-on' of the ionization signal and the subsequent image structure are monitored as the delay stage of the 392 nm light is varied. This changes the position of $t = 0$, where the pump and probe pulse overlap in time. Mapping the position of $t = 0$ over the entire delay range of the detector gives a

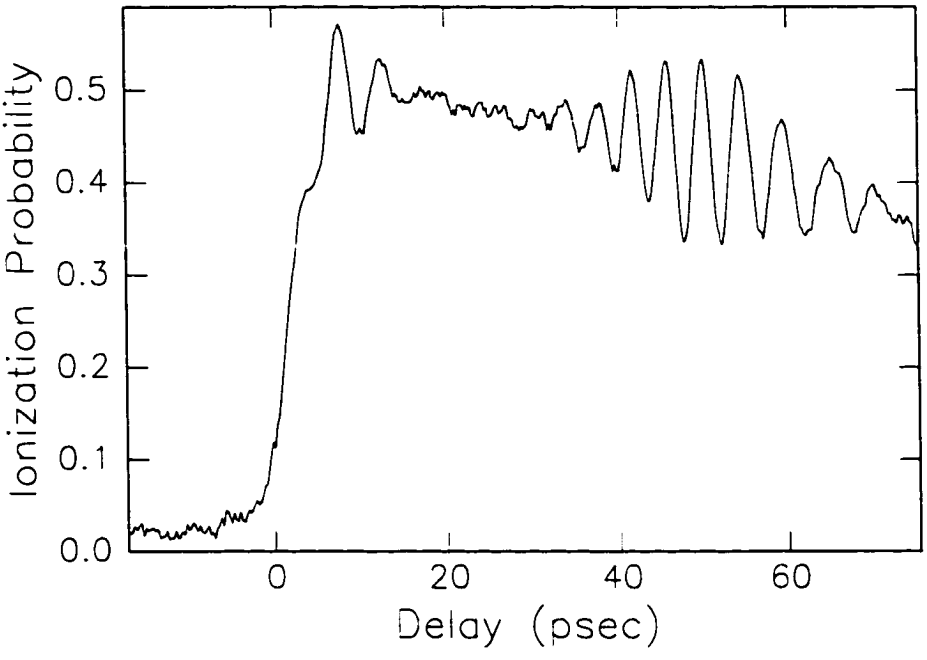

Figure 4.4: Plot of ionization versus time of a radial wavepacket due to a HCP of THz radiation. The curve shows the average of 300 pump-probe measurements.

quadratic function relating position to time.

A plot of the ionization probability of the radial wavepacket due to a HCP as a function of time is shown in Figure 4.4. The oscillations in the curve are due to changes in the momentum distribution of the radial wavepacket as it breathes in and out from the atomic core. Peaks in the signal at low HCP amplitudes indicate times when the wavepacket is near the core. The wavepacket has the highest probability of having a large momentum component along the HCP field axis at this time. Larger HCP amplitudes (as is the case in Figure 4.4), elicit features in the ionization probability versus HCP curve that do not provide direct information about the position of the wavepacket along its orbit. Therefore, the wavepacket may not be localized near the core at the peaks in the curve. The ionization probability is discussed in more

detail later in this Chapter.

Three hundred single line traces are averaged together to produce the curve in Figure 4.4. Image analysis must be performed when considering the non-uniform response of the imaging detector to incident ions. A zero signal scan is taken by placing the lens cap on the CCD camera. This provides the response of the camera to no signal. A background scan is also taken by measuring the signal on the camera when the wavepacket excitation lasers, but no HCP, pass through the atom/laser interaction region. A very weak signal is produced by a small portion of bandwidth in the laser beam that overlaps an auto-ionizing state. The camera's response to a uniformly bright signal is needed to compensate for inhomogeneities of the detector's response. A saturation curve is produced by measuring the ionization signal due to a large amplitude HCP that is strong enough to ionize 100 percent of the wavepacket population, irrespective of where the wavepacket is in its orbit. To determine the final ionization probability, the zero and background traces are subtracted from both the signal and saturation curves. The signal curve is divided by the saturation curve, giving the precise measurement of the relative ionization as a function of time for a given HCP. The relative brightness level for each pixel, i is given by,

$$B_i = \frac{S_i - Bk_i}{Sat_i - Bk_i},$$

where B_i is the brightness, S_i is the recorded signal, Bk_i is the background, and Sat_i is the saturation signal at pixel i. Although calibrated, the curve in Figure 4.4 drifts downward slightly at large delays. Slight focusing of the ions along the time axis near long times (near the edge of the slit) may be responsible for the drift. Ions formed beyond the edge of the slit in the top field plate, representing delays greater than 70 psec, may be expelled from the interaction region towards the detector. The signal at large times may be erroneously increased in the saturation curve. When the signal is

divided by the saturation curve, the disproportionally large values of the saturation curve decrease the final ionization probabilities at long times.

4.2.3 Impulsive Momentum Retrieval

A HCP of THz radiation is an extremely useful tool used to monitor wavepacket evolution. Over the past several years, the interaction of a HCP of electromagnetic radiation with Rydberg atoms has been well studied [13, 14, 15, 16, 17], and the atomic response to HCPs is becoming well understood. The pulse lasts $\sim$ 1 psec and is (generally) relatively short compared to the timescales of the evolving radial wavepacket. The Kepler period for an $N = 32.9$ wavepacket is about 5 psec. Therefore, the HCP acts as a fast shutter which captures the motion of the wavepacket at a given point in its orbit. An optical laser pulse has an electric field that rapidly oscillates about zero. Due to momentum conservation, an electron can only exchange energy with the laser pulse when it is positioned near the atomic core. The time-integrated electric field of the HCP is non-zero, and it may exchange energy with the wavepacket even when it is far from the atomic nucleus. HCPs are the first radiation source allowing continuous monitoring of the wavepacket throughout its trajectory.

The discussion presented here on impulsive momentum retrieval (IMR) [5] is based on classical arguments. A HCP gives an electron a momentum 'kick' along the polarization axis of the pulse. The momentum changes from its initial value, $\vec{p}_o \Rightarrow \vec{p}_o + \vec{A} = \vec{p}$, where $\vec{A}$ is the impulse delivered to the electron by the HCP.

$$\vec{A} = -\int \vec{F}(t)dt.$$

The change in energy of the wavepacket is given by

$$\Delta E = (\vec{p}^2 - \vec{p}_o^2)/2 = \vec{p}_o \cdot \vec{A} + \vec{A}^2/2. \tag{4.1}$$

If the change in energy is greater than the binding energy of the wavepacket, $E_n = -1/2N^2$, the electron is free to leave the atom and the remaining ion is detected. We arrive at a relation between the momentum of the wavepacket along a given axis, p_{o_i}, the impulse delivered by the HCP along that axis, A_i, and the mean principle quantum number of the wavepacket, N.

$$p_{o_i} = (\frac{1}{N^2} - A_i^2)/2A_i. \tag{4.2}$$

The probability distribution along the HCP polarization axis is simply the scaled derivative of the measurement of ionization probability of the wavepacket as the HCP amplitude is increased for a fixed time delay.

A series of ionization probability versus time curves, similar to that found in Figure 4.4, is taken over 50 different HCP amplitudes. Each curve is discretized into 300 data points and the data is resorted to give ionization probability versus HCP amplitude curves at 300 delay times. We extract the momentum distribution from these curves.

Previous ionization experiments agree with classical calculations. Therefore, we calibrate the impulse delivered by the HCP by equating the impulse at the 50% ionization level of the wavepacket at $t = 0$ to $A = 1/N$, where N is the average principle quantum number of the wavepacket. The peak HCP field scales linearly with the bias voltage on the GaAs wafer, and the impulse scales with HCP field. Thus, the momentum, or impulse, axis is fully calibrated with the determination of the 50 percent ionization level.

Once the impulse axis is calibrated, a spline [18] fit of the data is generated. We take the derivative of a spline fit, giving a $\frac{dI}{dA}$ vs. A curve, where I represents ionization probability. To preserve normalization, the vertical axis is scaled by a factor of $2A^2/(\frac{1}{N^2} + A^2)$. Finally, the impulse axis is converted to momentum coordinates

producing a $|\psi(p_i)|^2$ vs. p_i probability distribution curve (i represents a Cartesian axis). The integral of this curve is one, ideally, but varies in the measurements by about 10 percent for measurements along $\hat{x}$. To increase the resemblance of the spline fit to the data at low HCP fields, five uniformly spaced zero amplitude points are added to the beginning of each ionization probability versus HCP amplitude curve.

4.2.4 Probability Distribution Measurements

The time dependent momentum-space probability distributions for a $4sNd$ radial wavepacket in calcium, where the mean principle quantum number $N = 32.9$, along the $\hat{x}$ and $\hat{z}$ coordinates are shown in Figure 4.5. The distributions, $\mathcal{P}_z$ and $\mathcal{P}_x$, each have prominent characteristics that are explained in terms of the wavepacket's evolution. The HCP amplitude is limited due to the presence of the attenuating GaAs wafer. Therefore, we do not have sufficient field strength to measure large positive values of p_i. This is especially true in the measurement of $\mathcal{P}_z$ because a large portion of the vertically polarized HCP is reflected away by the attenuating wafer. Nevertheless, we observe anticipated structure in the momentum distributions. In subsequent experiments we bypass the problem of limited HCP field strength along orthoganal axes by recognizing a symmetry in the interaction of a HCP and a wavepacket.

At its creation ($t = 0$), the wavepacket is located near the atomic core, has a high probability of having large momentum values, and has a wide distribution. When the wavepacket is localized, we observe a 'breathing' in the momentum distributions. At the outer turning point of its highly elliptical orbit, the wavepacket is moving very slowly. The momentum distribution narrows and is sharply peaked at $p_i = 0$. In time, the distinct sharp peaks are separated by 5.4 psec, the Kepler period

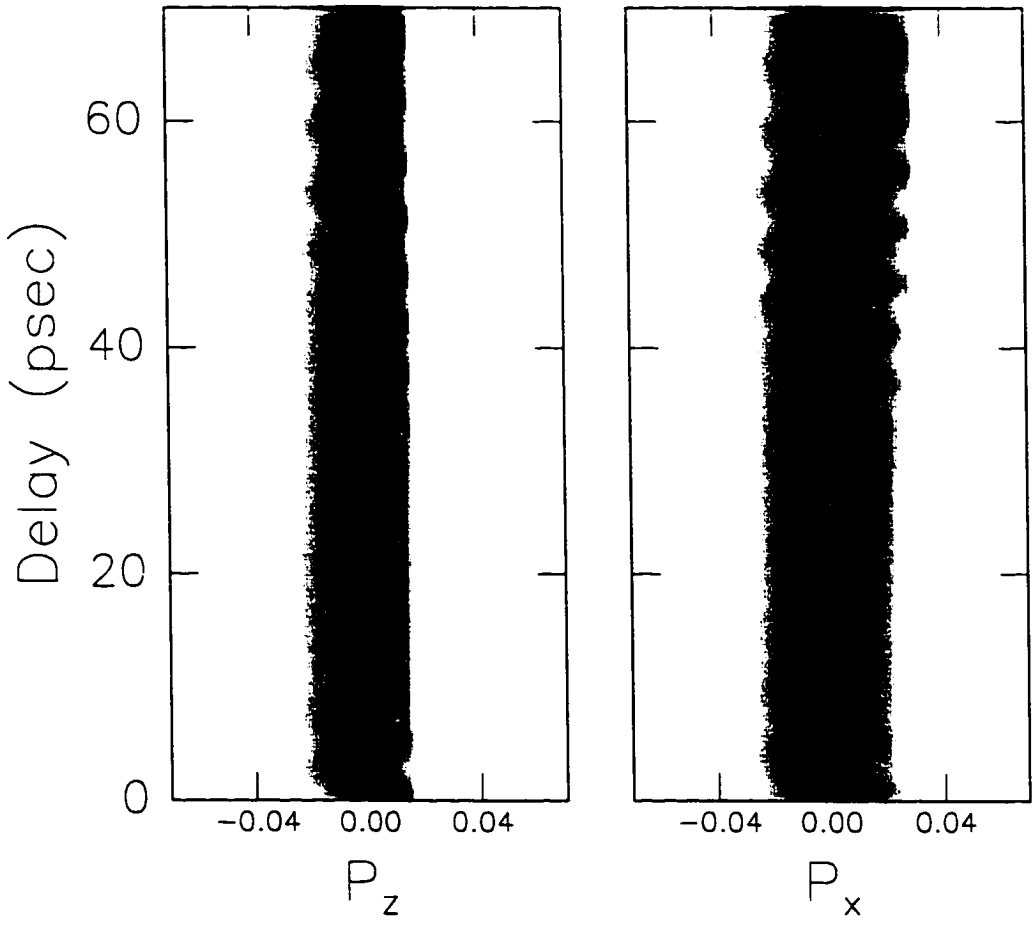

Figure 4.5: Measured momentum-space probability distributions along the A.) z and B.) x axes. The distribution along the z axis is cut off prematurely due to restricted HCP amplitudes along this axis. Dark shading indicates higher probability.

for this wavepacket, and represent the times when the radial wavepacket is at its outer turning point. The contributing states in the wavepacket quickly de-phase, and the momentum distribution is relatively static until about 40 psec. At this time a full-revival of the momentum oscillations is observed and is strongest at ~50 psec. During the revival, the wavepacket behaves similarly to when it was first excited and a breathing of the probability distribution is observed along both axes. For completeness, the ionization probability of the wavepacket due to oppositely polarized ($-\hat{x}$ and $-\hat{z}$) HCPs has been measured. These and the original measurements are identical, indicating the radial wavepacket has no asymmetries along any axis.

4.3 Analysis

Closer inspection of the measured probability distribution shows a pronounced asymmetry about zero momentum when the wavepacket is localized (near $t = 0$ and during the revival) and near its inner turning point. The asymmetry is persistent and consistently appears as a shift of the momentum distribution towards high values, independent of the polarization of the HCP.

True asymmetry in the probability distribution of a radial wavepacket results in temporal characteristics in the ionization probability that appear to be perfectly out of phase for oppositely polarized HCPs. However, this is not the case. Ionization probability curves are identical for oppositely polarized HCPs, indicating the asymmetric probability distributions are due to an artifact of the experimental method and/or a breakdown of the IMR method. To determine the origin of measured asymmetry, a comparison is made between measured probability distribution evolution and both quantum and classical calculations of the distribution. These comparisons demonstrate the capabilities and limitations of our methods.

First, we compare our measurement to a quantum calculation of the momentum distribution. The simulation considers $4snd$ ($31 \leq n \leq 37$) eigenstates of calcium that contribute ~ 5 percent or greater to the wavepacket population, as measured with SSFI. We assume the amplitude of each state is real at its creation ($t = 0$). Each eigenstate has a corresponding wavefunction with a time dependent phase factor in which the phase is proportional to the energy of the state. The radial wavefunction, $U(r) = rR(r)$, for each nd state is calculated numerically using a Numerov routine. The momentum-space wavefunction is generated by evaluating the wavefunction, $p_r\phi(p_r)$, at each value of p_r using the approach of Podolsky and Pauling [19] relating $\phi(p_r)$ to $R(r)$

$$\phi(p_r) = \sqrt{\frac{2}{\pi}} \int_0^\infty j_l(p_r r) r^2 R(r) dr. \tag{4.3}$$

where $j_l(p_r r)$ is the spherical Bessel function of order ℓ, and ℓ is the angular momentum quantum number. The momentum-space wavefunctions are used to propagate the wavepacket in time, where the total wavefunction is given by

$$\Psi(p_r, t) = \sum_n a_n e^{-i(E_n t - \phi_n)} \psi_{n,l=2}(p_r). \tag{4.4}$$

The projection of the time dependent momentum-space probability distribution along the $\hat{x}$ and $\hat{z}$ coordinates gives us the time-dependent probability distributions along those axes. The calculated distribution along p_x shown in Figure 4.6. represents the evolution of a wavepacket that was created instantaneously, and ϕ_n is set to zero for each eigenstate. Figure 4.7 shows the same calculation after it has been smoothed by a 1.5 psec Gaussian time window, which better represents the resolution of the detector. Our measurement of the momentum-space probability distribution is more complete along p_x, so we present the calculation along this axis.

Qualitative agreement is present between the calculation and the measurement.

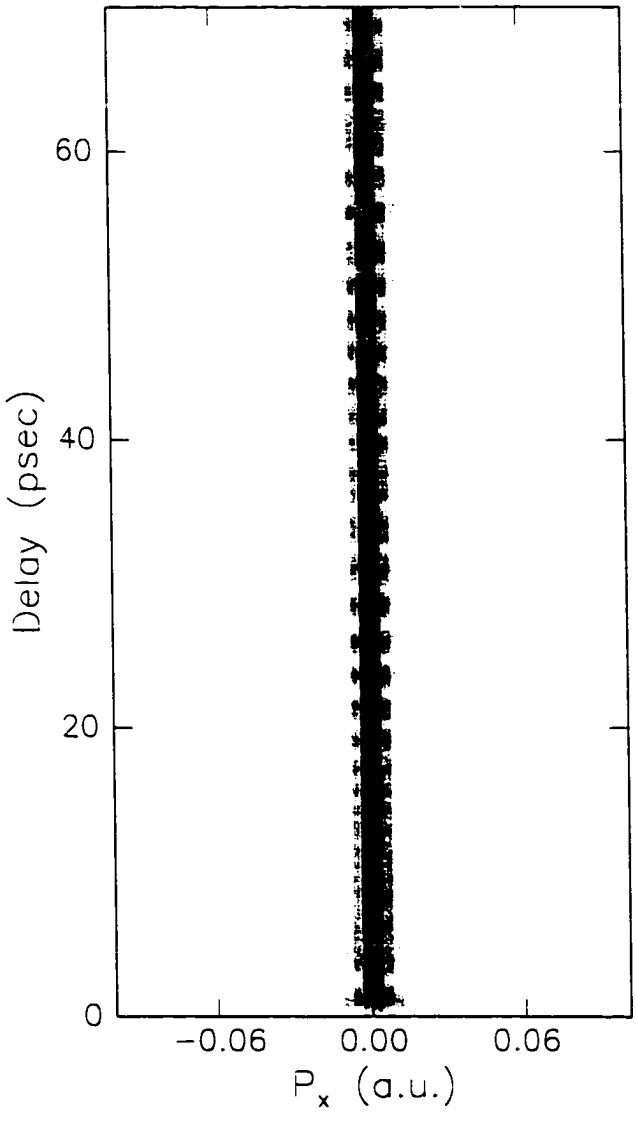

Figure 4.6: Quantum calculation of the momentum-space probability distribution for a radial wavepacket along the x axis. The distribution is perfectly symmetric about zero at all times. Notice evidence of a fractional revival near 25 psec.

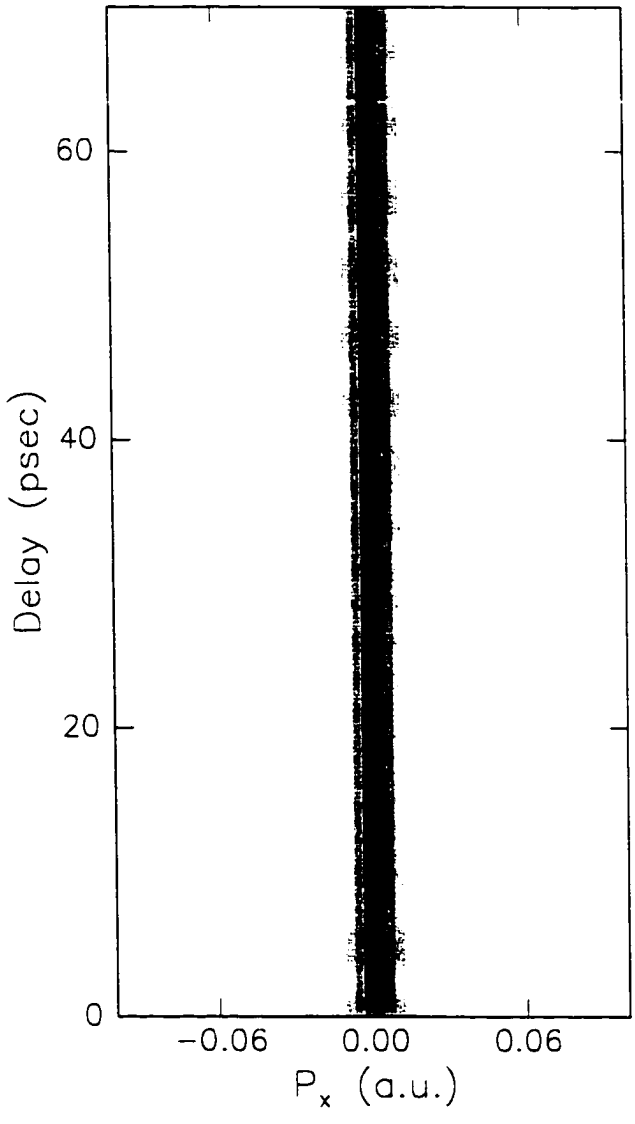

Figure 4.7: Same distribution as seen in Figure 4.6, but is time averaged over a 1.5 psec Gaussian shaped window, which emulates the resolution of our measurements. Time averaging prevents observation of fractional revivals [20].

The distribution is broad at the creation of the wavepacket when it moves quickly away from the atomic core. The distribution subsequently collapses into a sharp peak when the wavepacket reaches its outer turning point. The states quickly dephase, and the distribution remains relatively static until the full revival around 50 psec into the evolution. A fractional revival in the momentum distribution is seen in Figure 4.6 near 20 psec, but it is not observable when the detector response is considered. However, we notice the distribution is always perfectly symmetric about $p_z = 0$. Radial wavepackets have no 'sidedness' and always have equal probability to move up and down, or left and right. Thus, the calculated symmetry is expected. As mentioned earlier, the asymmetry seen in the measurement must be a result of the wavepacket probing technique and is not an intrinsic characteristic of the wavepacket. A full quantum simulation of the interaction of the wavepacket with a HCP [15] is not presented here. All accessible bound states (in n, ℓ and m), as well as continuum states, must be considered in such a calculation, making it a non-trivial computational task.

However, we consider the classical interaction of an electronic wavepacket with a HCP. Because we are working with Rydberg states, we can approximate the characteristics of the wavepacket through the statistical analysis of an ensemble of classical electrons in a Coulomb potential interacting with a HCP [21]. The electron distribution is launched in a spherical shell near a hydrogenic nucleus with a range of energies and well defined angular momentum. The energies are discretized and weighted according to the eigenstate distribution of the experimental wavepacket. A fifth-order Runge-Kutta algorithm integrates the classical equations of motion for the electron distribution. At some time after its launch, the ensemble is subject to a Gaussian HCP. The width of the HCP is an adjustable parameter of the simulation. After

the interaction, the fraction of the ensemble with positive energy gives the ionization probability for that HCP field and delay. The calculation is repeated for the range of fields needed to saturate the ionization probability over a desired range of time delays, running analogously to the experiment. The ionization probability versus HCP field curves are treated identically to the experimental data, and the momentum-space probability distribution along $\hat{x}$ is extracted. The results are smoothed in time with a 1.5 psec window to account for the 0.5 psec excitation time of the wavepacket and the resolution of the detector.

Figures 4.8 and 4.9 show the time dependent momentum distribution of the classical simulation for HCP widths of 100 fsec and 1 psec, respectfully. The two distributions are clearly different. For a 100 fsec pulse, which would be ideal for IMR measurements, but is not currently attainable in the laboratory, the momentum distribution is symmetric about zero as seen in the quantum calculation. The 1 psec pulse width results demonstrate an asymmetry about zero that is very similar to the measurement. Also, the 1 psec distribution appears narrower than the 100 fsec distribution. The differences between the two calculations can be explained classically. First, the electron distribution moves very rapidly when it is near the atomic core. Little time is required, roughly one-tenth of its Kepler period, for a Rydberg electron to move from the atomic core to half the outer turning point, where $r \approx n^2$. The small duration the electrons move at high velocity (in the wings of the distribution) lowers the rms value of the velocity while the distribution interacts with the HCP. A symmetric narrowing of the distribution occurs because the amplitude of large positive and negative portions of the distribution are reduced.

A second effect of the rapid motion of low angular momentum electrons near the atomic core involves a change in sign in the velocity while the electron interacts with

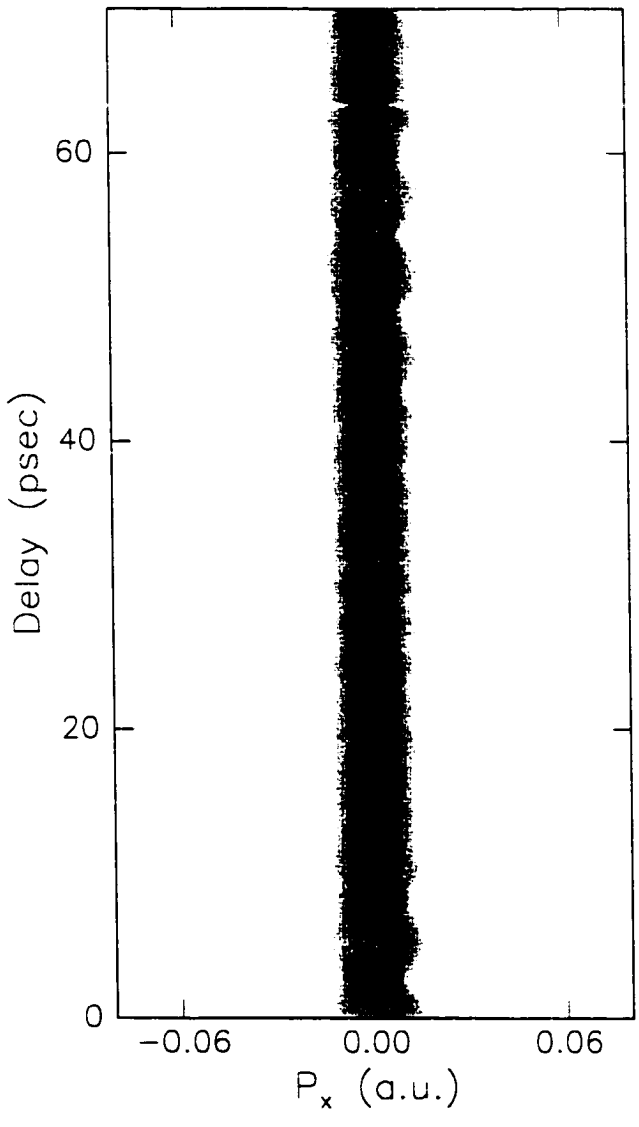

Figure 4.8: Classical calculation of the momentum distrubition along $\hat{x}$ for an ensemble of hydrogenic electrons probed with a 100 fsec HCP. The distribution resembles the quantum calculation and maintains symmetry about $p_x = 0$.

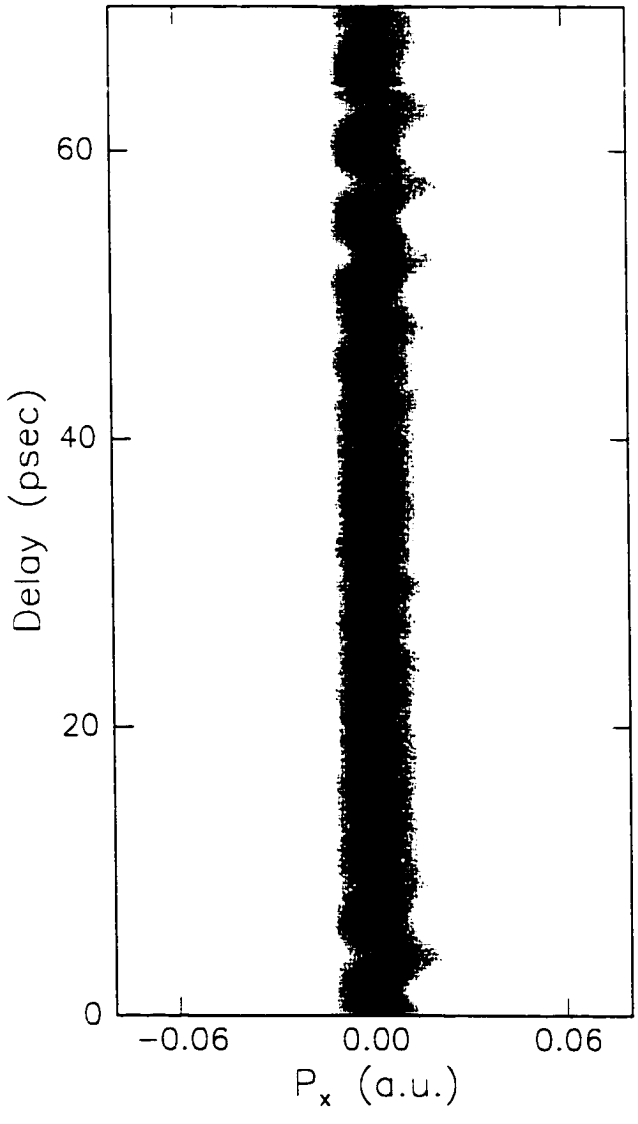

Figure 4.9: Classical calculation of the momentum distribution along $\hat{x}$ using a 1 psec HCP probe. Asymmetry along the momentum axis appears for the longer HCP and matches the measurement.

the HCP. The IMR method assumes the electron distribution is relatively motionless during its interaction with the HCP (hence the term 'impulsive'). For some of the electrons, the momentum gained (lost) from the HCP as it nears the core is perfectly canceled when its velocity changes sign and momentum is lost (gained) after it reflects off the atomic core. This effect makes it very difficult to ionize a portion of electron ensemble while it is near the core with an extended (1 psec) HCP. Higher fields are needed to ionize the electrons near the core, which results in weighting of the momentum distribution towards higher values. The cumulative effect of a finite HCP interacting with a rapidly moving wavepacket near the atomic core is a faster rising, slower decreasing probability distribution. The IMR method ensures accurate measurement of the time-dependent probability distribution for a radial wavepacket that is not localized near the atomic core.

The measured distribution shows an asymmetry in time in the evolution of the momentum distribution during each Kepler orbit. The cause of this is not clear and may result from purely quantum mechanical effects or imperfect characterization of the HCP. The probing HCP is certainly not perfectly Gaussian, so a faster rising edge of the pulse might make it more difficult to ionize the wavepacket when it is returning to the core (and increasing speed during its interaction with the pulse) than when it leaves the atomic core (and slowing down during its interaction with the pulse).

4.4 Measuring the Exact Wavefunction

We have developed a method to determine the complex phase of a radial wavepacket. Because the eigenenergies and wavefunctions of electronic Rydberg states are accurately known, our method is equivalent to the measurement of the time dependent wavefunction or quantum state of the system. For many applications of quantum

control, the ability to determine the exact state of an electronic system at a specific point in time is essential.

The technique presented here is rather straightforward. The evolution of the probability distribution in a radial wavepacket is determined by initial measurements of the ionization probability of a radial wavepacket due to a HCP as a function of time. We extract the complex phase for the wavepacket directly from these curves. A radial wavepacket in calcium made up of $4snd$ states can be described mathematically as,

$$\Psi(\vec{p}, t) = \sum_n a_n \psi_n(\vec{p}) e^{-i(E_n t - \phi_n)}, \tag{4.5}$$

where a_n are the real, time-independent amplitudes of the contributing eigenstates, $\psi(\vec{p})$ with energies E_n, and constant phase, ϕ_n. The time-dependent probability distribution is

$$\mathcal{P}(\vec{p}, t) = \sum_{n_1, n_2} a_{n_1} a_{n_2} \psi_{n_1}(\vec{p}) \psi_{n_2}(\vec{p}) e^{i(\Delta E_{n_2, n_1} - \Delta\phi_{n_2, n_1})}, \tag{4.6}$$

with $\Delta E_{n_2,n_1} = E_{n_2} - E_{n_1}$, and $\Delta\phi_{n_2,n_1} = \phi_{n_2} - \phi_{n_1}$. We have assumed the time-independent wavefunctions, $\psi_n(\vec{p})$ are real without loss of generality.

However, the probability distribution is not measured exactly. We measure the probability of the wavepacket having a momentum between some value $\vec{p}$ and $\vec{p} + \vec{\delta p}$ with HCP ionization, which is the integral of the probability distribution over that momentum-space volume element. More accurately, we measure the probability of the wavepacket having a momentum that falls within a momentum-space element along either the $\hat{x}$ or $\hat{z}$ axis. If we consider a range over large momentum values along a Cartesian axis, large radial momentum is implied, and the measurement matches the integral of Equation 4.6. We have measured the real, time-independent amplitudes of each constituent state using SSFI, and the relative phase information can be extracted

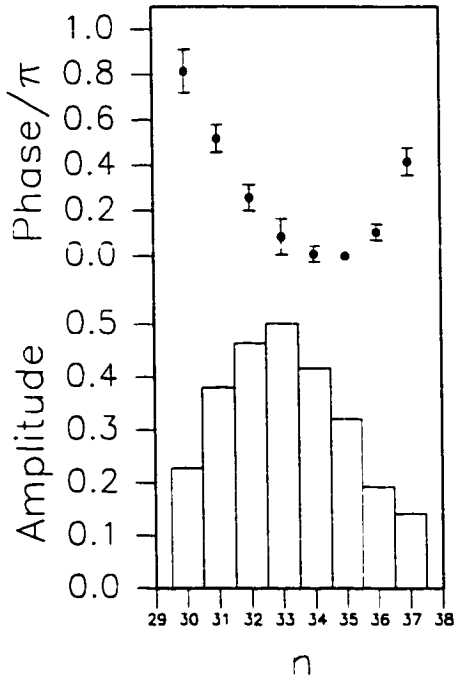

Figure 4.10: Measured amplitude and phase for a $4snd$ radial wavepacket in calcium. The real amplitudes were measured using SSFI, and the phases were obtained from the Fourier transform of time-dependent momentum-space probability distribution measurements.

by taking the discrete Fourier transform, $\mathcal{F}(\vec{p}, t)$, of a low ionization probability curve. Figure 4.12 shows $\mathcal{F}(\vec{p}, t)$ for a range of ionization levels. We restrict ourselves to low ionization probability curves because they correspond to large radial momentum. The transform consists of a series of peaks at the difference frequencies $\Delta E_{n_2,n_1}$. The phase of $\mathcal{F}(\vec{p}, t)$ evaluated at the center of each peak represents the phase difference, $\Delta\phi_{n_2,n_1}$ between eigenstates ψ_{n_2} and ψ_{n_1}. We determine the phase of each state, within a constant phase shift for all states, from the phase differences. The phase and amplitude of states comprising of the radial wavepacket are shown in Figure 4.10

The sign of the phase difference, ϕ_{n_2,n_1} (whether to take + or $-$ $\Delta\phi_{n_2,n_1}$) , between states varies with the sign of the product of the real wavefunctions, $\psi_{n_1}(\vec{p})\psi_{n_2}(\vec{p})$,

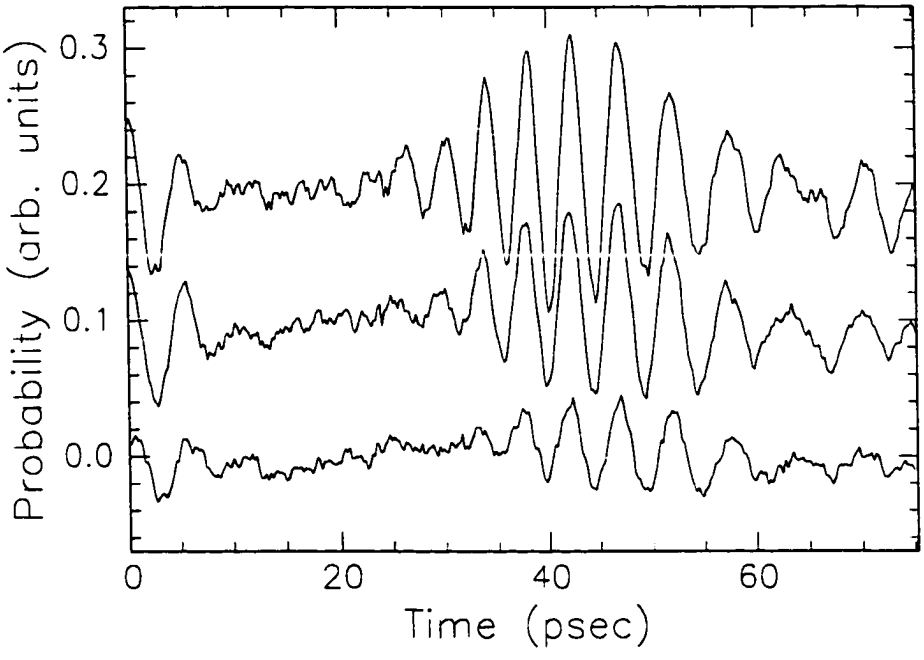

Figure 4.11: Measured relative ionization probability for three different HCP fields. The curves are vertically offset for clarity. Each curve oscillates about a base ionization level of 8, 20 and 35 percent respectively from bottom to top.

which is a known value for Rydberg eigenstates. For intermediate values of p_r, the product of the wavefunctions may oscillate rapidly, making it difficult to uniquely determine the phase difference sign. At its creation, the wavepacket is localized near the atomic core and has a high probability of having a large momentum component. The momentum-space wavefunction product for adjacent Rydberg eigenstates is positive for large $\vec{p}$. Therefore, by only considering low ionization probability (large momentum) curves, the phase difference is $+\Delta\phi_{n_2,n_1}$.

An interesting phenomenon is observed with the lowest ionization probability curves which are generated with low amplitude HCPs. Curves showing the time dependent ionization probability oscillations for the radial wavepacket for three different HCP amplitudes are shown in in Figure 4.11. The HCP field is large enough to ionize

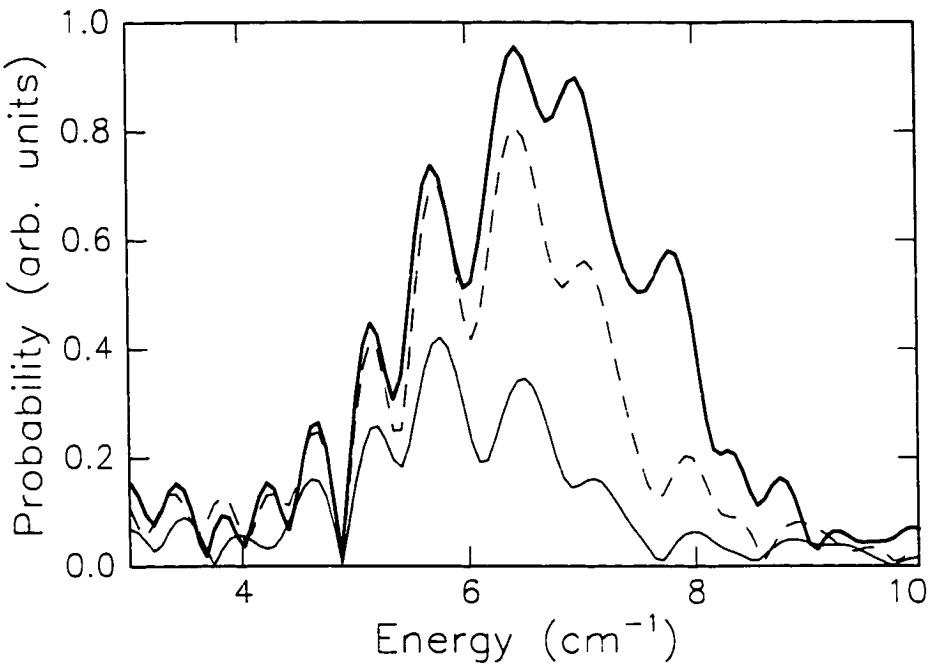

Figure 4.12: Discrete Fourier transform of the ionization probability curves shown in Figure 4.11. The thin solid line represents the lowest ionization level, the dashed line the next highest level and the bold solid line the highest ionization level. The peaks occur at the $4snd$ energy splittings for adjacent n-states. As the ionization probability increases, higher frequency components appear in the transform.

8, 20 and 35 percent of the wavepacket, respectfully, from bottom to top.

Clearly, as the HCP amplitude is increased, more oscillations appear earlier in time. Figure 4.12 shows the discrete Fourier transform of the curves shown in Figure 4.11. As the impulse of the HCP is increased, the size of the higher frequency peaks disproportionally increase. The higher frequency peaks correspond to the energy differences between lower n-states that are not as easily ionized by a low amplitude HCP. The HCP is selectively ionizing the high-n portion of the wavepacket. The lowest ionization probability curves only provide information about those states that are energetically high enough to be ionized by the HCP. To extract phase information regarding the low n-states of the wavepacket, slightly higher ionization probability

levels are needed. This brings a strong point to attention: the IMR method assumes there is a well defined energy of the wavepacket (electron), but the wavepacket has a range of energies. This discrepency is most noticeable in the low amplitude HCP regime. In this regard, a wavepacket with constituent eigenstates spread over a smaller energy range may be more appropriate for this type of measurement.

The phases shown in Figure 4.10 were obtained from 16 different ionization probability curves, taken along either the $\hat{x}$ or $\hat{z}$ directions. Fewer curves were used to find the phase of the extreme states in the wavepacket. The phases of the lower n-states were restricted to HCP fields that were strong enough to uniformly ionize those states but were not strong enough to compromise the large momentum value restriction. Error bars in Figure 4.10 represent the standard error of the mean of the measurement ensemble.

Using the measured complex amplitudes, the time-dependent probability distribution of the $4snd$ radial wavepacket is generated and shown in coordinate and momentum-space in Figure 4.13. The features in these plots match the features in Figure 4.5. Although we learned a great deal about the limitations on the IMR method, measurement of the complex amplitude of each contributing state in the wavepacket provides just as much information about the evolution of the wavepacket.

The ability to quantitatively assess the complex amplitudes of the constituent states in an electronic wavepacket, its quantum state, is not restricted to measurements of the probability distribution in momentum-space. The same information can be extracted from a measurement of the probability distribution for a Rydberg wavepacket near its inner or outer turning point using time-resolved isolated core excitation (TRICE) [22].

Note that we have used SSFI to measure the real eigenstate amplitudes. More

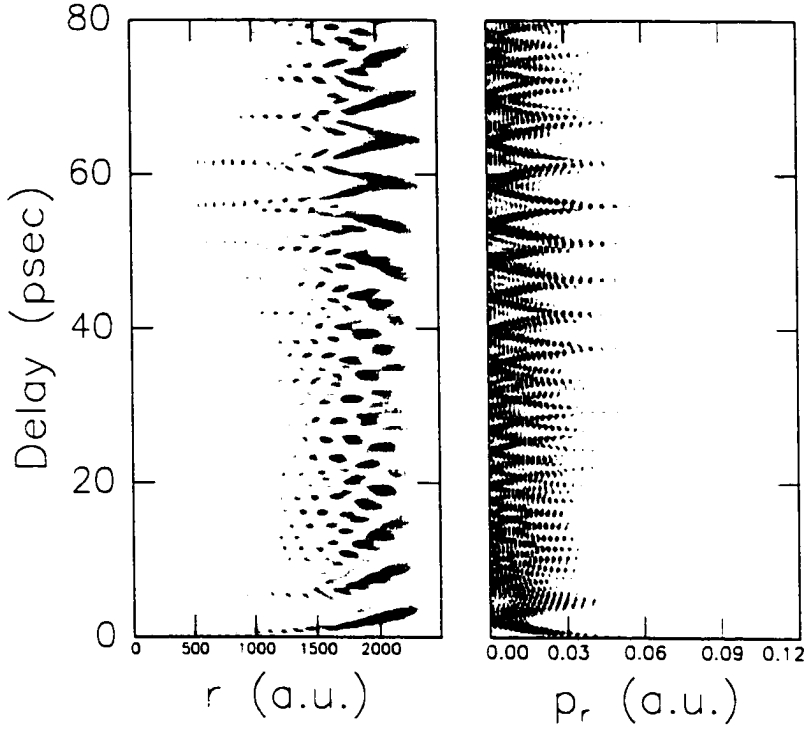

Figure 4.13: Evolution of the radial and momentum-space wavefunction as dictated by the measured values of amplitude and phase of the contributing states to the wavepacket.

complicated wavepackets that are superpositions of states with different n, ℓ and m, have states that are not as readily discernable with SSFI. In principle, the real eigenstate amplitudes, a_n can be determined from $\mathcal{F}(\vec{p}, t)$. The ratio of any two amplitudes, a_{n_1}/a_{n_2}, is directly proportional to $\mathcal{F}(\vec{p}, \Delta E_{n_1,n})/\mathcal{F}(\vec{p}, \Delta E_{n,n_2})$. The constant of proportionality depends on the eigenstate products, $\psi_{n_1}\psi_n$ and $\psi_n\psi_{n_2}$, which are known quantities. The discrete Fourier transforms are susceptible to noise. Also, the relative peak size varies significantly with different ionization probabilites, as observed in Figure 4.12. Therefore, a more reliable method such as SSFI is used.

The determination of the amplitude and phase of each constituent state in an electronic wavepacket has been achieved in another way. It was recently predicted [23] and demonstrated [24] that this information can be extracted from a wavepacket with a wavepacket cross-correlating measurement combined with the measurement of the real amplitudes of each state. This method involves the creation of two wavepackets, one is under study, and the other is a reference wavepacket with a known quantum state. The need for the excitation of two wavepackets can be technically challenging, especially for more complicated wavepackets. A complex reference wavepacket may not be in a well characterized quantum state, extending the difficulties of the cross-correlation technique. In some cases, the Fourier transform method used above is more straight forward in its ability to quantitatively measure the quantum state of an atomic system. However, this method is limited to wavepackets made up of states that have energy differences that can be distinguished in the Fourier transform. Different m and high ℓ states in zero field are indistinguishible with our current resolution. Similarly, the energy spacing between different Stark states (discussed in Chapter 5) is approximately equal in an n manifold, making it impossible to differentiate between Stark states in the discrete Fourier transform.

4.5 Conclusions

By studying radial wavepackets we have learned about the capabilities of monitoring electronic wavepacket dynamics with half-cycle pulses of THz radiation. The interaction of a HCP with a wavepacket is insightfully thought of classically, as a finite impulse delivered to an electron in a Keplerian orbit. This picture works well to a high degree of accuracy, but we must recognize when and how this approximation deteriorates.

When measuring the momentum-space probability distribution, the IMR method does not accurately determine the probability distribution of the wavepacket at times when the wavepacket is localized near the atomic core. The wavepacket is moving rapidly near the core, which breaks assumptions of the IMR method, that the impulse delivered by the HCP is truly impulsive, and the wavepacket is essentially motionless during its interaction with the pulse.

Extracting complex amplitudes of eigenstates in a radial wavepacket demonstrates that an enormous amount of information can be obtained with a simple measurement of its time-dependent ionization probability due to a HCP. However, for low amplitude HCPs, the probability only represents the contributing states with highest energy (*ie* the wavepacket does not uniformly respond to the HCP). The measurement is robust because a full determination of the momentum-space probability distribution is not necessary. The relative phases of constituent states of the wavepacket is fixed at $t = 0$ and is independent of $\vec{p}$.

We plan to take this knowledge and apply it to more complicated electronic systems in which the exact state distribution can be difficult to determine and theoretical analysis may be prohibitively difficult.

Bibliography

[1] L.D. Noordam and R.R. Jones, *J. Mod. Opt.* **44**, 2515 (1997).

[2] R.R. Jones and L.D. Noordam, *Advances in Atomic, Molecular and Optical Physics* **38**, 1 (1997).

[3] G. Alber, H. Ritsch and P. Zoller, *Phys. Rev. A* **34**, 1058 (1986).

[4] C. Raman, C.W.S. Conover, C.I. Sukenik and P.H. Bucksbaum, *Phys. Rev. Lett.* **76**, 2436 (1996).

[5] R.R. Jones, *Phys. Rev. Lett.* **76**, 3927 (1996).

[6] T.C. Weinacht, J. Ahn and P.H. Bucksbaum, *Phys. Rev. Lett.* **80**, 5508 (1998).

[7] G. Raithel, W.D. Phillips and S.L. Rolston, *Phys. Rev. Lett.* **81**, 3615 (1998). Robert Bluhm and V. Alan Kostelecký, *Phys. Rev. A* **50**, R4445 (1994). Robert Bluhm and V. Alan Kostelecký, *Phys. Rev. A* **51**, 4767 (1995). Xin Chen and John A Yeazell, *Phys. Rev. A* **57**, R2274 (1998). Jeffrey L. Krause, Kenneth J. Schafer, M. Ben-Nun and Kent R. Wilson, *Phys. Rev. Lett.* **79**, 4978 (1997). Robert Bluhm and V. Alan Kostelecký, *Phys. Lett. A* **200**, 308 (1995). A. ten Wolde, L.D. Noordam, A. Lagendijk and H.B. van Linden vanden Heuvell, *Phys. Rev. Lett.* **61**, 2099 (1988).

[8] L.D. Noordam, D.I. Duncan and T.F. Gallagher, *Phys. Rev. A* **45**, 4374 (1992). B.Broers, J.F. Cristian, J.H. Hoogenraad, W.J. van der Zande, H.B. van Linden van der Heuvell and L.D. Noordam, *Phys. Rev. Lett.* **71**, 344 (1993).

[9] D. You *et al.*, *Opt. Lett.* **18**, 290 (1993).

[10] R.R. Jones, D. You and P.H. Bucksbaum, *Phys. Rev. Lett.* **70**, 1236 (1993).

[11] Thomas F. Gallagher, *Rydberg Atoms*, Cambridge University Press (1994).

[12] N.E. Tielking, T.J. Bensky and R.R. Jones, *Phys. Rev. A* **51**, 3370 (1995).

[13] G.M. Lankhuijzen and L.D. Noordam, *Advances in Atomic, Molecular and Optical Physics* **37**, 121 (1997).

[14] R.R. Jones and P.H. Bucksbaum, *Comm. on At. Mol. Opt. Phys* **28**, L457 (1995).

[15] F. Robicheaux, *Phys. Rev. A* **56**, R3358 (1998).

[16] P. Kristensen, G.M. Lankhuijzen and L.D. Noordam, *J. Phys. B: At. Mol. Opt. Phys.* **30**, 1481 (1997). S. Yoshida *et. al.*, *Phys. Rev. A* **58**, 2229 (1998). R.R. Jones, N.E. Tielking, D. You, C. Raman and P.H. Bucksbaum, *Phys. Rev. A* **51**, R2687 (1995).

[17] R.B. Vrijen, G.M. Lankhuijzen and L.D. Noordam, *Phys. Rev. Lett.* **79**, 617 (1997). I. Bersons and A. Kulsh, *Phys. Rev. A* **59**, 1399 (1999).

[18] A spline fit through each ionization probability versus HCP field curve is necessary to prevent slight fluctuations due to noise from dominating the curve's derivative.

[19] B. Podolsky and L. Pauling, *Phys. Rev* **34** 109 (1929).

[20] The quantum calculations shown in Figure 4.6 and Figure 4.7 were performed by R.R. Jones.

[21] The ionization threshold calculations for a classical ensemble of hydrogenic electrons were performed by T.J. Bensky. Another approach to classically calculating probability distributions in Rydberg Atoms is presented in Inés Samengo, *Phys. Rev. A* **58**, 2767 (1998).

[22] R.R. Jones *Phys. Rev. A* **57**, 446 (1998).

[23] X. Chen and J.A Yeazell, *Phys. Rev. A* **56**, 2316 (1997).

[24] T.C. Weinacht, J. Ahn and P.H. Bucksbaum, *Phys. Rev. Lett.* **80**, 5508 (1998).

Chapter 5

Stark Wavepacket Evolution

5.1 Introduction

The work described in Chapter 4 demonstrated our ability to monitor the dynamics of radial wavepackets using HCPs of THz radiation. We learned that the impulsive momentum retrieval (IMR) method accurately determines the probability distribution of the wavepacket throughout a majority of its trajectory, failing only when the wavepacket is localized near the atomic core.

Direct observation of electronic motion of an electronic wavepacket can be used to interpret the physics behind the motion, without the need to depend on theoretical simulations. Controlling wavepacket motion in complex systems, in which full quantum mechanical calculations are not readily available, is limited by the ability to understand the system soley from experimental measurements.

With this in mind, we probe the evolution of Stark wavepackets. The experiment presented here is similar to the one described in Chapter 4. Wavepackets are excited in calcium atoms with a short laser pulse and the dynamics are monitored with HCP probes. In contrast to the previous experiment, the wavepackets are excited in the presence of a strong electric field. The electric field breaks the spherical symmetry of

the Coulomb potential, meaning orbital angular momentum is no longer a conserved quantity of the wavepacket. Using the IMR method, we are able to directly monitor both radial and angular dynamics, as well as a large-amplitude linear oscillation of the electronic dipole moment. The measurement of the full time-dependent momentum-space probability distribution, enables both interpretation of the intricate dynamics of coupled radial and angular precessions and characterization of the wavepacket throughout its orbit. The Stark effect on Rydberg atoms has been studied extensively in the last decade, including wavepacket recurrence measurements [1] and calculations [2]. Other studies include probing wavepackets with far-infrared radiation [3], time-gated photionization spectroscopy using an atomic streak camera [4], and calculations of electronic dynamics in electric fields [5]. Work focused on monitoring the dynamics of Stark wavepackets with HCPs has also been performed [6, 7, 8]. Yet we are the first to recover the full time-dependent probability distribution of a Stark wavepacket.

Strong oscillations in the electonic dipole moment imply the Stark wavepacket emits bursts of THz radiation. This Chapter presents a quantum mechanical simulation that calculates the time-dependent dipole moment for an arbitrary Stark wavepacket. By varying the constituent state population of the wavepacket and the applied static field strength, we search for the optimal conditions for strong THz pulse generation. The idea of a Stark wavepacket as a tunable source of short pulsed THz radiation is exciting due to the low number of such devices currently available.

5.2 The Stark Effect

The perturbation of energy states in an atom due to an externally applied electric field is traditionally referred to as the Stark effect, and a discussion of how to quantify this effect is presented in this section. The phenomenom is named after Johannes

Stark, who published the first paper on the subject on December 4, 1913 in *Nature*. Apparently, a fellow by the name of Antonino LoSurdo was scooped by Stark. LoSurdo had observed energy level splitting in the summer of 1913 [9] but did not get publish an article until December 21, 1913, shortly after Stark. LoSurdo, however, had presented the first photographs of split Balmer series lines in hydrogen as a result of an applied electric field in the Fall of 1913. LoSurdo has lost out to Stark regarding the accepted jargon, but it is necessary to mention his contribution to the study of the effect of applied electric fields on atoms. If Stark had waited a couple of weeks to publish his article, this Chapter may well have been called "LoSurdo Wavepacket Evolution." Eventually, LoSurdo founded the Italian National Institute of Geophysics and left the atomic physics community, so he probably does not mind.

The presence of a static electric field ($\vec{F} = F\hat{z}$) breaks the spherical symmetry of the Coulomb potential in an atom, so angular momentum is no longer a conserved quantity (ℓ is no longer a good quantum number). Time independent perturbation theory can be used to study the effects the electric field has on the eigenstates of an atom [10, 11]. We begin by considering the linear Stark effect in hydrogen, which provides a good approximation of the effect external fields have on the energy levels in calcium atoms.

The symmetry of the atom best matches parabolic coordinates, ξ, η, and ϕ, where $\xi = r + z$, $\eta = r - z$ and $\phi = tan^{-1}(\frac{y}{x})$, and the Stark effect can be calculated in closed form using this coordinate system. Alternatively, the eigenvalues of the system can be extracted from a perturbation matrix formed with eigenfunctions in polar coordinates. This is done for both hydrogen and (out of necessity) calcium later in the Chapter.

ξ and η form parabolic surfaces of revolution. The perturbation potential ex-

pressed in these coordinates is $Fz = \frac{1}{2}F(\xi - \eta)$. The Laplacian in the Schrödinger equation, $(\frac{1}{2}\nabla^2 + E + Z/r - Fz)\psi = 0$, must be converted to parabolic coordinates, giving the following Hamiltonian,

$$\frac{\partial}{\partial\xi}(\xi\frac{\partial\psi}{\partial\xi}) + \frac{\partial}{\partial\eta}(\eta\frac{\partial\psi}{\partial\eta}) + (\frac{1}{4\xi} + \frac{1}{4\eta})\frac{\partial^2\psi}{\partial\phi^2} + [\frac{1}{2}E(\xi+\eta) + Z - \frac{1}{4}F(\xi^2 - \eta^2)]\psi = 0. \quad (5.1)$$

This is separable in u_1 and u_2, giving the eigenfunctions $\psi(\xi, \eta, \phi) = u_1(\xi)u_2(\eta)e^{\pm im\phi}$, where $m = 0, 1, 2, \ldots$ (m is the familiar azimuthal or magnetic quantum number) and the functions u_1 and u_2 are solutions to the following differential equations:

$$\frac{d}{d\xi}(\xi\frac{du_1}{d\xi}) + (\frac{1}{2}E\xi + Z_1 - \frac{m^2}{4\xi})u_1 = 0. \quad (5.2)$$

and,

$$\frac{d}{d\eta}(\eta\frac{du_2}{d\eta}) + (\frac{1}{2}E\eta + Z_2 - \frac{m^2}{4\eta})u_2 = 0. \quad (5.3)$$

Z_1 and Z_2 are separation constants where $Z = Z_1 + Z_2$ is the nuclear charge seen by the electron and m is the quantum number corresponding to the projection of angular momentum on the z axis.

We want to find a functional form of u_1 and u_2. Following the standard method of solving the differential equations above, as would be done for the radial equation for hydrogen in spherical coordinates, we get the following boundary conditions for $u_1(\xi)$ and $u_2(\eta)$, namely $u_1(\xi) \sim \xi^{\frac{1}{2}m}$, $u_2(\eta) \sim \eta^{\frac{1}{2}m}$ (for $m > 0$) as $\xi, \eta \to 0$ and $u_1(\xi) \sim e^{-\frac{1}{2}\xi\epsilon}$ and $u_2(\eta) \sim e^{-\frac{1}{2}\eta\epsilon}$ as $\xi, \eta \to \infty$ for $\epsilon \equiv \sqrt{-2E}$. From this, we look for polynomial solutions $f_1(\xi)$ and $f_2(\eta)$ that satisfy

$$u_1(\xi) = \xi^{\frac{1}{2}m}e^{-\frac{1}{2}\xi\epsilon}f_1(\xi), \quad (5.4)$$

and

$$u_1(\eta) = \eta^{\frac{1}{2}m}e^{-\frac{1}{2}\eta\epsilon}f_2(\eta). \quad (5.5)$$

By changing coordinates to $x = \epsilon\xi$ and $y = \epsilon\eta$, we get

$$x\frac{d^2f_1}{dx^2} + (m+1-x)\frac{df_1}{dx} + (\frac{z_1}{\epsilon} - \frac{m+1}{2})f_1 = 0. \tag{5.6}$$

and

$$x\frac{d^2f_2}{dy^2} + (m+1-y)\frac{df_2}{dy} + (\frac{z_2}{\epsilon} - \frac{m+1}{2})f_2 = 0. \tag{5.7}$$

The solutions to these equations are associated Laguerre polynomials, $f_1 = L^m_{n_1+m}(x)$ and $f_2 = L^m_{n_2+m}(y)$. For f_1 and f_2 to remain finite at large values of ξ and η, n_1 and n_2 must be non-negative integers. This gives $n_1 = \frac{Z_1}{\epsilon} - 1/2(m+1)$ and $n_2 = \frac{Z_2}{\epsilon} - 1/2(m+1)$, $\epsilon = \sqrt{-2E}$. So, $n_1 + n_2 = \frac{(Z_1+Z_2)}{\epsilon} - m - 1 = n - m - 1$, or $\frac{Z}{\epsilon} = n_1 + n_2 + m + 1$. ($0 \le m \le n-1$ and $0 \le n_1, n_2 \le n-1$) where n_1 and n_2 are known as the parabolic quantum numbers. Remember, in zero external field the energy of each parabolic state is $E = \frac{-\epsilon^2}{2} = -\frac{Z^2}{2}\frac{1}{(n_1+n_2+m+1)^2} = \frac{Z^2}{2n^2}$, and $n = n_1 + n_2 + m + 1$. Therefore, the parabolic eigenfunctions and the angular momentum eigenfunctions span the same space, and they are both complete and orthogonal: $|n_1 n_2 m> = |nkm> = \sum_\ell a_{\ell,k} \mid n\ell m>$, where $k = n_1 - n_2$ is the projection of the electric dipole along the z axis and $a_{\ell,k} =< n\ell m \mid nkm >$ are Clebsch-Gordan coefficients. The energy of Stark state depends not only on the principle quantum number, n, but on k. The $a_{\ell,k}$ coefficients are evalutated with

$$< n\ell m \mid nkm >= (-1)^{(1-n+m+k)/2+\ell} \times \sqrt{2\ell+1} \begin{pmatrix} \frac{n-1}{2} & \frac{n-1}{2} & \ell \\ \frac{m+k}{2} & \frac{m-k}{2} & -m \end{pmatrix}, \tag{5.8}$$

where the last term is a Wigner 3J symbol [12].

Now that the necessary equations have been defined for hydrogen in zero field, we must now consider the external electric field potential, $V_{ext} = Fz = \frac{1}{2}F(\xi - \eta)$, in the Hamiltonian. The Schrödinger equation remains separable with the adjusted

potential, and we arrive at the following differential equations.

$$\frac{d}{d\xi}(\xi\frac{du_1}{d\xi}) + (\frac{1}{2}E\xi + Z_1 - \frac{m^2}{4\xi} - \frac{1}{4}F\xi^2)u_1 = 0. \tag{5.9}$$

and,

$$\frac{d}{d\eta}(\eta\frac{du_2}{d\eta}) + (\frac{1}{2}E\eta + Z_2 - \frac{m^2}{4\eta} - \frac{1}{4}F\eta^2)u_2 = 0. \tag{5.10}$$

To find the perturbation due to the additional potential term, $V_{pert} = V_{ext} = F\vec{z} = Fr\cos(\theta)$, we find corrections to the separation constants $Z_1$and Z_2 in terms of $\epsilon = \sqrt{-2E}$. These corrections are found with,

$$Z_1^{(1)} = Z_1^{(0)} + \frac{1}{4}F < u_1^{(0)} \mid \xi^2 \mid u_1^{(0)} >= \epsilon(n_1 + \frac{m+1}{2}) + \frac{1}{4}\frac{F}{\epsilon^2}\left[6n_1^2 + 6n_1m + m^2 + 6n_1 + 3m + 2\right],$$

and

$$Z_2^{(1)} = Z_2^{(0)} + \frac{1}{4}F < u_2^{(0)} \mid \eta^2 \mid u_2^{(0)} >= \epsilon(n_2 + \frac{m+1}{2}) + \frac{1}{4}\frac{F}{\epsilon^2}\left[6n_2^2 + 6n_2m + m^2 + 6n_2 + 3m + 2\right].$$

We realize $Z = Z_1^{(1)} + Z_2^{(1)} = \epsilon n + \frac{3}{2}\frac{F}{\epsilon^2}(n_1 - n_2)n$. So, by solving for ϵ and using $\epsilon \equiv \sqrt{-2E}$, we find an expression for the energy.

$$E^{(1)} = -\frac{Z^2}{2n^2} + \frac{3}{2}\frac{Fn}{Z}(n_1 - n_2). \tag{5.11}$$

The change in energy of a given Stark state, k, is $\Delta E = \frac{3Fnk}{2}$ and is linear in F. We set $Z = 1$ for a valence electron. This is the first order correction to the hydrogenic energy levels and is valid as long as $F^2n^6 \ll 1$ cm^{-1}, which holds true for this experiment.

A plot of the one-dimensional combined Coulomb and static field ($F = 180$ V/cm) potential is shown in the bold curve of Figure 5.1. The thin curve represents the Coulomb potential without the external field. The potential on the $+\hat{z}$ side of the curve is called the "uphill" side and the $-\hat{z}$ side is called the "downhill" side, reflecting the general slope of the potential.

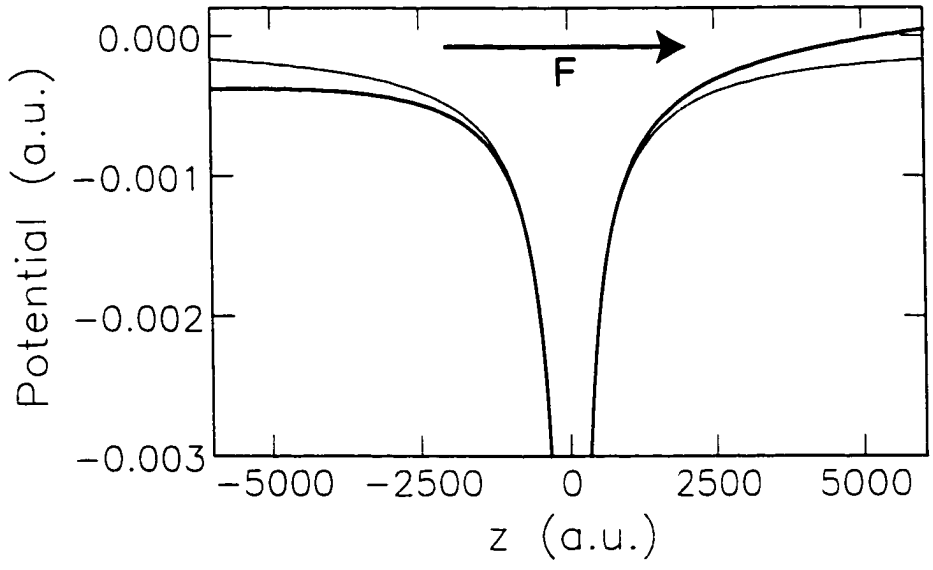

Figure 5.1: A one-dimensional plot of the adjusted Coulomb potential due to an applied static field ($F = 180$ V/cm) along $\hat{z}$ is shown with the bold curve. The thin curve plots the Coulomb potential with no external field. The combined potential moves "uphill" for $z > 0$ and "downhill" for $z < 0$.

The energy of individual Stark states similarly changes either uphill or downhill. The uphill (downhill) states are also known as blue (red) states because of the energy increase (decrease). The maximum energy change between the reddest state and the bluest state in a single n-manifold is given by $\Delta E_{max} = 3n^2F/Z$, and the spacing between adjacent Stark states is given by $\Delta E = 3nF/Z$.

A Stark map for hydrogen is shown in Figure 5.2. Energy level degeneracy is lifted for the different angular momentum states, and the energy of each Stark state scales linearly with the field strength. States from different manifolds cross at field where the reddest state of one manifold intersects with the bluest state of the manifold just below. This crossing occurs at a field strength of $F_c = \frac{Z^3}{3n^5}$, for $n \gg 1$.

A wavepacket evolves on a time scale defined by the energy spacing between accessible eigenstates of the wavepacket. The calculations described above demonstrates that adjacent eigenstates are separated in energy by $\Delta E = 3nF$, meaning the period for angular precession is $\tau_{Stark} = 2\pi/3nF$. Therefore, a wavepacket with initially localized angular momentum in the presence of a static electric field experiences an angular momentum precession from its original value to the available angular levels and back over a Stark period. Although the calculation discussed above was made for hydrogen we use this time scale to approximate the angular evolution in a Stark wavepacket in calcium. In calcium, the valence electron excited into a wavepacket does not encounter a hydrogenic coulomb potential when it approaches the nucleus due to the finite size of the ionic core. This effect shifts the energy of the low ($\ell = 0, 1, 2$) angular momentum states in calcium but leaves the remaining angular momentum states insignificantly affected. In the presence of a static electric field, the energy spacing between eigenstates in calcium are not significantly different than those in hydrogen, and the electron spends a majority of its time in states with high an-

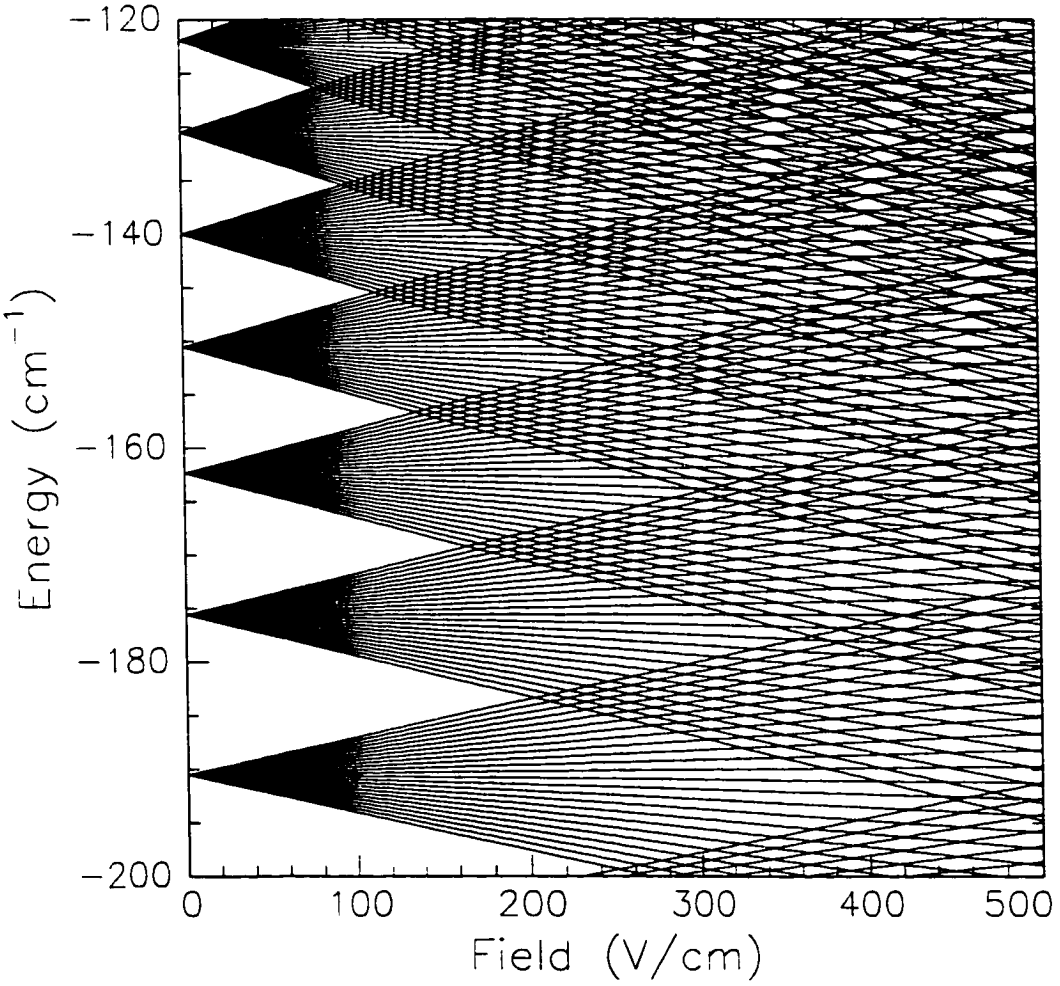

Figure 5.2: Stark map for hydrogen for $24 \leq n \leq 30$ generated using the linear Stark effect approximation. In the presence of an electric field, the k-state energy levels are not degenerate. Notice the manifolds cross at $F_c \approx 1/3n^5$.

gular momentum character. Therefore, we use this approximation to estimate the evolutionary timescale of a Stark wavepacket. Quantum mechanical calculations indicate the finite ionic core *does* noticably affect the long-term dynamics of a Stark wavepacket, and this is discussed later in the Chapter.

5.3 Experiment

The experimental setup is similar to the radial wavepacket experiment. The excitation scheme for the sample of calcium atoms is shown in Figure 5.3. Ground state $4s4s^1S_0$ atoms are excited to a $4s4p^1P_0$ intermediate state with a 5 nsec, 423 nm dye laser pulse. A 1.5 psec, 392 nm laser pulse populates the $4snd^1D_0$ wavepacket, with $26 \leq n \leq 30$. This pulse generated by frequency doubling a portion of the 120 fsec, 786 nm laser pulse with a 2 cm BBO crystal. Phase matching in the crystal extends the pulse to 1.5 psec, limiting the bandwidth so that ~80% of the wavepacket population is in the n=27, 28 and 29 states (the laser bandwidth was much larger in the radial wavepacket experiment). The calcium atoms are supplied in an effusive beam directed between two electric field plates. The 10 cm × 10 cm plates are separated by 1.5 cm, and a +275 V static field is applied to the bottom field plate, creating a 180 V/cm electric field throughout the atom/laser interaction region. All laser beams are polarized along the static field axis, so only $m_\ell = 0$ states are excited. As seen on the Stark map in Figure 5.2, assuming Stark states in calcium are similar to those in hydrogen, we work in a region where the adjacent manifolds begin to cross. The characteristic time scale of angular momentum precession is the Stark period, $T_{Stark} = \frac{2\pi}{3NF} = 54$ psec, where N is the mean principle quantum number in the wavepacket, and F is the applied static field strength. At this moderately strong electric field strength, the potential experienced by the wavepacket is dominated

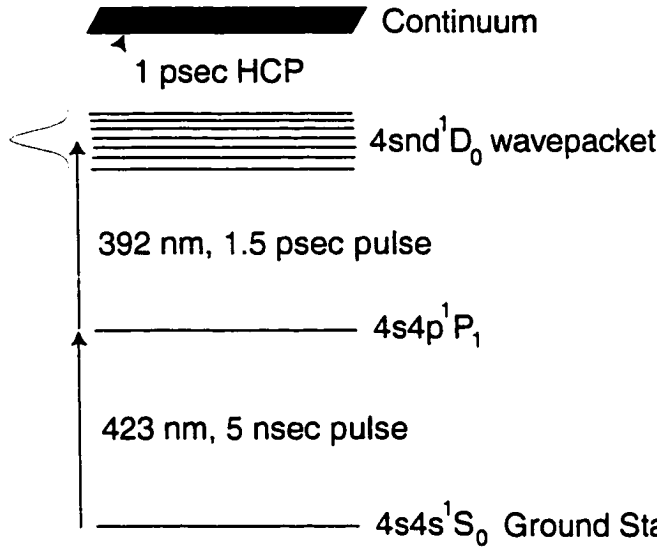

Figure 5.3: Excitation scheme for creating and detecting Stark wavepackets in calcium. The 392 nm, 1.5 psec pulse has enough bandwidth to excite a wavepacket with about 5 manifolds included.

by the Coulomb field and the external field at its inner and outer turning points, respectively.

We probe the wavepacket with half-cycle pulses, and the interaction of a HCP with an electronic wavepacket is discussed in Chapter 4. Clearly, the 1 psec HCP duration is significantly shorter than both the Kepler ($\tau_{Kepler} = 2\pi.N^3 = 3$ psec) and Stark ($\tau_{Stark} = 2\pi/3NF = 54$ psec) periods of the wavepacket [13]. Wavepacket ionization probability as a function of HCP amplitude and delay is recorded along the $\pm\hat{x}$ and $\pm\hat{z}$ directions in the same manner as described in Chapter 4. Again, the data is resorted into ionization probability as a function of HCP amplitude over a range of time delays, from which the time-dependent momentum-space probability distribution is determined along orthogonal axes.

Previously, we struggled to get HCP fields strong enough to saturate the ionization probability for a radial wavepacket with a mean principle quantum number equal

$N = 33$ along the $\hat{x}$ axis. For this experiment we retrieve the full distribution along both $\hat{x}$ and $\hat{z}$ axes for a wavepacket centered on $N = 28$. Two differences between experiments make this possible. First, the static electric field reduces the energy transfer required for ionization. More importantly, we recognized a symmetry in the HCP ionization process. Thinking classically, a bound electron moving in the $+\hat{x}$ direction can be ionized by a weak HCP polarized along $+\hat{x}$, whereas ionization requires a very strong HCP polarized along $-\hat{x}$. A cartoon illustrating this effect is shown in Figure 5.4. The momentum-space probability distribution along the $+\hat{x}$ axis can be determined using the IMR method by either relatively weak HCPs polarized along the $+\hat{x}$ axis or very strong HCPs polarized along the $-\hat{x}$ axis, and vice versa for the distribution along $-\hat{x}$. Therefore, the probability distribution along the entire axis is produced by combining the measurement of the distributions along the negative (using negatively polarized HCPs) and positive (using positively polarized HCPs) portions of the distribution. The same reasoning is used along the $\hat{z}$ axis. Near $p_{x,z} = 0$, the portions of the distributions that overlap are averaged together.

We combine opposite sides of the probability distributions along each axis to obtain the full distribution even though in Chapter 4 we have shown the IMR method artificially generates asymmetric distributions in the wavepacket. The asymmetry resulted when the low-ℓ wavepacket was localized near the atomic core. The Stark wavepacket has low angular momentum for only a small fraction of its trajectory and spends a vast majority of the time far from the core, where the IMR method reliably determines the probability distribution.

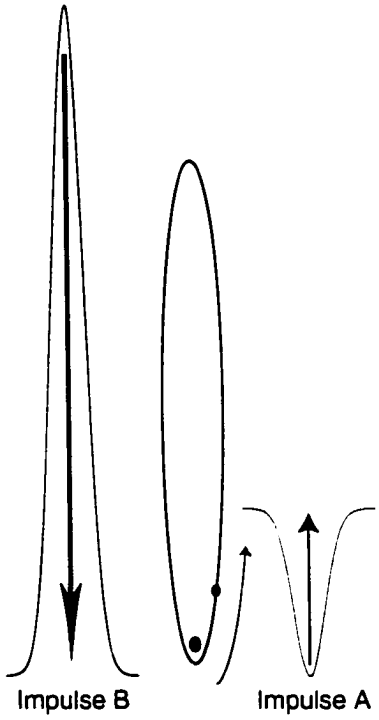

Figure 5.4: Schematic diagram showing the (approximate) relative HCP amplitude needed to ionize an electron moving quickly away from the atomic core for oppositely polarized HCPs. To ionize the electron, $|B| > 4|A|$.

5.4 Results

Density plots of the measured time-dependent momentum distributions along the $\hat{z}$ ($\mathcal{P}_z$) and $\hat{x}$ ($\mathcal{P}_x$) directions are shown in Figure 5.5A and 5.5B, respectively. The distributions are attained from the scaled derivative of the ionization vs HCP amplitude curve at each time delay, as discussed earlier. Two data runs for each HCP polarization are averaged together to produce these plots. Symmetry of the atomic system dictates that $\mathcal{P}_x = \mathcal{P}_y$, so the full distribution has been measured.

The 1.5 psec excitation pulse is short enough to ensure the wavepacket initially is localized in both its angular and radial distributions. For a short time after its excitation the wavepacket has low angular momentum and resembles a radial wavepacket. The momentum axis is calibrated by scaling the bias voltage on the GaAs switch to the calculated impulse required to produce 50% ionization of the d-wave packet at $t = 0$. Setting the total energy of the wavepacket to zero, $E = 0 = -1/2N^2 + (P_o + A)^2/2 - Fz$, gives $A = \sqrt{1/N^2 - 2Fz}$ when $P_o = 0$. At $t = 0$, the wavepacket is close to the atomic core, so z is small, and the calibration of A is nearly identical to results in Chapter 4, namely $A \approx 1/N$.

Sufficient HCP field amplitude transmits through the attenuating GaAs wafer along the $\hat{x}$ axis to saturate the wavepacket ionization probability at unity. An absolute determination of the 50% ionization probability signal level allows calibration of the impulse delivered by the HCP along both the $\hat{x}$ and $\hat{z}$ axes.

The temporal evolution of $\mathcal{P}_x$ and $\mathcal{P}_z$ are noticeably different. $\mathcal{P}_x$ is symmetric about $p_x = 0$ and broadens by $\sim 50\%$ near $t = 27$ psec. At $t = 0$, as well as $t = 54$ psec, a symmetric breathing occurs for a couple of cycles at the Kepler period. This motion is produced by a localized wavepacket moving away from and back towards

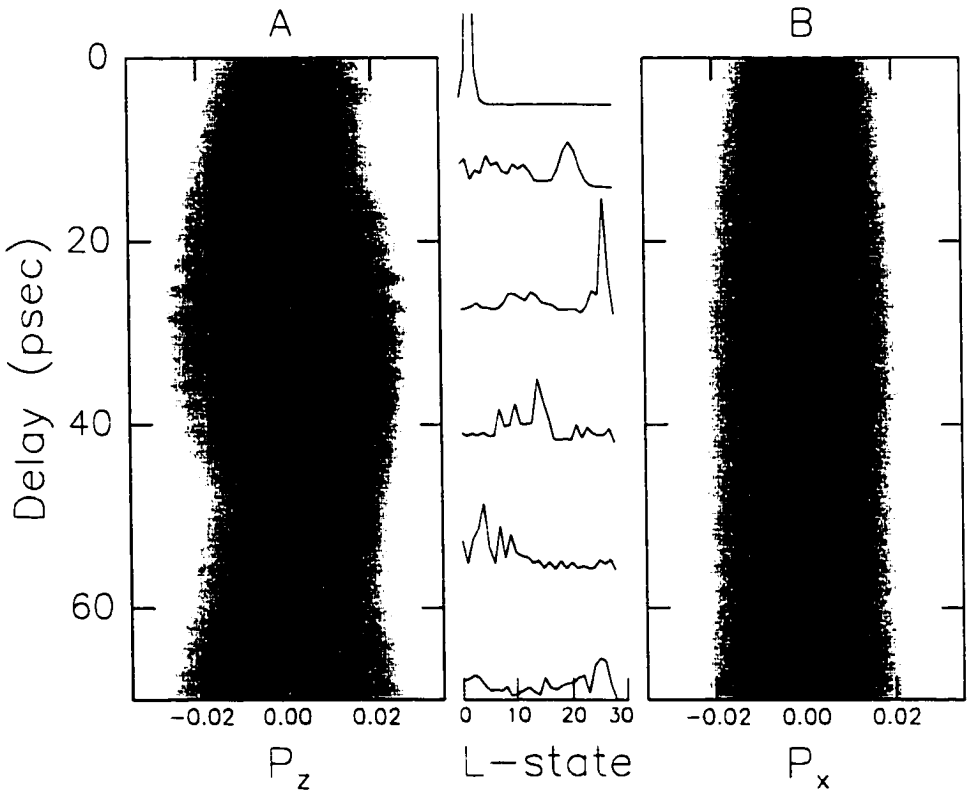

Figure 5.5: Density plots of the measured time-dependent momentum distribution of the Stark wavepacket in the A) z and the B) x directions. Higher probability is represented by darker coloring. The central insert show the calculated ℓ-state distribution at different times during the evolution.

the atomic core and resembles the distribution evolution of a radial wavepacket. The distribution is narrowest when the localized wavepacket is near its outer turning point and basically stopped. The overall breathing of the $\mathcal{P}_x$ at the Stark period reflects the angular momentum precession of the wavepacket.

The inset between Figures 5.5 A and B shows the expected angular momentum state distribution at different times throughout the wavepacket's evolution. At half the Stark period the distribution is heavily weighted towards high angular momentum states. Electrons in high ℓ-states have (nearly) circular orbits and spend less time at the outer turning point relative to the highly elliptical low ℓ-states. Therefore, the electrons have a lower probability of having zero momentum along the $\hat{x}$ axis. Calculations of the momentum-space probability distributions for an ensemble of classical electrons with well defined energy in different angular momentum states are shown in Figure 5.6. The distribution in the x-y plane consistently peaks at zero and broadens for high angular states.

$\mathcal{P}_z$ has a much more structured evolution but behaves similarly to $\mathcal{P}_x$ near $t = 0$ and $t = \tau_{Stark} = 54$ psec, when the wavepacket has low angular momentum. The oscillations at the Kepler frequency are due to the radial oscillations of the wavepacket and occur with identical phase and frequency as the oscillations seen in $\mathcal{P}_x$. At early times, $\mathcal{P}_z$ has a single probability maximum. Over the first Stark period the structure separates into two distinct peaks before collapsing back into a single peak near τ_{Stark}. This, again, reflects the precession of angular momentum from low to high back to low ℓ-states. Considering an ensemble of classical electrons in $m_\ell = 0$ states, all trajectories lie in a plane containing the z axis. $\mathcal{P}_z$ provides an end-on view of an ensemble of planar orbits. Low angular momentum states have highly elliptical orbits arranged over many different semi-major axis orientations relative to $\hat{z}$, resulting in a

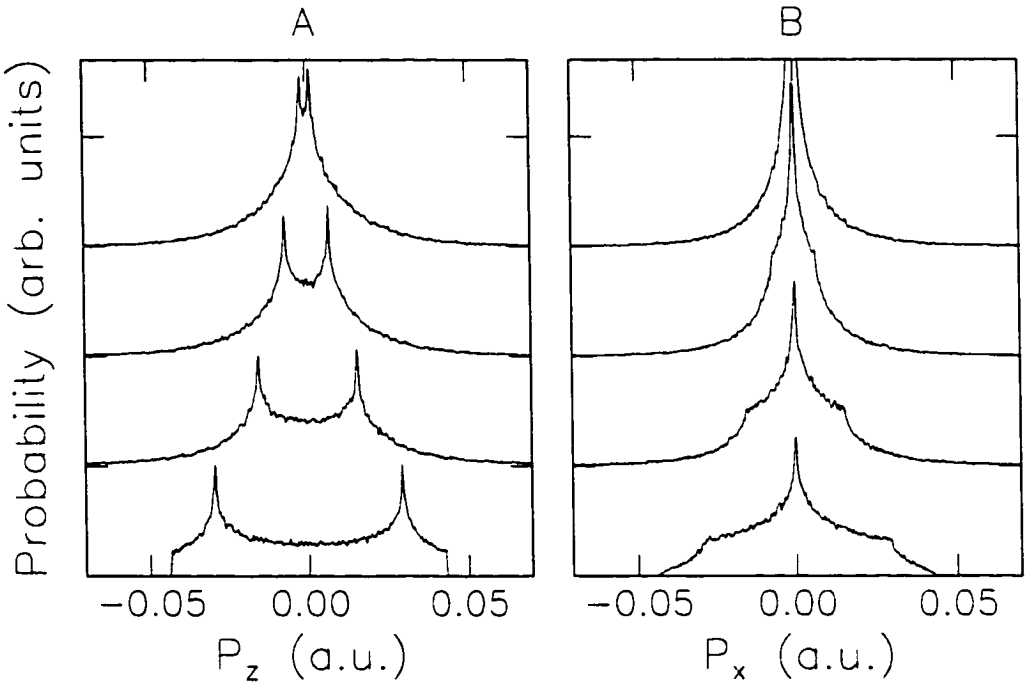

Figure 5.6: Calculated momentum distribution along $\hat{z}$ and $\hat{x}$ for an ensemble of classical hydrogenic electrons in the $n = 28$, $m_\ell = 0$ states with $\ell = 2, 10, 20,$ and 27 from top to bottom [14].

broadening of $\mathcal{P}_z$ that is centered on $p_z = 0$. For circular orbits with high-ℓ, there is only one orientation of the orbit with respect to the z-axis. Therefore, the probability for an electron travelling in the $+\hat{z}$ or $-\hat{z}$ directions increases, and the double-peaked distribution is produced. In both $\mathcal{P}_x$ and $\mathcal{P}_z$ we directly observe the full precession of the electronic orbital angular momentum.

The bi-modal feature in $\mathcal{P}_z$ is weighted towards negative values of p_z during the first half of the Stark period. Conversely, the two peaks are weighted towards positive values during the second half of the Stark period. Again, classical arguments can explain this phenomenon. At the time of the launch, the wavepacket is described as an ensemble of classical electrons leaving the atomic core in a shell of probability. The external field applies a non-central "downhill" force on the electrons, providing the torques responsible for angular momentum precession. The electron motion is restricted to a plane so the angular impulse is either parallel or anti-parallel to the electron's net orbital angular momentum. The electrons leave the core with low angular momentum, but the applied field ensures that they have a nonzero angular momentum component along $-\hat{z}$ by the time they reach their respective outer turning points. The fact that $\mathcal{P}_z$ is weighted towards negative values of p_z for $0 \leq t \leq \tau_{Stark}/2$ implies the charge distribution has a common circulation pattern, moving slowly downhill at the outer turning point and moving very rapidly uphill near the nucleus. Because the wavepacket spends most of the time near the outer turning point, its momentum there is most prominent in $\mathcal{P}_z$. For $\tau_{Stark}/2 \leq t \leq \tau_{Stark}$, the angular momentum of the wavepacket is decreasing in time, indicating the electron is travelling uphill near its outer turning point. As a result, the peak at $p_z > 0$ dominates the probability distribution during these times. A simple cartoon in Figure 5.7 highlights the effects discussed above.

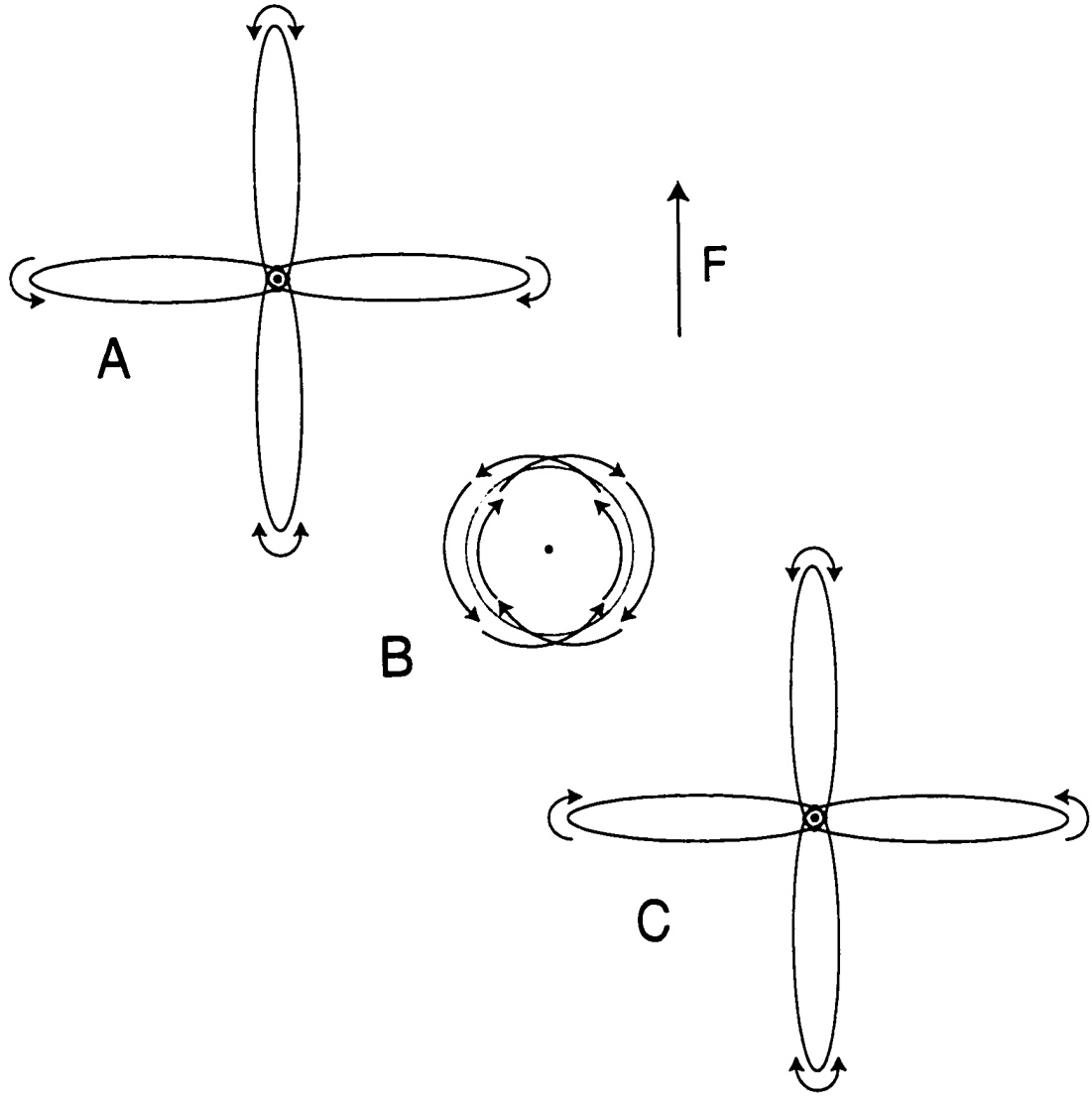

Figure 5.7: Cartoon showing high-probability motion in the electron orbits of a Stark wavepacket at different times in its evolution. The external electric field, F, induces (A) $0 < t < T_{Stark}/2$ relatively uniform motion 'downhill' near the outer turning point, (B) $t \approx T_{Stark}/2$ cycling of charge in circular orbits is in phase, creating an oscillation in $< z >$, and (C) $T_{Stark}/2 < t < T_{Stark}$ as angular momentum decreases. "uphill" motion at its outer turning point, where the wavepacket spends most of its time. The probability distribution is weighted towards positive values at this time.

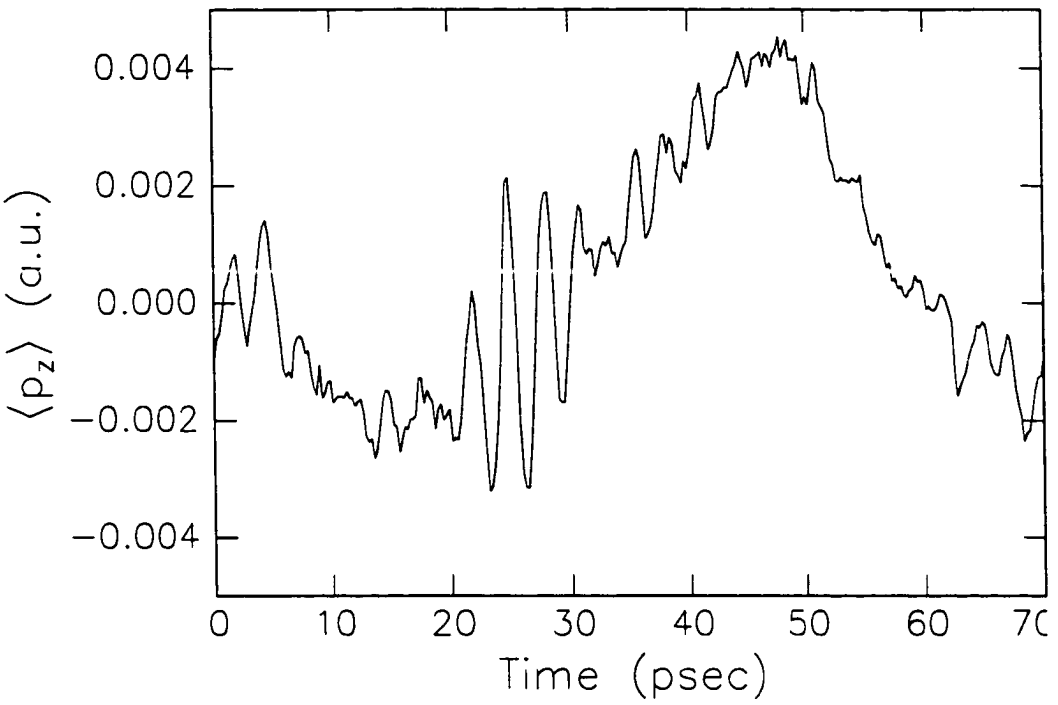

Figure 5.8: Measured time dependence of $\langle p_z(t) \rangle$.

At times near $T_{Stark}/2$ the distribution takes on its most interesting features. The wavpepacket's angular momentum is at a maximum, and the momentum distribution is oscillating back and forth at the Kepler frequency. Following the reasoning above, the electron distribution is circulating, or churning, uniformly throughout the wavepackets evolution. During the first half of the Stark period, the distribution is moving downhill at its outer turning point, whereas it is moving uphill at its outer turning point during the second half of the Stark period. Near $t = \tau_{Stark}/2$, the electron occupies circular, high angular momentum states in which the wavepacket is basically at or near its outer turning point throughout several Kepler orbits. The uniform cycling of charge results in an alternating up-down motion of the wavepacket, producing the oscillations at τ_{Kepler} in $\mathcal{P}_z$.

Rapid oscillations in the momentum distribution imply the charge distribution in

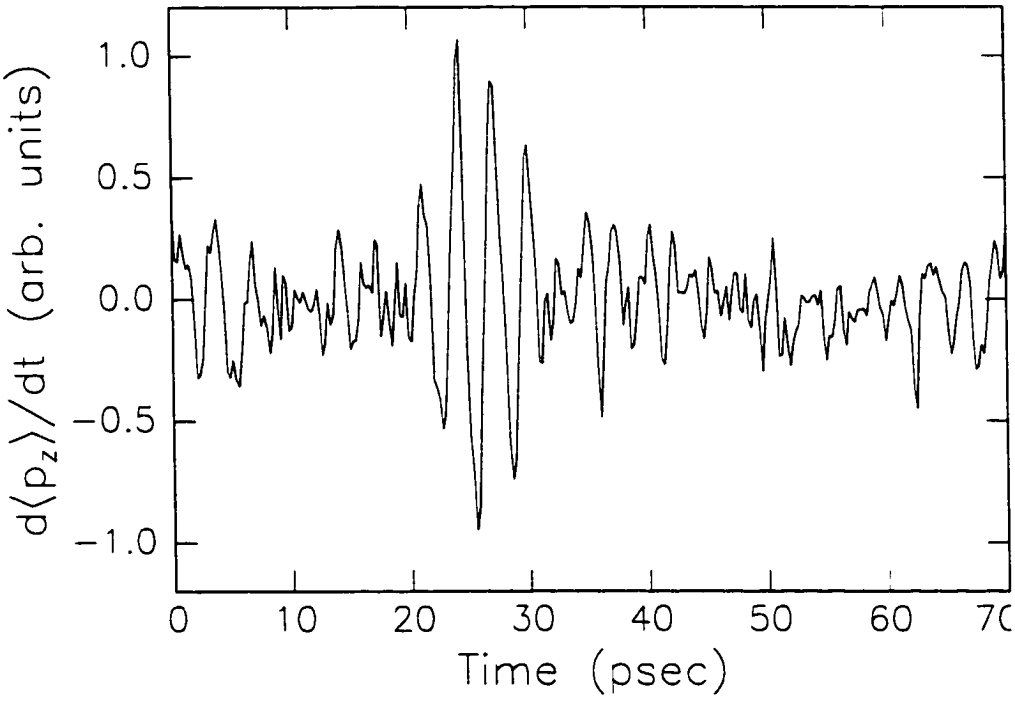

Figure 5.9: The time derivative of the measured expectation value of p_z, $d\langle p_z\rangle/dt$, which is proportional to the emitted field of the Stark wavepacket. Oscillations occur at a frequency of $1/T_{Kepler} = 0.3$ THz indicate the Stark wavepacket is a source of short pulses of Far-IR radiation.

the atom is moving primarily together in one direction, then quickly moving in the opposite direction. Such a charge distribution is an oscillating electric dipole at the Kepler frequency, $1/T_{Stark} = 0.33$ THz. The radiated field of an oscillating electric dipole has an amplitude proportional to the acceleration of the dipole moment, which is simply the time derivative of $\langle p_z \rangle$. We have measured $\langle p_z(t) \rangle$, which is extracted from the data by summing $\mathcal{P}_z(p_z) \cdot p_z(t)$, at each point in time. Plots of $\langle p_z(t) \rangle$ and $d\langle p_z \rangle/dt$ are shown in Figures 5.8 and Figure 5.9, respecfully. The slow sinusoidal appearance of $\langle p_z(t) \rangle$ results from $\mathcal{P}_z(p_z)$ being spread out for positive values of p_z as angular momentum increases and being spread out for negative values of p_z as angular momentum decreases during the first and second halves of the Stark period, respectfully. A fraction of the distribution on these elongated sides falls beneath the sensitivity of the detector and do not contribute to the evaluation of $\langle p_z(t) \rangle$. Krause and Schafer predicted this behavior in Stark wavepackets and performed calculations showing strong dipole oscillations [15]. However, they failed to present any physical arguments as to the physics behind the oscillations.

The clear, strong oscillations at the Kepler frequency indicate Stark wavepackets might be a good source of short pulses of THz radiation. We have attempted an experiment that would use Rydberg atoms as a receiver for the radiation emitted from a Stark wavepackets. This experiment is explained in greater detail in Appendix A.

5.5 Quantum Simulation

Strong dipole oscillations at the Kepler period of Stark wavepackets indicate these wavepackets are potential sources of tunable, short pulses of THz radiation. The Kepler period is defined by the constituent n-states of the wavepacket, which is con-

trolled with the excitation laser pulse. The duration of the THz pulse coincides with how long the wavepacket spends in high angular momentum states, which is related to the Stark period and is controlled by the applied static field. We would like produce a stronger, shorter THz pulse by simply controlling the state makeup of the wavepacket and the external field strength.

Quantum mechanical calculations are presented here that explore the 'tunability' of Stark wavepackets with respect to the emitted THz radiation. The study calculates $\langle z(t) \rangle$ for Stark wavepackets with varied state contribution over a range of static fields in an attempt to find trends in the behavior of Stark wavepackets which will allow arbitrary control of the emitted radiation.

We begin calculating $< \Psi(t) \mid z \mid \Psi(t) >$, in hydrogen using the linear Stark effect approximation, where $\Psi(t)$ is given by,

$$|\Psi(t) >= \sum_{n,l} a_{n,\ell} |n\ell m\rangle \tag{5.12}$$

where

$$a_{n,\ell} = \sum_{n,k} b_{n,k} e^{-\imath E_{n,k} t} < n\ell m \mid nkm >.$$

and

$$b_{n,k} =< n\ell_{init} m \mid nkm > .$$

ℓ_{init} equals to the angular momentum of the state at $t = 0$. The matrix elements $< n\ell m \mid nkm >$ are calculated using Equation 5.8. We calculate the $\mid n\ell m >$ matrix elements of $z = r\cos(\theta)$ using

$$< n\ell m \mid z \mid n\ell' m >=< n\ell m \mid r \mid n\ell' m >< n\ell m \mid \cos(\theta) \mid n\ell' m > . \tag{5.13}$$

In the linear Stark approximation, perturbing matrix elements only exist for $n = n'$. Dipole selection rules dictate that only states with ℓ differing by 1 are non-zero. The

matrix elements for r are given by

$$< n\ell m \mid r \mid n\ell + 1m >= \frac{-3n\sqrt{n^2 - \ell^2}}{2}[12]. \tag{5.14}$$

The angular matrix elements for $\Delta\ell = 1$ states are given by

$$< n\ell m \mid \cos(\theta) \mid n\ell + 1m >= \sqrt{\frac{(\ell+1)^2 - m^2}{(2\ell+3)(2\ell+1)}}[12], \tag{5.15}$$

which, for $m = 0$, has a maximum of 0.58 for $\ell = 0$ and a minimum of 0.5.

The wavepacket used in the simulation is similar to the one created in the experiment and is initially populated by nd states with $26 \leq n \leq 30$. The wavepacket evolves in the presence of a 180 V/cm static electric field along z and $< z(t) >$ is calculated over the first 100 psec of the wavepackets trajectory. We assume that the wavepacket is simply launched from its initial state and does not have a finite excitation time. A plot of $< z(t) >$ is shown in Figure 5.10. Throughout its evolution the wavepacket has clear oscillations in $< z >$ that occur at the Kepler period of the wavepacket. The oscillations are strongest shortly after $t = 0$ and near $t = 25$ psec, which approximately equal the measurement.

The state distribution of the wavepacket, $|< n\ell \mid \Psi(t) >|^2$, is plotted as a function of time in Figure 5.11. This figure shows the probability of occupying a given ℓ-state for five n-manifolds, ranging in n from 26 to 30. Angular momentum runs from $\ell = 0$ to $\ell = n - 1$ left to right for each n-manifold. There is a clear distinction between adjacent manifold state distribution evolution. The wavepacket starts in a d-state, and the angular momentum moves out to high ℓ and returns to $\ell = 2$ at the Stark period, $\tau_{Stark} = 54$ psec for the $n = 28$, but each manifold has a slightly different Stark period. An interesting feature of the distribution is the initial separation of the wavepacket to $\ell = 1$ and $\ell = 3$ just after $t = 0$. The portion of the wavepacket that starts towards lower ℓ 'reflects' off $\ell = 0$ then follows the other portion of

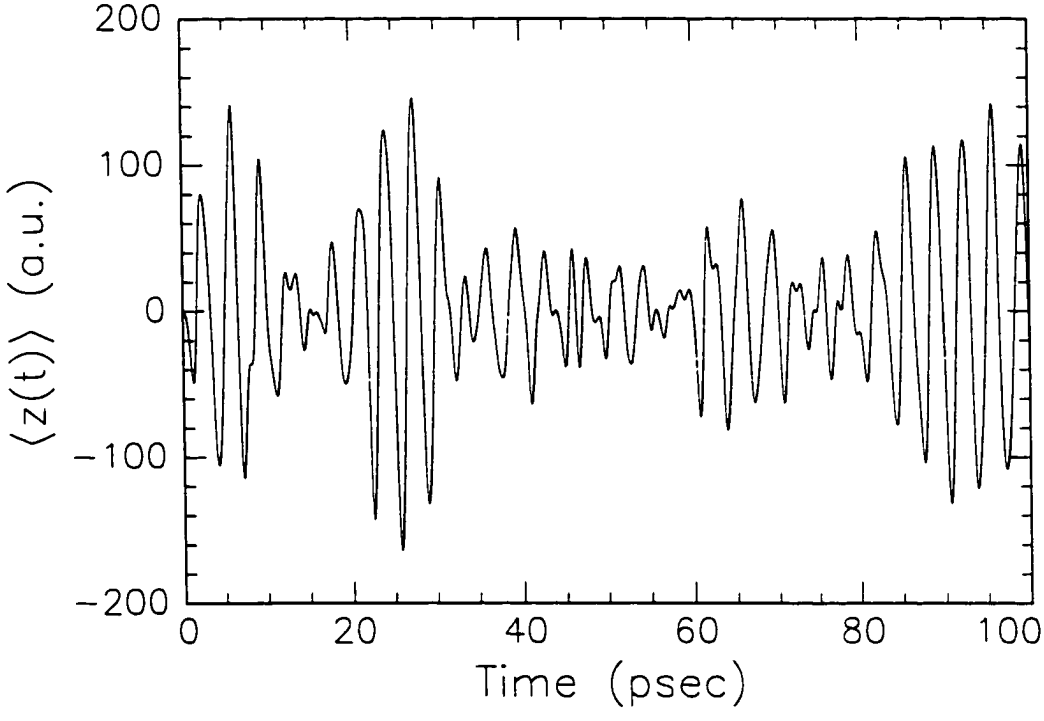

Figure 5.10: Calculated of $< z(t) >$ in hydrogen using the linear Stark approximation. Oscillations at the Kepler frequency are observe near $T_{Stark}/2$, but strong oscillations also occur at other times.

the wavepacket out to high angular momentum states. About half of the probability stays in the narrow band that reaches the highest angular momentum states available, whereas the other half spreads out over the lower ℓ-states. Because we are using the linear Stark effect, each manifold evolves independently of the other manifolds. This is a good approximation for hydrogen, but does not accurately mimic the behavior of a wavepacket in calcium, in which non-negligible state mixing between different Stark manifolds occurs. Mixing results from the non-Coulombic potential experienced by the wavepacket near the nucleus.

When considering $< z(t) >$ for calcium, or any other atom besides hydrogen, the perturbing matrix elements are not found in closed form. The presence of a finite sized atomic core changes the Coulomb potential felt by the outer electron as $r \rightarrow 0$, so we no longer have a well defined inner boundary condition to calculate the wavefunction. We know, however, that the wavefunction vanishes as $r \rightarrow \infty$. As before, we start with the wavefunction being the solution to the radial part of the Schrödinger equation for the hydrogen,

$$\frac{\partial \chi^2}{\partial r^2} + 2\left[E + \frac{Z}{r} - \frac{\ell(\ell-1)}{2r^2}\right]\chi = 0, \tag{5.16}$$

where $\chi = rR(r)$ and $R(r)$ is the radial part of the wavefunction. The two independent solutions, $f(\nu, r)$ and $g(\nu, r)$ have the forms $f(\nu, r) \sim r^{\ell+1}$ and $g(\nu, r) \sim r^{-1}$ as $r \rightarrow 0$. ν is defined by the energy, $E = -\frac{1}{2\nu^2}$ for all values of E. The asymptotic form of f and g depends on the energy as $r \rightarrow \infty$. Here, because we are working with bound wavepackets, only the case where $E < 0$ is considered.

$$f(\nu, r) \sim u(\nu, r)\sin(\pi\nu) - v(\nu, r)e^{i\pi\nu}, \tag{5.17}$$

and

$$g(\nu, r) \sim -u(\nu, r)\cos(\pi\nu) - v(\nu, r)e^{i\pi(\nu+1/2)}, \tag{5.18}$$

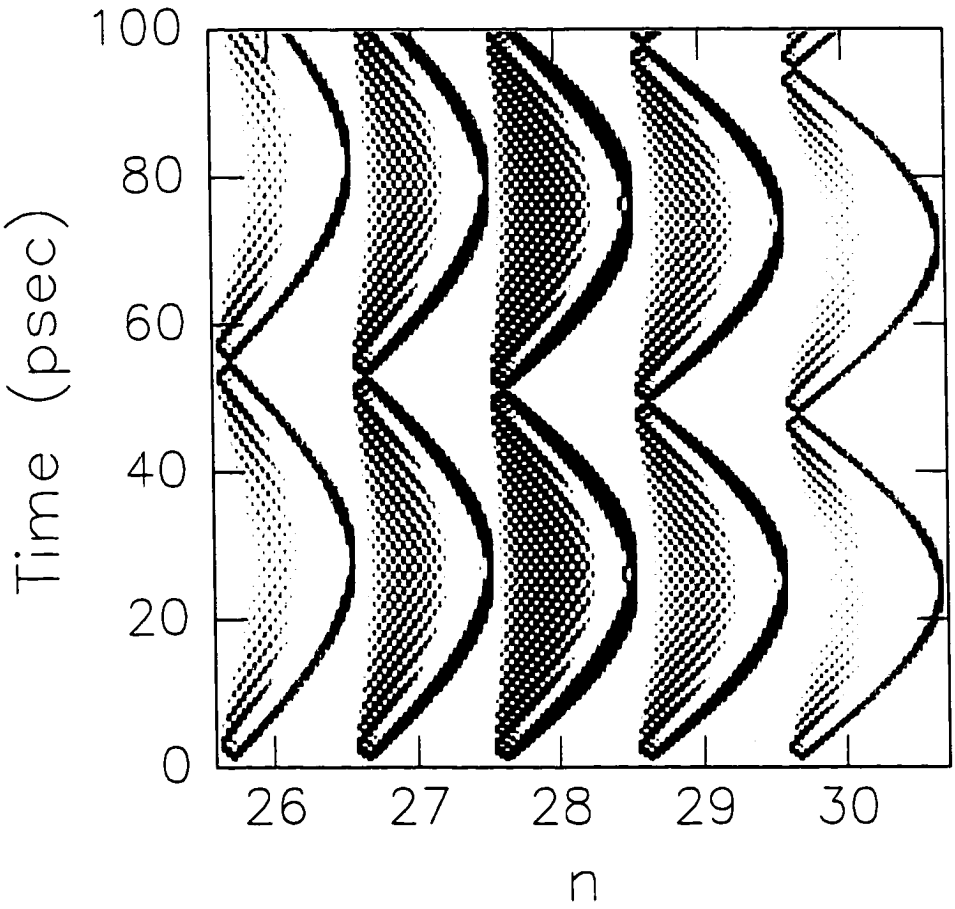

Figure 5.11: Density plot of $|< n\ell \mid \Psi(t) >|^2$ for a Stark wavepacket in hydrogen with $26 \leq n \leq 30$. This is calculated using the linear Stark effect approximation.

as $r \to \infty$. Here, $u(\nu, r)$ and $v(\nu, r)$ are defined as

$$u(\nu, r) \equiv (-1)^{\ell}\sqrt{\nu}\frac{1}{\pi}(\frac{\nu}{2r})^{\nu}e^{r/\nu}\sqrt{\Gamma(\nu-\ell)\Gamma(\nu+\ell+1)}. \tag{5.19}$$

and

$$v(\nu, r) \equiv (-1)^{\ell}\sqrt{\nu}(\frac{2r}{\nu})^{\nu}e^{-r/\nu}\left(\sqrt{\Gamma(\nu-\ell)\Gamma(\nu+\ell+1)}\right)^{-1}. \tag{5.20}$$

The most general solution for $\chi(\nu, r, \ell)$ is given by,

$$\chi(\nu, r, \ell) \propto f(\nu, r, \ell)\cos(\pi\delta_{\ell}) - g(\nu, r, \ell)\sin(\pi\delta_{\ell}). \tag{5.21}$$

For hydrogen, the coefficient of $u(\nu, r)$ must vanish to keep the exponential term from dominating as $\nu \to 0$. Therefore, we have $\sin(\pi\nu) = 0$ making $\nu = n =$ an integer. For non-hydrogenic atoms we no longer consider the wavefunction as $r \to 0$.but as $r \to \infty$. The same condition applies that the wavefunction must remain finite at large values of r, so again the coefficient of $u(\nu, r)$ is set to zero. This gives us,

$$\sin(\pi\nu)\cos(\pi\delta_{\ell}) + \sin(\pi\delta_{\ell})\cos(\pi\nu) = 0. \tag{5.22}$$

Therefore, $\nu + \delta_{\ell} = n =$ integer, giving

$$E = -\frac{1}{2\nu^2} = -\frac{1}{(n-\delta_{\ell})^2}, \tag{5.23}$$

where δ_{ℓ} is called the quantum defect. In calcium, the quantum defect changes significantly for $\ell = 2$ over the range we are interested. A few of the quantum defects are listed in Table 5.1. States with $\ell \geq 3$ have negligible quantum defects.

To account for the quantum defect, we must calculate the eigenstates of the atom in a static electric field by constructing a perturbation matrix [16]. The elements in the matrix are $< n\ell m \mid z \mid n'\ell'm' > = < n\ell m \mid r \mid n'\ell'm' >< n\ell m \mid \cos(\theta) \mid n'\ell'm' >$. We obtain the eigenstates and the corresponding eigenfunctions for the atom by

n	δ_s	δ_p	δ_d
20	2.34	1.88	1.01
21	2.34	1.88	1.04
22	2.34	1.88	1.06
23	2.34	1.88	1.09
24	2.34	1.88	1.11
25	2.35	1.88	1.13
26	2.35	1.88	1.15
27	2.35	1.88	1.16
28	2.35	1.88	1.18
29	2.35	1.88	1.19
30	2.35	1.88	1.20
31	2.35	1.88	1.21
32	2.35	1.88	1.22
33	2.35	1.88	1.23

Table 5.1: Quantum defects, δ_ℓ, for calcium. The d-state quantum defect changes significantly over the considered n-state range.

diagonalizing the perturbation matrix. The $< z >$ matrix elements are no longer trivial to calculate. The wavefunctions are generated using a Numerov routine, and explicit integration is performed to calculate $< n\ell m \mid z \mid n'\ell'm' >$. However, the angular matrix elements are the same as before.

Diagonalization of the perturbation matrix generates the eigenenergies of the system which are used to calculate the time-dependent state distribution as well as $< z(t) >$, which was calculated above for hydrogen. The eigenenergies for calcium are plotted in Figure 5.12 for a range of electric field values in a Stark map. There is a clear separation of the s, p and d angular momentum states at low fields, but these energy states 'merge' with the nearby manifolds as the applied field increases. To simplify the calculation and parallel the experiment, we always consider $m = 0$ states.

The angular matrix elements are unchanged, so the n, n' matrix elements are

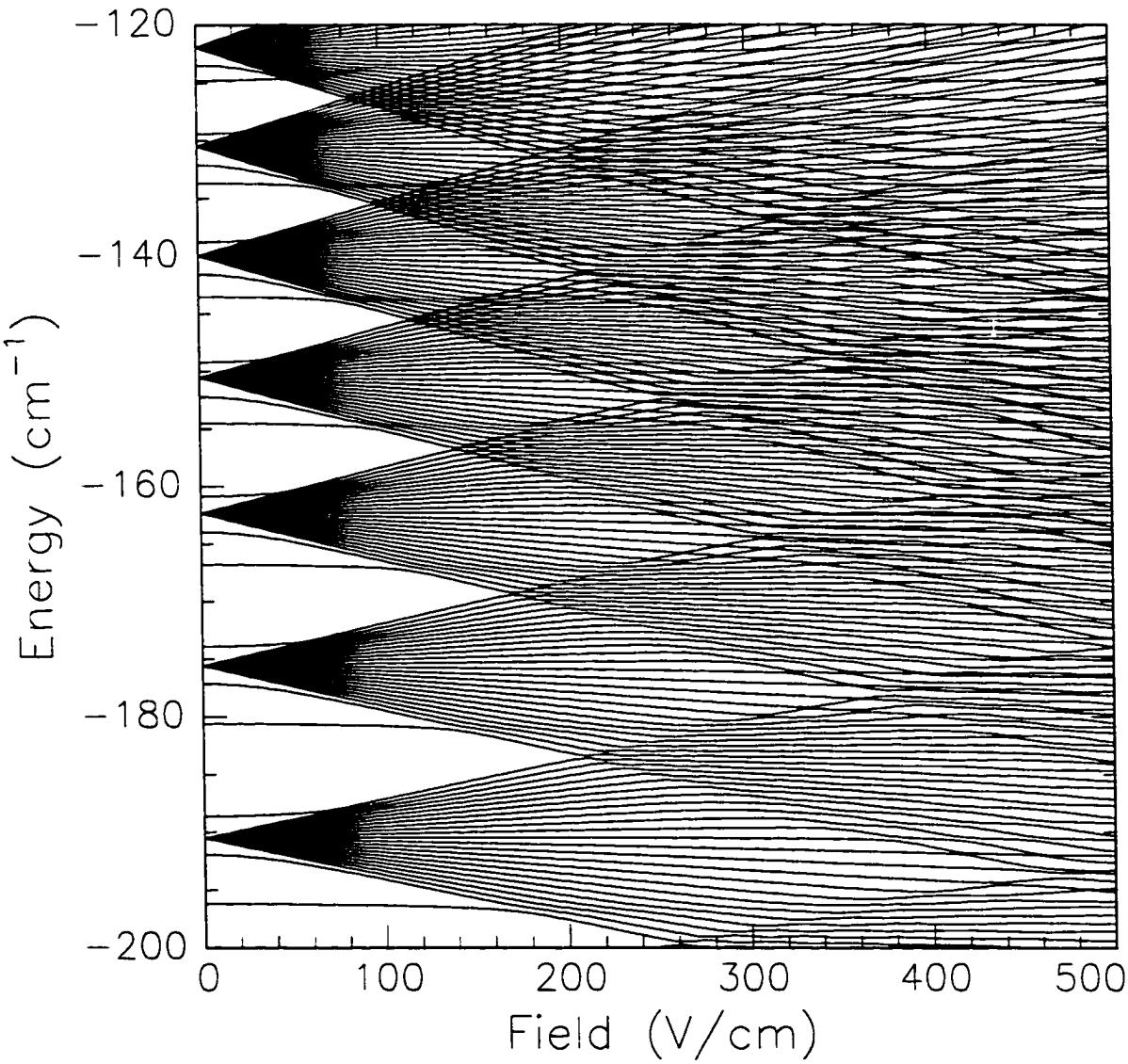

Figure 5.12: Stark map for calcium showing the energy eigenstates for the $24 \leq n \leq 30$ manifolds as the electric field strength is increased. The quantum defects for the s, p and d states lift their degeneracy with their respective manifold.

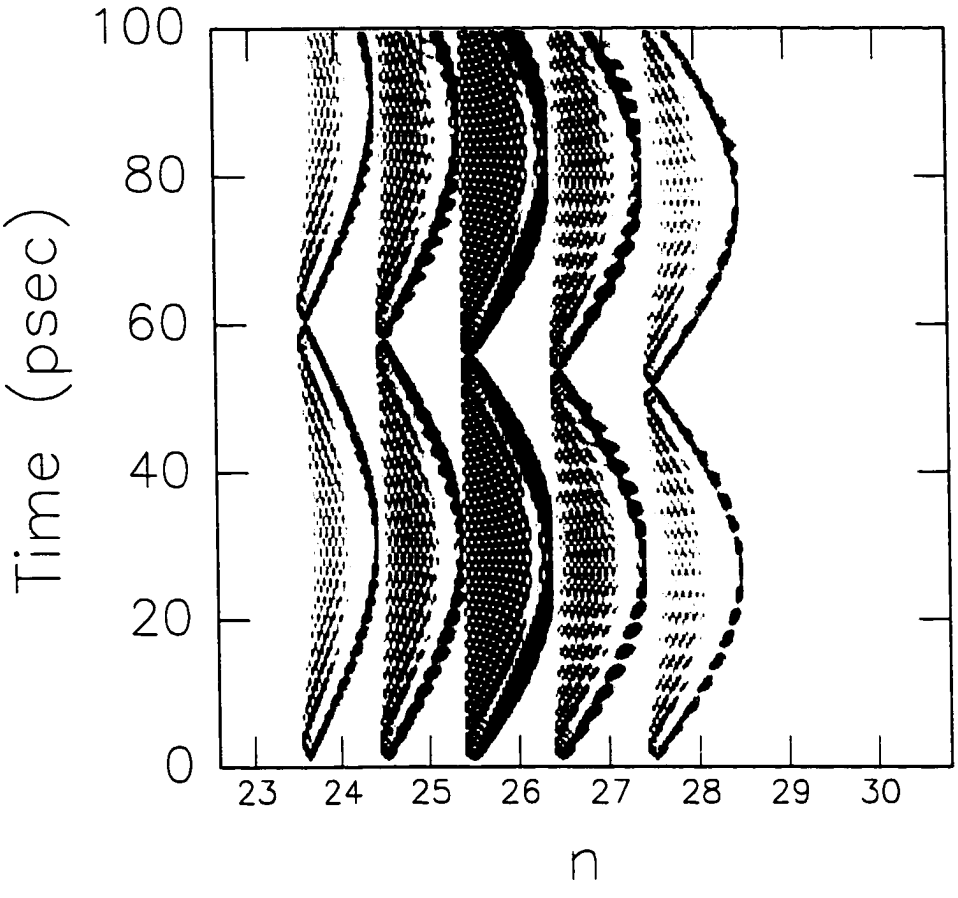

Figure 5.13: Density plot of $|< n\ell \mid \Psi(t) >|^2$ as a function of time for hydrogen.

limited to those with $\Delta\ell = 1$. The eigenvalues and eigenfunctions of the system are generated by diagonalizing the perturbation matrix. The eigenfunctions describe the makeup of each $|n'km >$ state in the $|n\ell m >$ basis set of states, from which we generate the time-dependent wavefunction for a Stark wavepacket. The time-dependent $\mid n\ell m >$ state distributions for hydrogen (all quantum defects are zero in this case) and calcium are plotted in Figures 5.13 and 5.14, respectively. For both, the wavepacket starts in a d-state with $24 \leq n \leq 28$ with a 180 V/cm static field present.

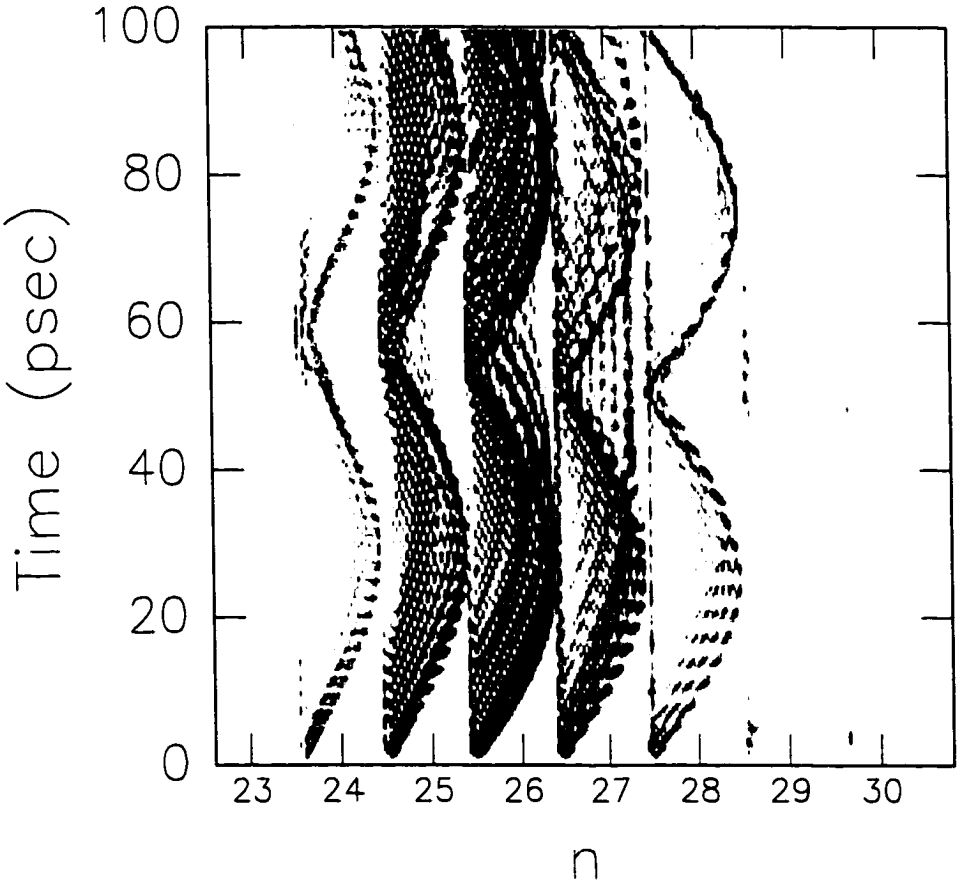

Figure 5.14: Density plot of $|< n\ell \mid \Psi(t) >|^2$ as a function of time for calcium. The angular precession is smoother in hydrogen than in calcium, yet both demonstrate time scales at precisely the Stark period, $T_{Stark} = 2\pi/3nF$. Darker regions indicate higher probabilty.

In hydrogen, we see smooth rolling of angular momentum in each manifold from low to high values and back. Each manifold arrives back at $\ell = 2$ at precisely the corresponding Stark period. There is a weak 'wavy' nature in each manifold. This 'breaking up' of the distribution was not seen in the state distribution evolution generated with the linear Stark effect in hydrogen, and it is the first sign that the linear Stark effect breaks down at even moderate electric field strengths. A small probability of being in the $n = 29$ manifold exists even though its initial probability is zero. This phenomenon could never happen in the linear approximation.

The calcium state distribution evolves differently. Two main surges of probability move from low to high values of ℓ during the first Stark period. Also, the distribution for calcium seems much more scattered and less uniform than for hydrogen. The differences are produced by the non-zero quantum defect of the s, p and d states. These states do not have similar character to the manifold and the nearest states are not uniformly spaced. Therefore, the 'rolling' from state to state is not as smooth as with hydrogen. However, the general structure shows that the majority of the ℓ-state distribution remains somewhat localized as it precesses in time.

Using the time dependent wavefunction, $< z(t) >$ is calculated for hydrogen and calcium. The radial wavefunctions contributing to the wavefunction are generated using a Numerov code, which are used to calculate $< \Psi(t) \mid z \mid \Psi(t) >$. Density plots of $< z >$ as a function of electric field and time are shown in Figure 5.15 and Figure 5.16 for calcium and hydrogen, respectively. The wavepackets have an initial state population of $25d = 5\%$, $26d = 10\%$, $27d = 80\%$, $28d = 10\%$, and $29d = 5\%$. Lighter shading indicates a more positive value of $< z >$. As with the state distributions, these plots differ significantly.

The evolution of the calcium wavepacket has several interesting features. An

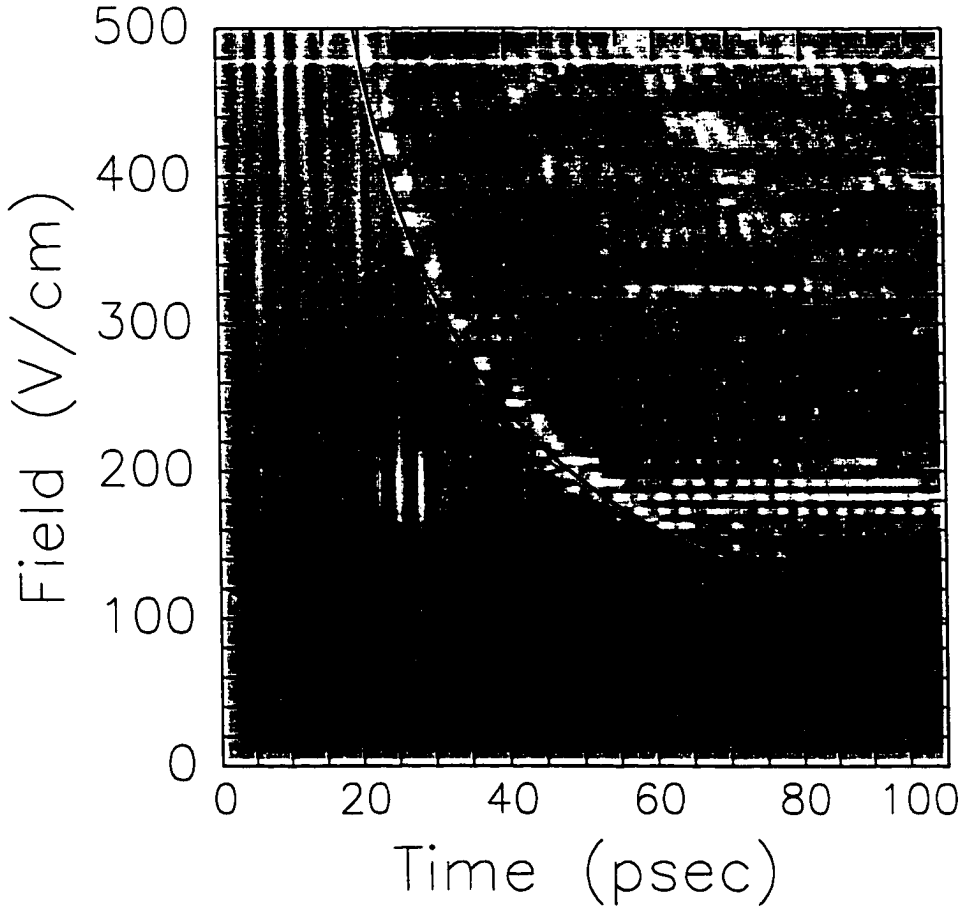

Figure 5.15: Density plot of a calculation of $< z >$ in calcium as a function of time and static electric field for a wavepacket centered on $n = 27$. Oscillations in time at the Kepler period $T_K = 2\pi n^3 = 3.3$ psec are seen in both atoms near $T_{Stark}/2$ for $F < 200$ V/cm. The solid line shows the Stark period for the wavepacket at the given field. There is a clear change in the behavior of the of $< z >$ at times after the first Stark period, when scattering of the low-ℓ wavepacket disrupts the smooth evolution.

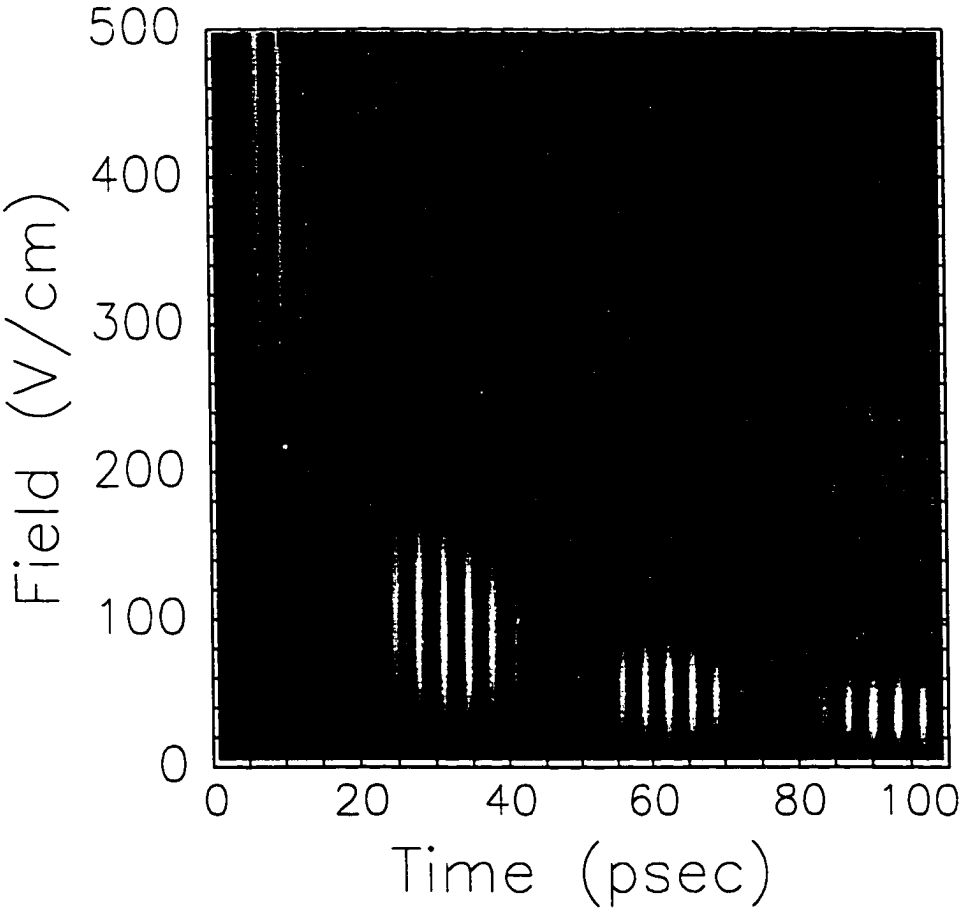

Figure 5.16: There is no significant core scattering in hydrogen, so the evolution of $< z >$ continues smoothly, even after T_{Stark}. Our measurements was made at $F = 180$ V/cm and the calculation shows a single packet of oscillations in $\hat{z}$ at this field which agrees with the measurement.

overall broad, dark band (representing negative values) in the density plot at fields less than 135 V/cm indicates the wavepacket is generally being pulled to one side of the atom. Looking at the Stark map for calcium, the d-state energy level first merges with the $n = 26$ Stark manifold around 135 V/cm. At higher electric fields, $< z >$ strongly oscillates about $z = 0$ at the Kepler frequency near $t = T_{Stark}/2$. The oscillations reflect our measurement of the wavepacket's dynamics. The solid line drawn through the plot indicates the Stark period for the wavepacket at the given electric field. The evolution of $< z(t) >$ progresses smoothly until $t = \tau_{Stark}$, and then seems to bounce sporadically afterwards. This behavior is found at all electric field strengths. At the Stark period, the wavepacket has returned to small angular momentum values and scatters off the atomic core. The scattering can disrupt the coordination of the wavepacket moving back towards large angular momentum states and the uniform angular impulse delivered to the wavepacket in the first Stark period is not seen in the subsequent Stark periods.

In contrast, there is no core scattering in hydrogen, and a smooth evolution in $< z >$ is observed well past the first Stark period. The wavepacket needs to be radially localized for the charge circulation to produce strong oscillations in the electronic dipole moment. The small shift in time of the oscillations in hydrogen relative to the oscillations in calcium may be due to the electronic distribution of the wavepacket being most localized at a slightly different time. Another difference seen in the calculation for hydrogen is $< z >$ is generally negative at all times and fields. A shift in $< z >$ to a mean value to near zero at fields strong enough for the Stark manifolds to cross does not occur.

In calcium, the strongest oscillations in $< z(t) >$ occur at a field between 160 and 200 V/cm, exactly at the field the experiment was performed. At lower fields,

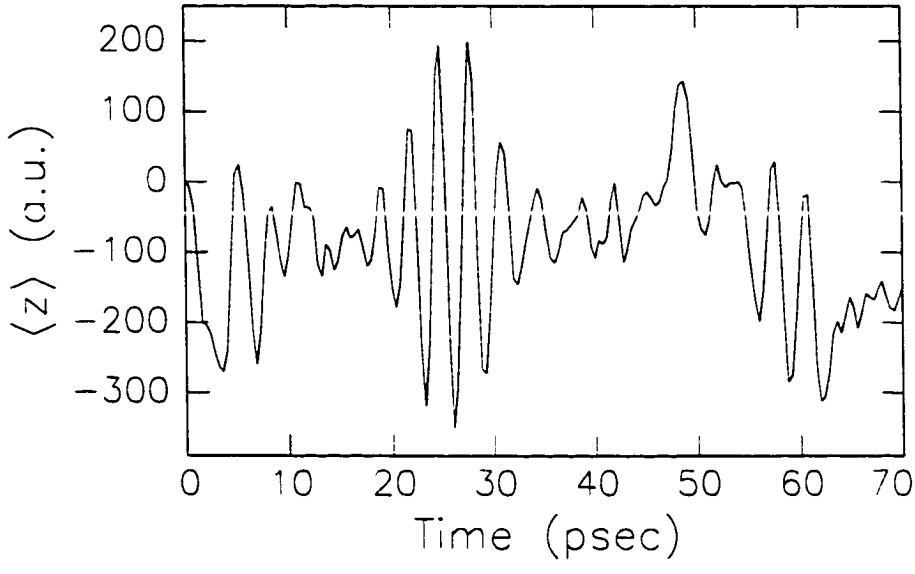

Figure 5.17: Calculation of $< z(t) >$ for a wavepacket in calcium with $N = 27$ in a 183 V/cm static electric field.

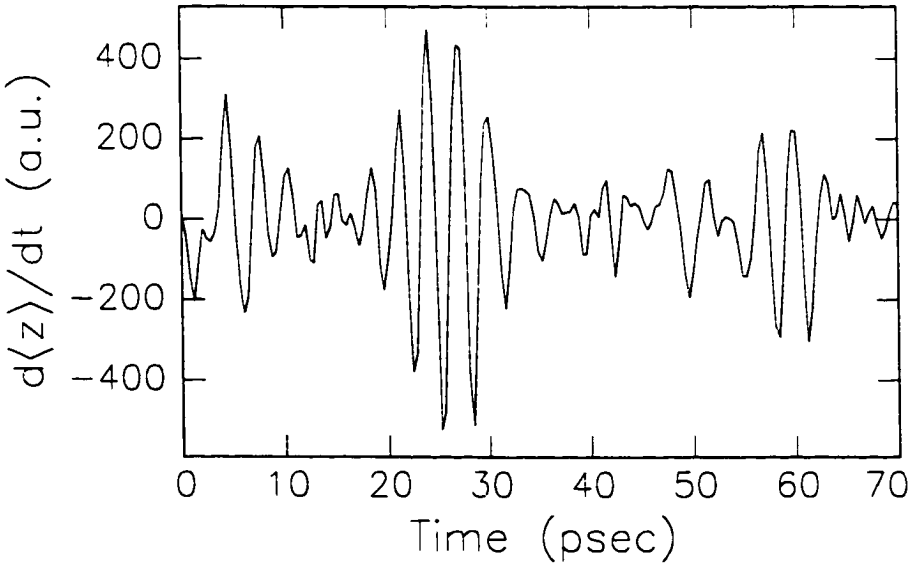

Figure 5.18: Calculation of $d < z > /dt$ for a wavepacket in calcium with $N = 27$ in a 183 V/cm static electric field.

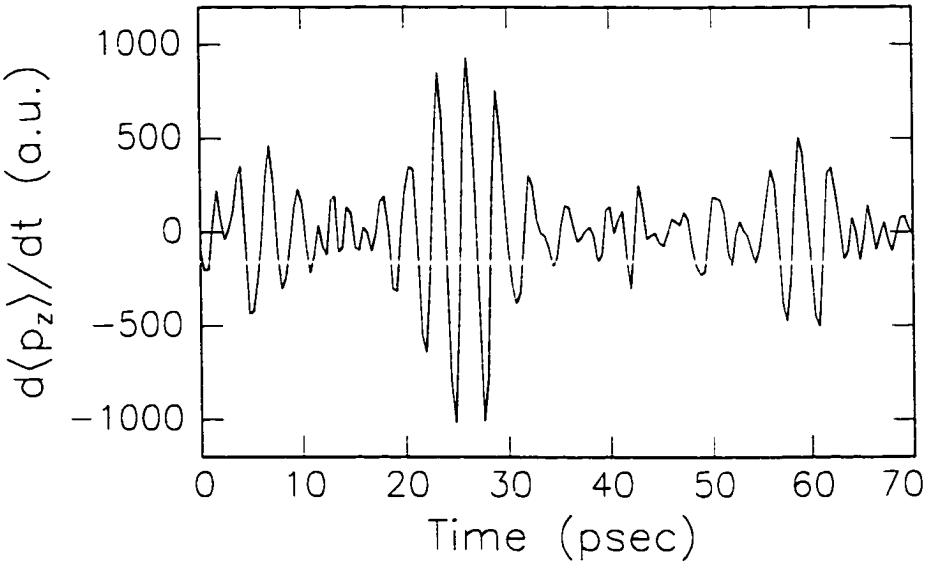

Figure 5.19: Calculation of $d^2 < z > /dt^2 \propto d < p_z(t) > /dt$ in calcium, which shows a strong resemblence to the measurement of $d < p_z(t)/dt$ shown in Figure 5.9.

the amplitude of the oscillations are not as strong and continue for over 40 psec. For fields greater than 200 V/cm there are fewer oscillations, indicating a broader bandwidth THz pulse, but the amplitude is quite small compared to the oscillations at lower field strengths. Disruption of the smooth evolution of $< z(t) >$ due to core scattering is actually a fortunate occurance. The use of a Stark wavepacket as a THz pulse emitter is enhanced because each wavepacket only emits a single pulse during its lifetime, meaning the emitted radiation is fairly well characterized.

The behavior of $< z(t) >$ is uniform as the mean principle quantum number, N, of the wavepacket is varied. The maximum amplitude Kepler frequency oscillations still occur near $t = \tau_{Stark}/2$ at fields where the $n+1$ and $n-1$ manifolds just begin to merge. The duration of the pulse does not appreciably change when the constituent eigenstates are weighted differently. Attempts to beat two wavepackets together, that were excited at different times, to produce a one- or two-cycle pulse of THz

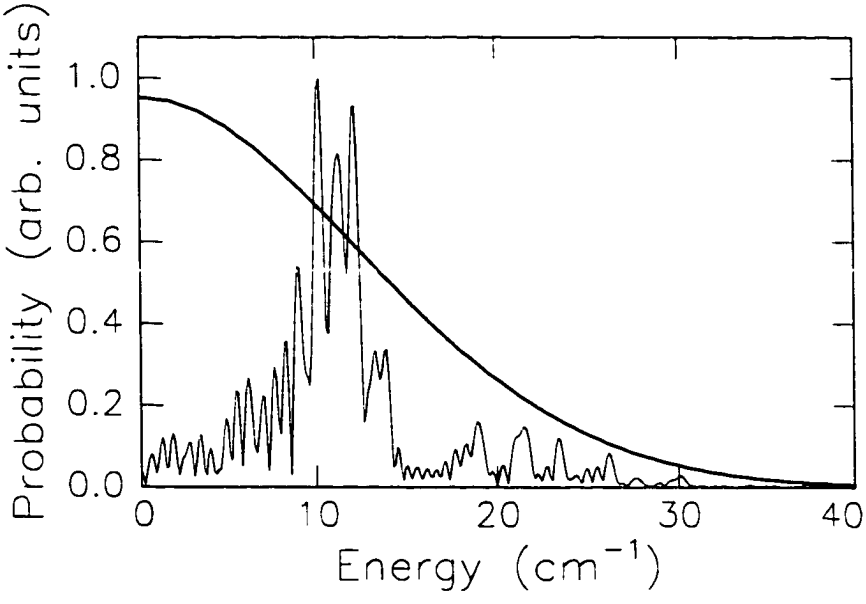

Figure 5.20: Discrete Fourier transform of $< z(t) >$ showing the frequency spectrum of the THz pulse emitted by the Stark wavepacket. The spectrum is compared to the frequency spectrum of a 1 psec HCP, plotted with the bold curve.

radiation were unsuccessful. The dipole moment oscillates at a rate defined by the energy spacing between n-manifolds. The energy spacing between manifolds is not linear. Therefore, it is difficult to produce the necessary frequency components for the generation of a one-cycle pulse.

The calculations of $< z(t) >$ for the Stark wavepacket at 180 V/cm and its derivative (which is proportional to $< p_z(t) >$) are plotted in Figures 5.17 and 5.18. Between four and five dipole oscillations occur $\sim$ 26 psec into the wavepacket's evolution and are seen in both the measurement and simulation, indicating we chose the optimal electric field to produce a THz emitter with a Stark wavepacket.

The frequency spectrum of the emitted THz pulse is shown in Figure 5.20. The bandwidth extends over $\sim$ 5 cm^{-1} and is compared to the radiation spectrum of a 1 psec Gaussian HCP. Clearly, a HCP contains the frequency components of the

THz pulse emitted by the wavepacket, but may have too much bandwidth for certain applications involving low energy transitions. The frequency spectrum emitted by a biased GaAs switch can be modulated with shaped optical pulses. This type of pulse generation has been used to drive population between close lying Rydberg eigenstates [17] but is accompanied by the large electrical noise produced by the breakdown of a highly biased GaAs wafer. Stark wavepackets do not have this problem and are potentially useful as THz pulse emitters. An experiment attempting to drive population transfer between Rydberg states using the radiation pulses from Stark wavepackets is described in Appendix A.

The motion of the electron probability distribution can be observed using the calculations above. Because we know the contributing $| n\ell >$ states in the wavepacket as a function of time we can reconstruct the wave-function spatial probability distribution and momentum space probability distribution. The p-space wavefunctions are generated by taking the Fourier transform of the spatial wavefunction, which is rather complicated in spherical coordinates. Therefore, we calculate the wavefunction at a given point, p, over a range of p values using the integral (as seen in Chapter 4),

$$\phi(p) = \sqrt{\frac{2}{\pi}} \int_0^\infty j_\ell(pr) r^2 R(r) dr, \tag{5.24}$$

where $j_\ell(pr)$ is the spherical Bessel function. A recursive routine found in Numerical Recipes [18] is used to generate the spherical Bessel functions. Plots of $rR(r)$ and $p\phi(p)$ are shown in Figure 5.21 for a range of n and ℓ states. For states with the same angular momentum, the spatial wavefunctions are in phase near the origin, whereas the momentum space wavefunctions are in phase at large values. This is expected from the Fourier transform relation of the wavefunctions.

Plots of the spatial and momentum space probability distributions of a Stark

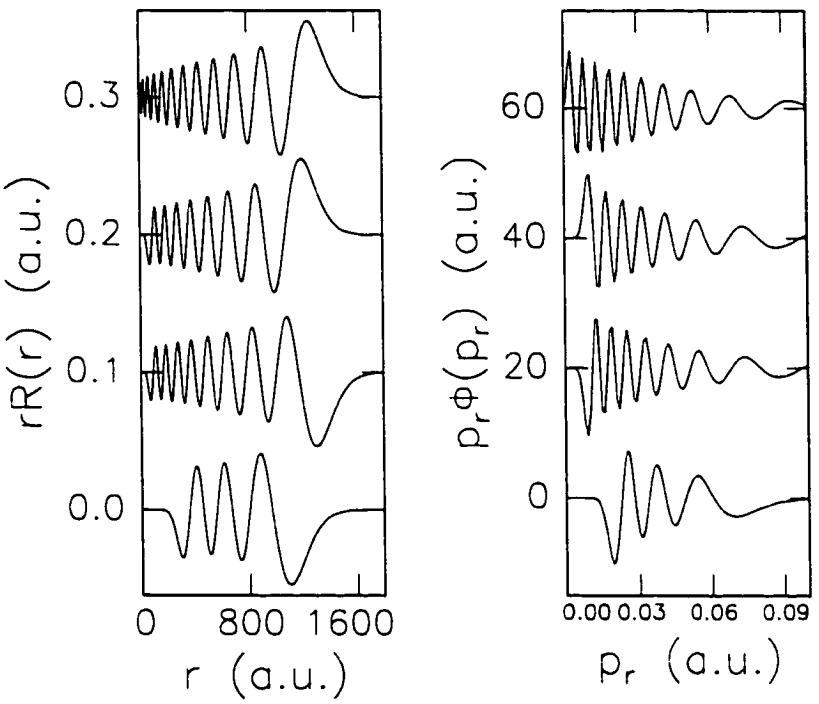

Figure 5.21: Plots of $rR(r)$ and $p_r\Phi(p_r)$ for (from top to bottom) $\mid n = 26, \ell = 2 >$, $\mid n = 26, \ell = 10 >$, $\mid n = 27, \ell = 10 >$, and $\mid n = 27, \ell = 20 >$ states. The wavefunctions differing in ℓ are clearly different, whereas the wavefunctions of the same angular momentum and different n (the middle two curves on each plot) are in phase for small r for the radial wavefunctions and for large p_r for the momentum wave functions.

wavepacket are shown in Figures 5.22 and 5.23 for times near $T_{Stark}/2$ when oscillations in $< z >$ occur at the Kepler period. Darker shading indicates high probability in the Figures. The spatial probability distribution clearly shifts from the high side to the bottom side and back in approximately 3 psec.

5.6 Conclusions

The measurement of the full time-dependent momentum-space probability distribution of a Stark wavepacket has allowed us to directly observe the full precession of the electronic orbital angular momentum and robust oscillations of the electronic dipole moment. Using classical reasoning, we are able to explain the periodic up-down asymmetry of the momentum distribution for the wavepacket along the external field axis, as well as recognize that the general structure of the distributions along $\hat{x}$ and $\hat{z}$ as being attributed to the constituent angular momentum states of the wavepacket. Our measurement techniques enables us to view the dynamics of a complicated atomic system in real time.

In addition, we have explored the possibility of 'shaping' the THz pulse emitted by a Stark wavepacket using quantum mechanical simulations. Varying the mean principle quantum number of the wavepacket changes the central frequency of the pulse, and adjusting the applied field controls the duration of the emitted pulse. Potentially, our ability to monitor wavepacket dynamics in real time will allow us to optimize the radiated pulse experimentally, instead of relying on theoretical calculations.

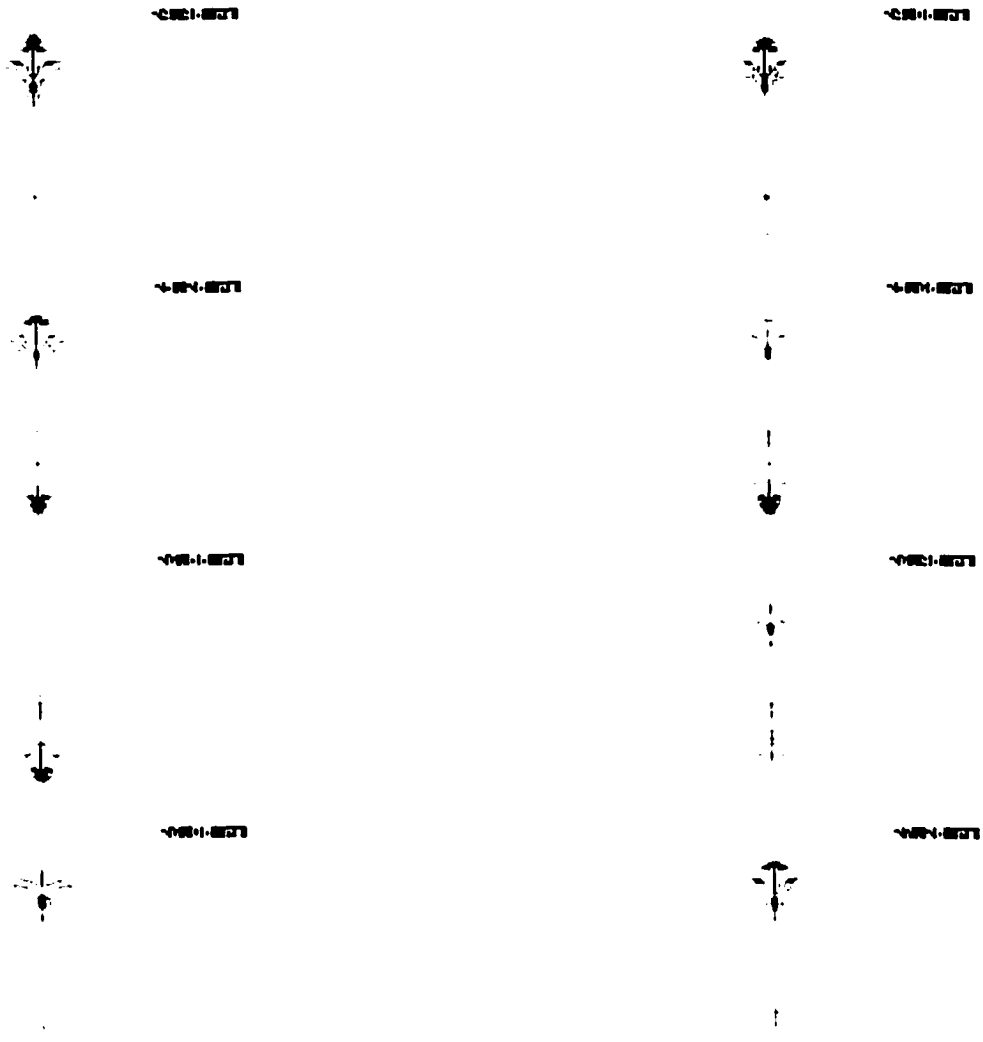

Figure 5.22: Density plots of the calculated wavepacket spatial probability distribution in the x-z plane at different times during the calcium wavepacket's evolution. The time range is 24.4 psec $\leq t \leq$ 27.2 psec in 0.4 psec time steps, starting in the top left and finishing in the bottom right. A full cycle of the $< z >$ oscillation at the Kepler period is shown, and clearly the distribution moves from the high side of the plot to the bottom, and back during this time.

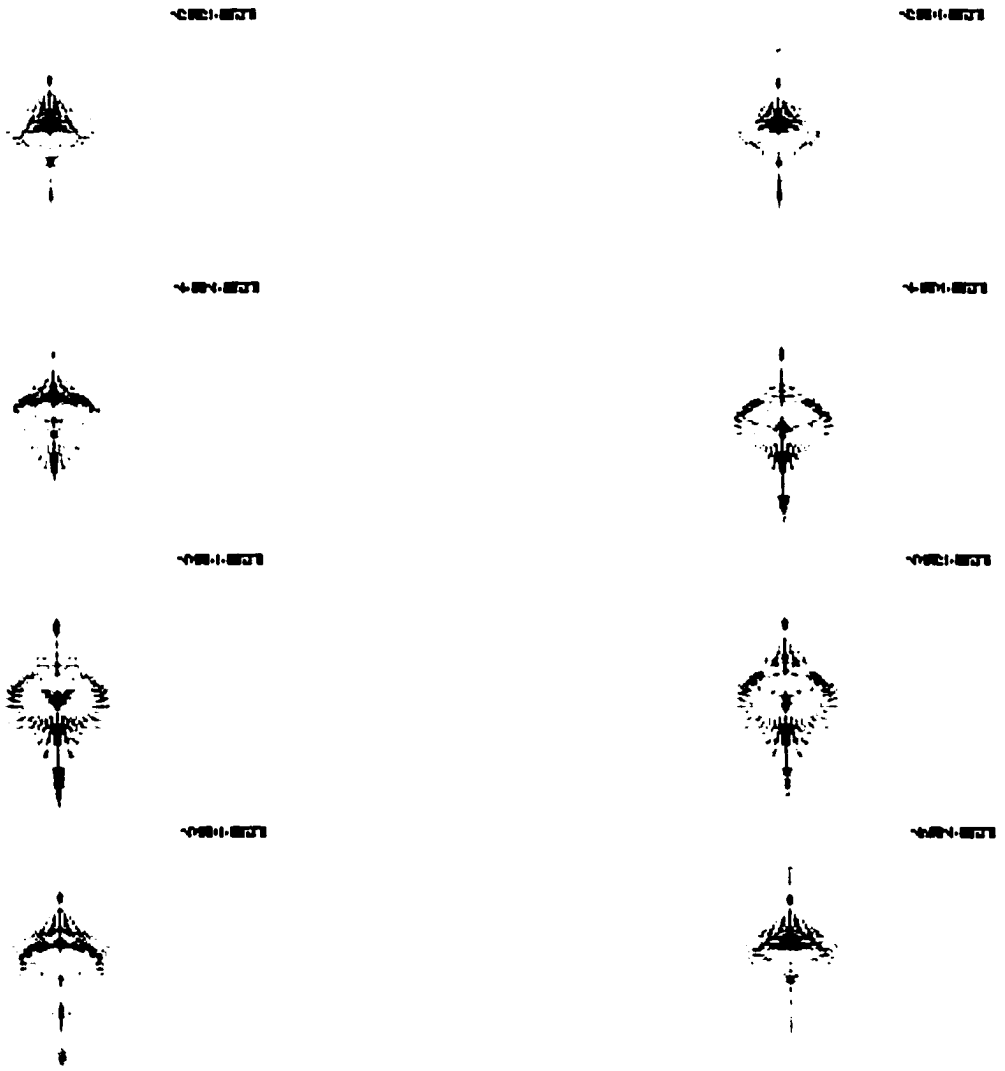

Figure 5.23: Density plots of the calculated momentum-space probability distribution in the p_x-p_z plane at different times during the calcium wavepacket's evolution. The up-down motion of the distribution is out of phase with the spatial distribution. The distribution is plotted for $24.4 \leq t \leq 27.2$ psec in 0.4 psec steps.

Bibliography

[1] M.L. Naudeau, C.I. Sukenik and P.H. Bucksbaum, *Phys. Rev. A* **56**, 636 (1997). B. Broers, J.F. Christian, J.H. Hoogenraad, W.J. vander Zande, H.B. van Linden van den Heuvell and L.D. Noordam, *Phys. Rev. Lett.* (1993).

[2] Robert Bluhm and V. Alan Kostelecký, *Phys. Rev. A* **55**, 819 (1997). P. Fassbinder, W. Schweizer and T. Uzer, *Phys. Rev. A* **56**, 3626 (1997).

[3] Jan Hoogenraad, *Rydberg Atoms in Picosecond Optical and Far-Infrared Laser Pulses*, Ph.D. Thesis, University of Amsterdam (1996) and references therein.

[4] G.M. Lankhuijzen, F. Robicheaux and L.D. Noordam, *Phys. Rev. Lett.* **79**, 2427 (1997). L.D. Noordam *et. al.*, *Phys. Rev. A* **40**, 6999 (1989). G.M. Lankhuijzen and L.D. Noordam, *Phys. Rev. A* **52**, 2016 (1995).

[5] F. Robicheaux and J. Shaw, *Phys. Rev. A* **56**, 278 (1997). F. Robicheaux, *Phys. Rev. A* **56**, 4032 (1997).

[6] R.R. Jones, N.E. Tielking, D. You, C. Raman and P.H. Bucksbaum, *Phys. Rev. A* **51**, R2687 (1995).

[7] C. Raman, T.C. Weinacht and P.H. Bucksbaum, *Phys. Rev. A* **55**, R3995 (1997).

[8] M.J. Frey, F.B. Dunning, C.O. Reinhold and J. Burgdörfer, *Phys. Rev. A* **55**, R865 (1997).

[9] Cleanthes A. Nicolaides, Charles W. Clark and Munir H. Nayfeh, *Atoms in Strong Fields*, Plenum Press, New York, NY (1990).

[10] Hans A. Bethe and Edwin E. Salpeter, *Quantum Mechanics of One- and Two-Electron Atoms*, Academic Press, New York, NY (1957).

[11] The derivation presented here closely follows the distributed notes from the *Introduction to Atomic Physics* class taught by R.R. Jones.

[12] Thomas F. Gallagher, *Rydberg Atoms*, Cambridge University Press (1994).

[13] R.R. Jones, *Phys. Rev. Lett.* **76**, 3927 (1996). F. Robicheaux, *Phys. Rev. A* **56**, R3358 (1997).

[14] The classical calculation for the momentum distributions for different angular momentum eigenstates was performed by T.J. Bensky.

[15] Kenneth J. Schafer and Jeffrey L. Krause, *Optics Express* **1**, 209 (1997).

[16] Michael G. Littman, Myron L. Zimmerman, Theodore W. Ducas, Richard R. Freeman and Daniel Kleppner, *Phys. Rev. Lett.* **36**, 788 (1976). Zimmerman *et. al. Phys. Rev. A* (1978).

[17] C. Raman, M.F. Decamp and P.H. Bucksbaum, *Optics Express* **1**, 186 (1997).

[18] William H Press *et. al.*, *Numerical Recipes in C*, Cambridge University Press, New York, NY (1992).

Chapter 6

HCP Assisted Recombination of Photo-ionized wavepackets

6.1 Introduction

Photo-ionization of an atom with a short laser pulse produces an ion and a continuum wavepacket. In the absence of external fields, the dynamics of the wavepacket is neither complicated nor very interesting. The electron distribution simply moves away from the ion at a rate defined by the energy of the excitation pulse. However, our ability to monitor the evolution of a continuum wavepacket has proven to be rather illuminating. Using $\sim$ 1 psec half-cycle pulses (HCPs) [1], we can re-attach a portion of the electron distribution to its parent ion. We have directly observed quantum and classical behavior in the wavepacket, probed the strong field response of calcium atoms, and discovered a potentially powerful method of arbitrary wavepacket manipulation through measurements of the recombination process.

Electron-ion recombination has been studied for several decades and a variety of distinct mechanisms of this process have been observed, including radiative, di-electronic and three-body recombination [2, 3]. The common link between these mechanisms is electron capture resulting from the transfer of energy and momentum

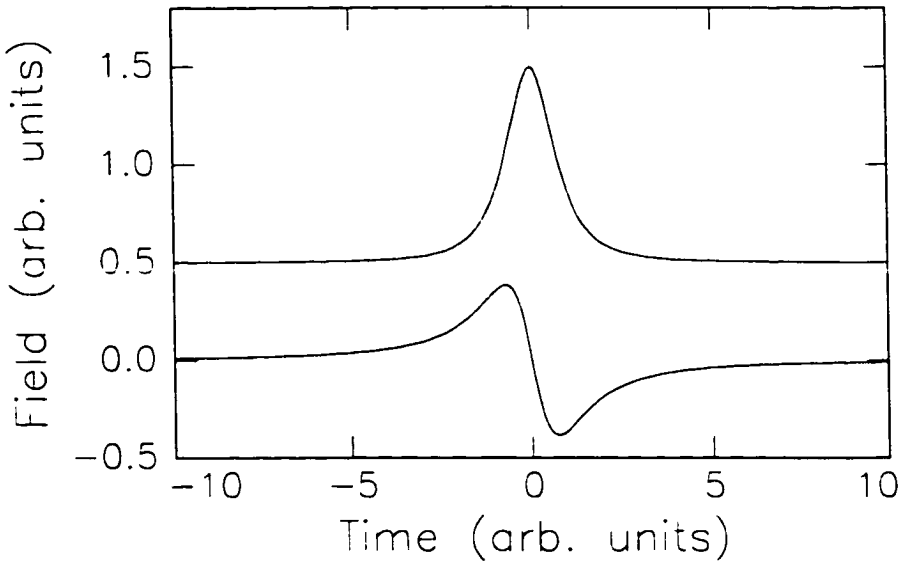

Figure 6.1: Time dependent transverse (top curve) and longitudinal (bottom curve) electric fields due to a passing charged particle. The transverse field strongly resembles the field of a HCP.

from the electron to some third body, leaving the electron in a bound state. A low energy electron becomes captured by an ion and emits a photon in the radiative recombination process [2]. This process reminds me of radiative decay of a bound excited state as a photon is emitted when an electron drops to a lower state. In three body recombination, energy is carried away from the captured electron by a massive particle in a scattering event [2] (most likely another free electron).

HCP assisted recombination closely resembles the three body recombination process, except the "collision" with the third body is simply the interaction of the unbound wavepacket with a HCP. No scattering from a nearby particle occurs A HCP of THz radiation resembles the transverse field produced by a passing charge and extracts momentum and energy from the electron, promoting capture by a nearby ion. Plots of the transverse field (top curve) and longitudinal field (bottom curve) experienced by an electron, due to a passing charge as a function of time, are shown

in Figure 6.1, for which the impact parameter is much greater than the ion-electron separation. A HCP delivers a uniform impulse along its polarization axis to the electronic distribution as the wavepacket leaves its parent ion. Considering an ensemble of classical electrons moving away from a central hydrogenic Coulomb potential (as seen in Figure 6.2) provides some insight to the recombination process. The impulse delivered by a HCP, $\vec{A}$, changes the momentum of each electron from $\vec{p}_o$ to $\vec{p}_o + \vec{A}$. The initial energy for each electron is $E = p_o^2/2 - 1/r > 0$, its final energy may be less than zero, leaving the electron bound to the ionic core. The energy of each electron changes by $\Delta E = \vec{p}_o \cdot \vec{A} + \vec{A}^2/2$. Different portions of the electron distribution acquire different energies, as shown in Figure 6.3, where energy is plotted along $\hat{z}$. The electron initially moving directly against the HCP impulse is stopped, losing all kinetic energy, and left in a loosely bound (but bound nonetheless) atomic state. The energy of a vast majority of the electrons increases, and these electrons leave the atom at an accelerated rate. The amplitude of the impulse plays a crucial role in promoting recombination. A HCP much weaker than the one shown in Figure 6.3 merely slows down the exiting electron travelling along $-\hat{z}$, and a stronger pulse reverses the direction of the electron and gives it enough energy to scatter from the core and subsequently leave.

The experiments described in this Chapter use HCPs to probe continuum wavepackets. In contrast to the experiments described in Chapters 4 and 5, we detect the bound portion of the final state distribution. Because the initial state is in the continuum, any bound population must result from HCP assisted electron-ion recombination. We probe the probabilty distribution of a continuum wavepacket by measuring the probability of recombination as a function of HCP polarization, strength, and delay with respect to continuum wavepacket excitation. In addition, a classical simulation of the

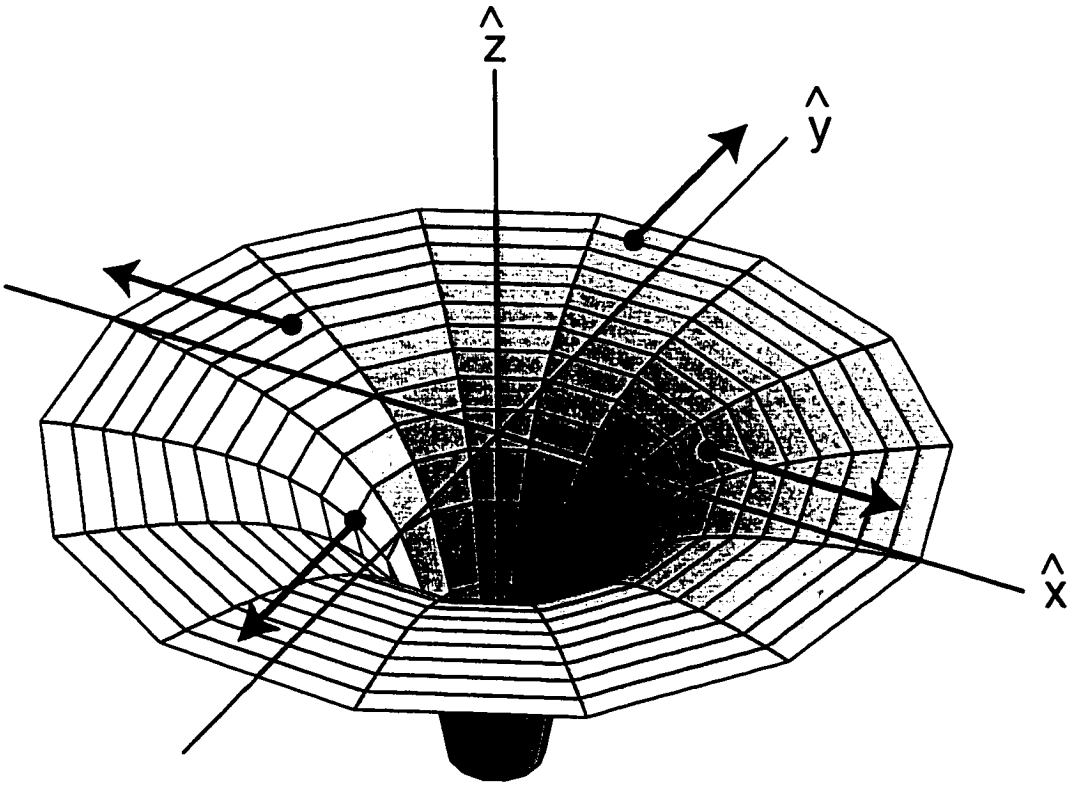

Figure 6.2: 2D potential well showing momentum-vector of different portions of a continuum wavepacket. Momentum is shown in the x-y plane and Energy is represented along the z-axis. The wavepacket leaves the atom symmetrically in this plane.

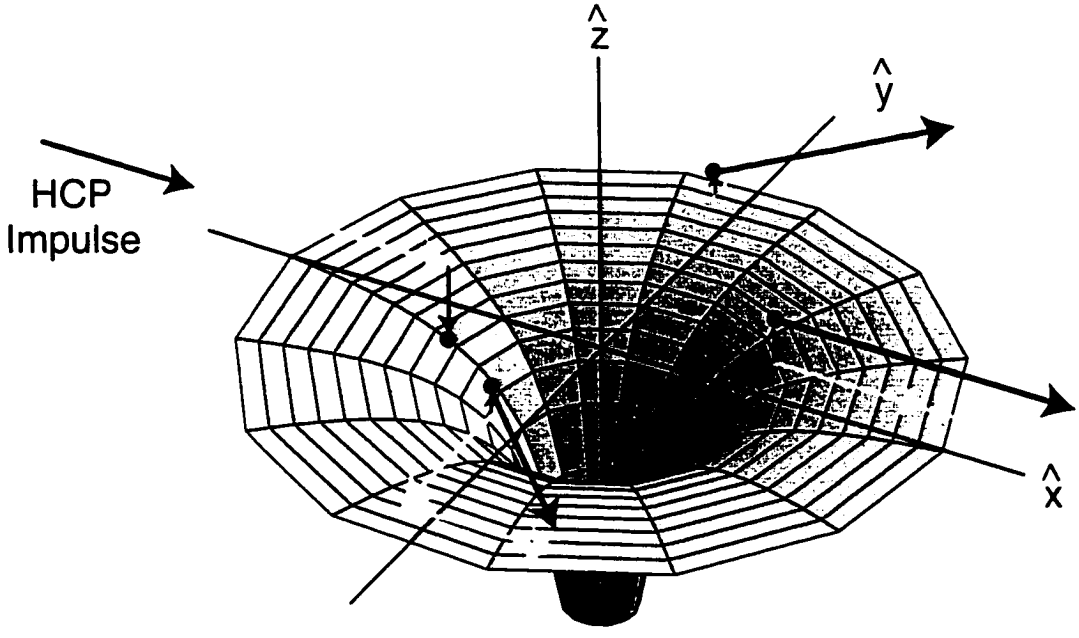

Figure 6.3: An impulse changes the momentum of different parts of the wavepacket. The final momentum vector is shown with a black arrow. The impulse perfectly offsets the momentum of portion of the wavepacket, leaving it with a total energy less than zero. Other parts of the wavepacket get an increase in momentum (and energy) and leave the atom.

dynamics of the bound wavepacket produced in the recombination process predicts that the wavepacket becomes highly localized in three dimensions. According to the calculation, the position of the dense "blob" of charge with respect to the atomic core is determined by the the polarization, amplitude, and delay of the HCP, which are easily controlled experimental parameters.

6.2 Experiment

In an effusive beam, ground state calcium atoms are excited from the $4s^2\ ^1S_0$ state to the $4s4p\ ^1P_0$ intermediate state with a 5 nsec dye laser pulse. A $4s\epsilon d\ ^1D_0$ continuum wavepacket is excited with a 392 nm, 1.5 psec laser pulse, which is created with portion of the 786 nm, 120 fsec pulse passing through a 2 cm long frequency doubling KDP crystal. Phase matching in the crystal limits the bandwidth to about 15 cm^{-1}. The KDP crystal is tuned past the ionization threshold by 0.5 nm to prevent any bound state wavepacket excitation. To ensure the pulse has a proper Gaussian frequency profile, a 0.25 m monochromater monitors the full spectrum of the pulse. Neutral density filters attenuate the 786 nm beam to prevent saturation in the KDP crystal, an effect that can produce high and low frequency pedestals in the doubled frequency pulse.

We probe the continuum wavepacket with HCPs of THz radiation. The two laser beams and HCP intersect the thermal beam of calcium atoms between two electric field plates. A long slit in the top field plate defines the time axis of this pump-probe experiment. The dye-laser beam passes through the region along the long dimension of the slit, whereas the short laser pulse and HCP beam enter the region nearly perpendicular to the slit with a $\sim 15^o$ separation between their propagation axes. The experimental configuration is shown in Figure 6.4. In this arrangement, we view

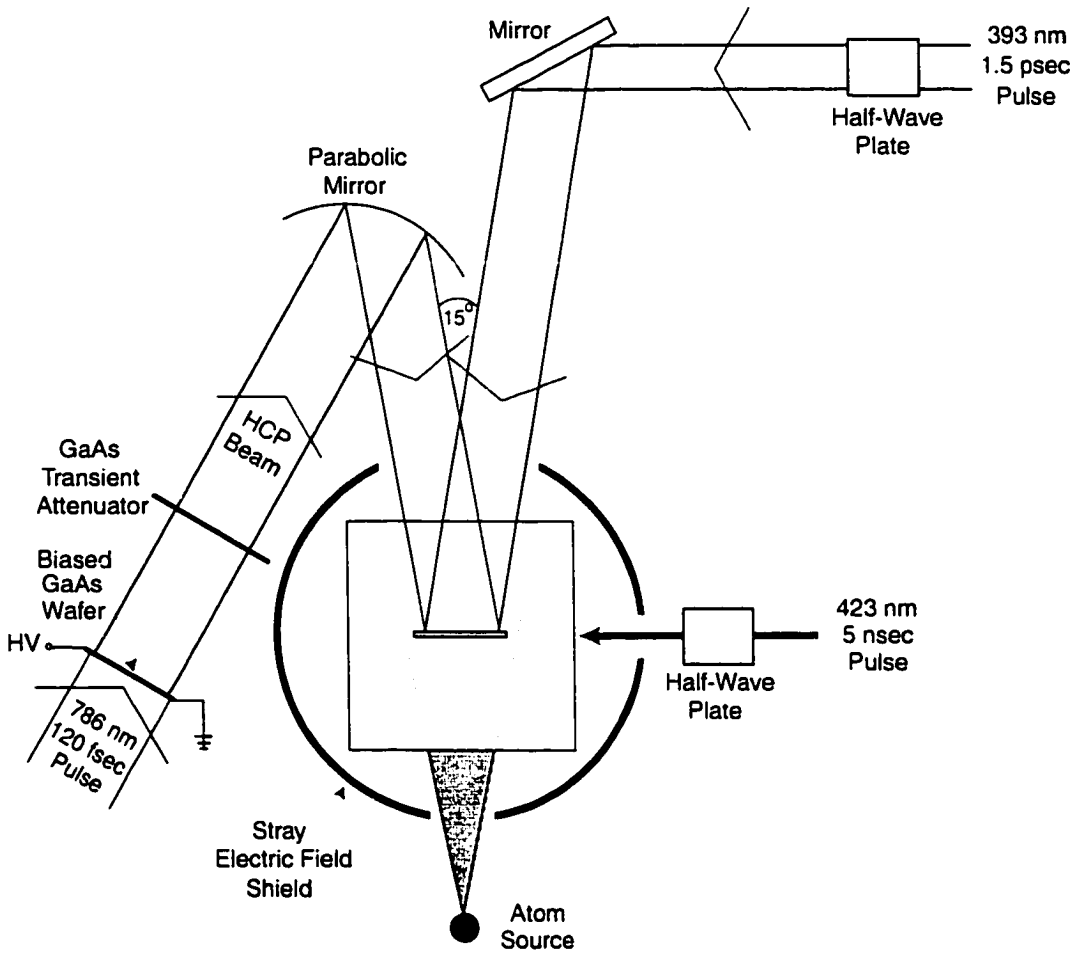

Figure 6.4: Overhead view of laser configuration.

a $\sim$ 20 psec window of wavepacket evolution with each pump-probe pair with the single-shot imaging detector. The 392 nm, 1.5 psec pulse is "telescoped-up" with a pair of cylindrical lenses to provide a nearly uniform beam intensity across the ion extraction slit.

Before reaching the atom/laser interaction region, the HCP travels about twice as far as it did for the radial and Stark wavepacket measurements. The HCP passes through an unbiased GaAs wafer, but in contrast to previous experiments, the wafer is not illuminated by a short optical pulse due to limited space in the vacuum chamber.

Non-unipolar components of the HCP, especially the oppositely polarized small peak that follows 11 psec behind the main HCP, have not significantly altered ionization probabilities when the pulse is sent through an unilluminated, unbiased wafer [5]. Apparently, illumination of the attenuating wafer by the laser light passing around the HCP generating wafer produces a transient attenuator for the HCP.

The HCP is steered into the interaction region with a large gold parabolic mirror and is centered down the middle of the slit. We test the spatial HCP beam profile by considering the ionization threshold for a sample of Rydberg eigenstates. An $n = 32$ eigenstate is created in the calcium atoms with two dye-laser pulses. The first pulse excites the intermediate step as described above, and the second pulse excites a $4s32d$ $^1D_0$ eigenstate. Both dye-laser beams propagate along the long dimension of the slit, ensuring uniform laser beam intensity across the sample of atoms beneath the slit. We measure the ionization probability for the Rydberg atoms as the HCP amplitude is increased. HCP ionization threshold of Rydberg eigenstates is a well calibrated process, so we measure the integrated ionization probability in 23 spatial bins along the slit. We assume the HCP amplitude is constant over the width of each bin. The relative field strengths are determined by finding the scale factor that matches the threshold curve for each bin to the threshold curve of the central, strongest amplitude HCP bin. The spatial HCP profile, converted to delay with respect to the wavepacket excitation pulse, is shown in Figure 6.5.

The experimental setup described above was used for two separate measurements of HCP assisted electron-ion recombination. First, the recombination probability dependence on HCP amplitude and delay is explored, providing a gauge of the optimal conditions for re-attachment. Second, the angular dependence of recombination is measured, demonstrating our ability to directly observe the spatial probability dis-

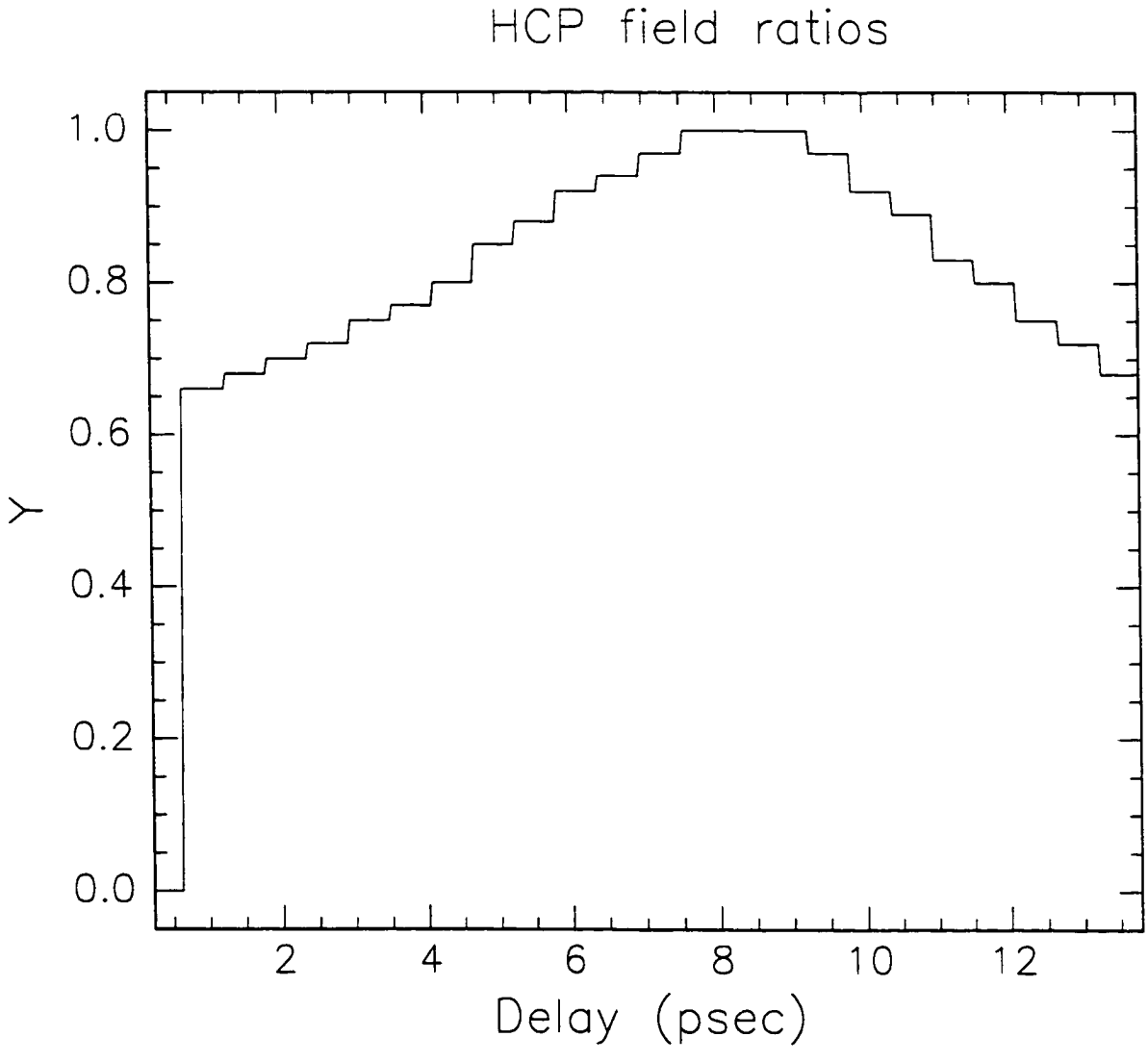

Figure 6.5: Relative HCP amplitude vs. time over the delay window of the imaging detector. The field is constant within 10 percent over a $\sim$ 4 psec range.

tribution of a continuum wavepacket.

Recombined electron-ion pairs are detected using a sequence of time-dependent electric fields applied to the capacitor plates above and below the atom/laser interaction region. Approximately 20 nsec after the laser and HCP pulses, a quick rise-time +50 V pulse is sent to the top field plate with a Behlke switch. This pulse clears the photo-excited ion sample from the interaction region. After several microseconds a +2.5 kV pulse is applied to the bottom field plate, field ionizing the neutral Rydberg atoms formed during the recombination process. The applied field pushes the ions through the slit in the upper field plate to the single-shot detector with their spatial distribution intact. The field ionization pulse delay is positioned so there is zero signal in the absence of a HCP, indicating the photo-excited ions have been swept from the interaction region.

6.2.1 Recombination Probability as a Function of HCP Amplitude and Delay

The relative probability of electron-ion recombination is measured as a function of HCP amplitude and delay. Once excited, the continuum wavepacket quickly moves away from the atom and does not return. The 15^o separation between propagation directions of the wavepacket excitation pulse and the HCP provides a $\sim$ 20 psec window for viewing wavepacket evolution, which is sufficient to observe the electron distribution fully disperse. Recombination as a function of time is directly related to the ionization signal as a function of position along the extraction slit. Therefore, we observe the time-dependence of the recombination process in real time using the imaging detector. A single line of the video image is averaged for 250 laser events at 15 different HCP amplitudes. The data is then sorted (taking into account the

non-uniform HCP amplitude as a function of time) to produce the density plot of recombination probability as a function of HCP amplitude and delay as shown in Figure 6.6.

The momentum axis is calibrated by measuring the HCP ionization threshold of a Rydberg eigenstate. The impulse delivered by the HCP is inversely proportional to the principle quantum number of the eigenstate, $A = 1/n$, at the 50% ionization level. The time axis is calibrated by adjusting the arrival time of the short laser pulse, which excites a bound wavepacket a fixed amount, and mapping the position of a recognizable feature in signal as it moves across the image.

Analysis

Quantum properties of the system define the likelihood of observing HCP assisted recombination. We will observe that the probability of this recombination process is directly related to the momentum distribution of the continuum wavepacket, and a full quantum mechanical calculation of the system would describe the dynamics completely. The presence of the HCP field mixes bound states with the constituent continuum states of the wavepacket. The probability for recombination depends on the extent of the overlap between the bound state wavefunctions and the wavefunction of the continuum wavepacket. During its interaction with the HCP, an extremely large number of n, ℓ and m states are available to the continuum wavepacket's probability distribution, which makes a quantum calculation of the recombination probability beyond the scope of this work [6]. Therefore, our analysis is based on classical arguments.

We have been working with Rydberg wavepackets and exploiting their exaggerated properties to describe their evolution with classical reasoning. The process of HCP

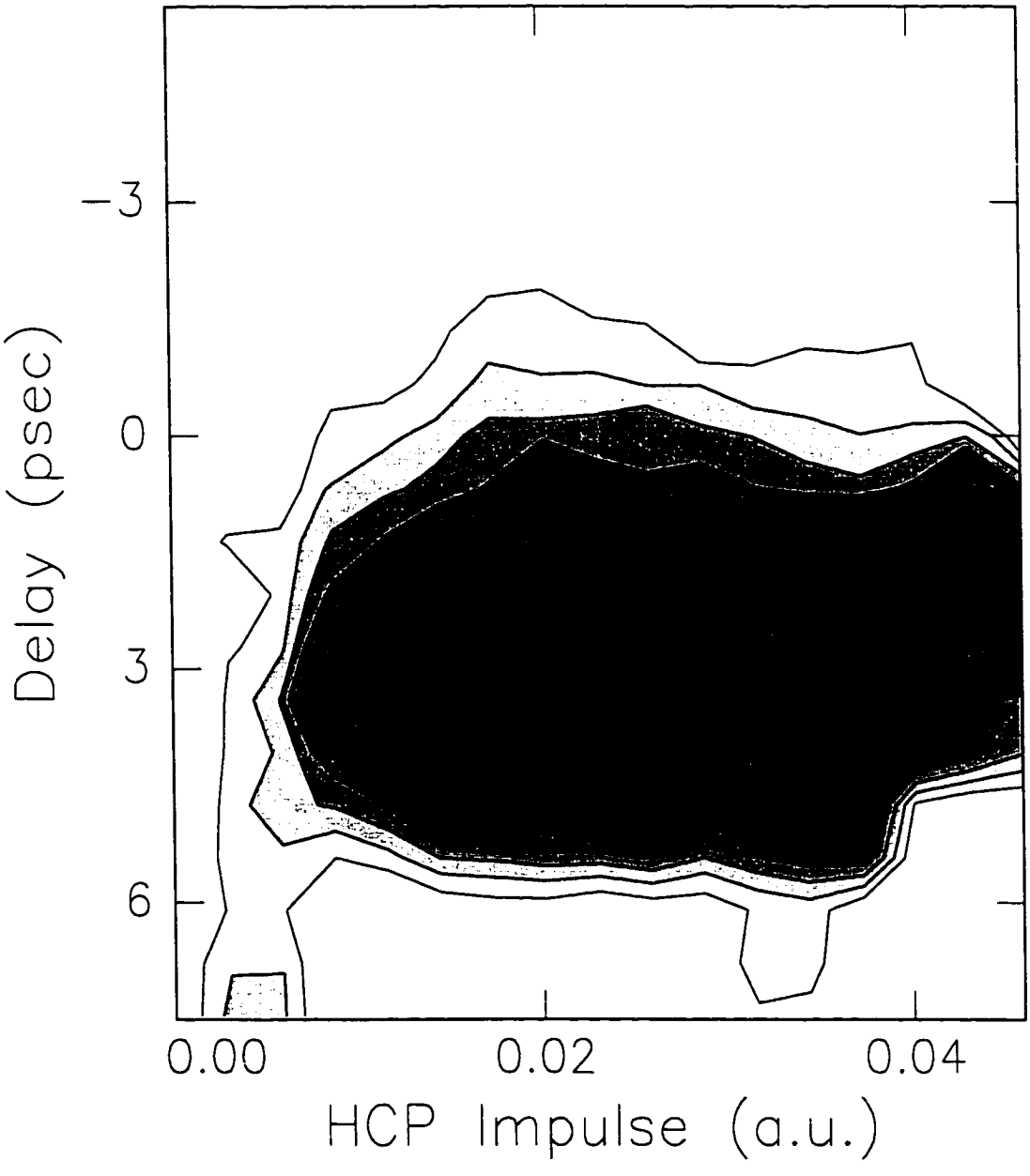

Figure 6.6: Measured probability for HCP assisted electron-ion recombination of a low energy continuum wavepacket. Darker shading indicates higher probabilty. The maximum recombination occurs for $A \approx \sqrt{2E} \approx 0.02$ a.u.

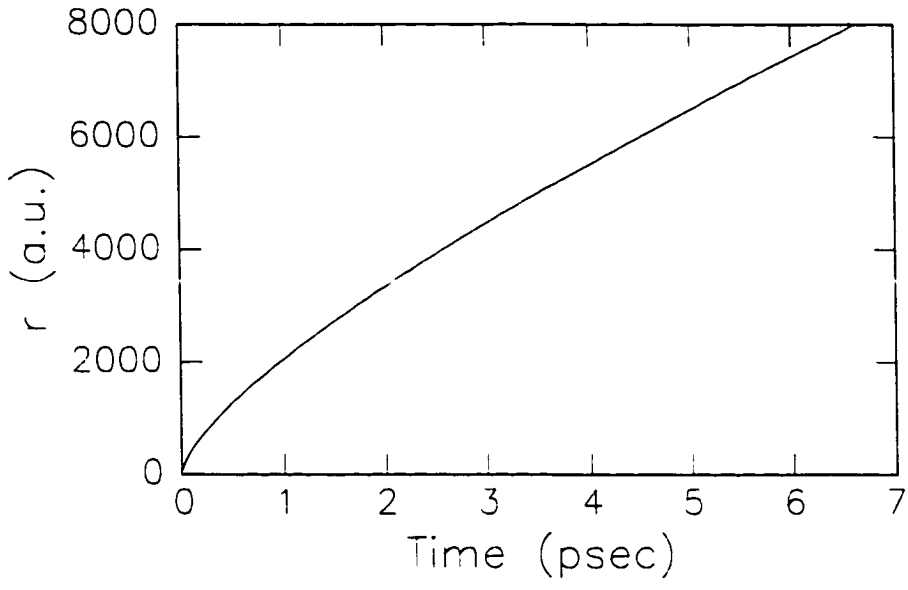

Figure 6.7: Plot of the distance from the atomic core a 25 cm^{-1} wavepacket is as a function of time. The wavepacket reaches the outer turning point of the $n = 55$ eigenstate ($\sim$ 6000 a.u.) in $\sim$ 4.5 psec.

electron-ion recombination is no exception and is favorably described with classical arguments. An electron with energy greater than zero will leave the atomic core and never return. A properly aligned HCP of a given amplitude can deliver an impulse to the free electron in the opposite direction of its travel and stop the electron, leaving it motionless in the original coulomb potential of the parent ion. The distance between the frozen electron and the nucleus determines into what bound state the electron has fallen, because that distance corresponds to the outer turning point of its new orbit.

A plot of distance from the atomic core versus time for a +25 cm^{-1} wavepacket is shown in Figure 6.7. The wavepacket quickly moves away from the nucleus, limiting the time in which recombination can occur. There is a $\sim$ 2 psec rise time in the recombination process corresponding to the convolution of the 1 psec HCP and the 1.5 psec excitation pulse. Maximum recombination is observed about 3 psec after

the wavepacket is created. The $\sim$ 1 meV shell of charge is about 4000 a.u. away from the core at this time, corresponding to the outer turning point for the $n = 44$ state. Shortly after 4.5 psec, there is a rapid drop off in recombination probability. The radius of the continuum wavepacket has become so large that any recombination places the wavepacket into very high n-states, which are field ionized by the 50 V (33 V/cm) ion clearing pulse. This field is sufficient to ionize a low angular momentum $n = 56$ Rydberg eigenstate.

Electron-ion recombination occurs if the HCP impulse extracts momentum from the electron and drops its total energy below zero, implying the impulse required for electron- ion recombination is restricted to a small range. By relating the energy of the wavepacket to the momentum change, we see why this is the case. The continuum wavepacket carries an energy, $E_o \approx 25$ cm^{-1}, in the form of kinetic energy. The momentum of the wavepacket is simply $p_o = \sqrt{2E_o}$, and the impulse delivered to the wavepacket by the HCP changes its momentum to $\vec{p}_o + \vec{A}$. For a portion of the wavepacket, $\vec{A} \approx -\vec{p}_o$, meaning the HCP "freezes" part of the electron distribution. The frozen charge remains in the Coulomb potential of the parent ion and resembles a wavepacket at its outer turning point. This wavepacket is unique because there is an asymmetry about the atomic core.

The change in total energy due to an impulse $\vec{A} = -A\hat{i}$ is given by, $\Delta E = \vec{p}_i \cdot \vec{A} + A^2/2$. The electron will recombine if $\Delta E \leq -E_o$, which occurs whenever $p_i \equiv \vec{p} \cdot \hat{i} \geq (E_o + A^2)/A \equiv p_c$, where p_c is the "critical momentum." As the wavepacket expands, its momentum distribution narrows, decreasing the probability for measuring recombination. Using this method, which is essentially the inverse of impulse momentum retrieval, we determine the probability that the wavepacket has a momentum projection greater than p_c by measuring HCP assisted recombination.

The ~ 25 cm^{-1} continuum wavepacket initially has a high probability of having $p \geq p_c = \sqrt{2E} \approx 0.02$ and has the greatest probability of recombining when getting an impulse of this value. This agrees with the measurement, which shows a maximum in recombination probability (which is only a few percent of the total wavepacket population) around $A = 0.02$.

A simulation of HCP assisted electron-ion recombination probability for an ensemble of classical electrons leaving a hydrogenic nucleus has been made [7]. The electrons each have an energy of 25 cm^{-1} and interact with a 1 psec HCP. The HCP passes through the ensemble at some delay after the wavepacket is launched, and the fraction of electrons with $E < 35$ cm^{-1} (to account for the 33 V/cm clearing pulse) is recorded. This calculation is repeated for a range of HCP amplitudes and delays. The calculated recombination probability as a function of HCP impulse and delay is plotted in Figure 6.8. The time axis has been smoothed out with a 1.5 psec Gaussian window to account for the width of the wavepacket excitation pulse. The simulation results are similar to the measured recombination probabilities, having a maximum at a HCP impulse of about 0.02.

6.2.2 Angular Dependence of Recombination

We have also used HCP induced recombination to map out the angular probability distribution of the wavepacket as it leaves the atom. The probability of recombination directly corresponds to the probability of the wavepacket having its momentum component exactly opposite the impulse direction delivered by the HCP. By adjusting the relative angle between the laser polarization axis and the HCP field axis, we map the relative probability of the low energy, continuum wavepacket moving away from the atom in each direction.

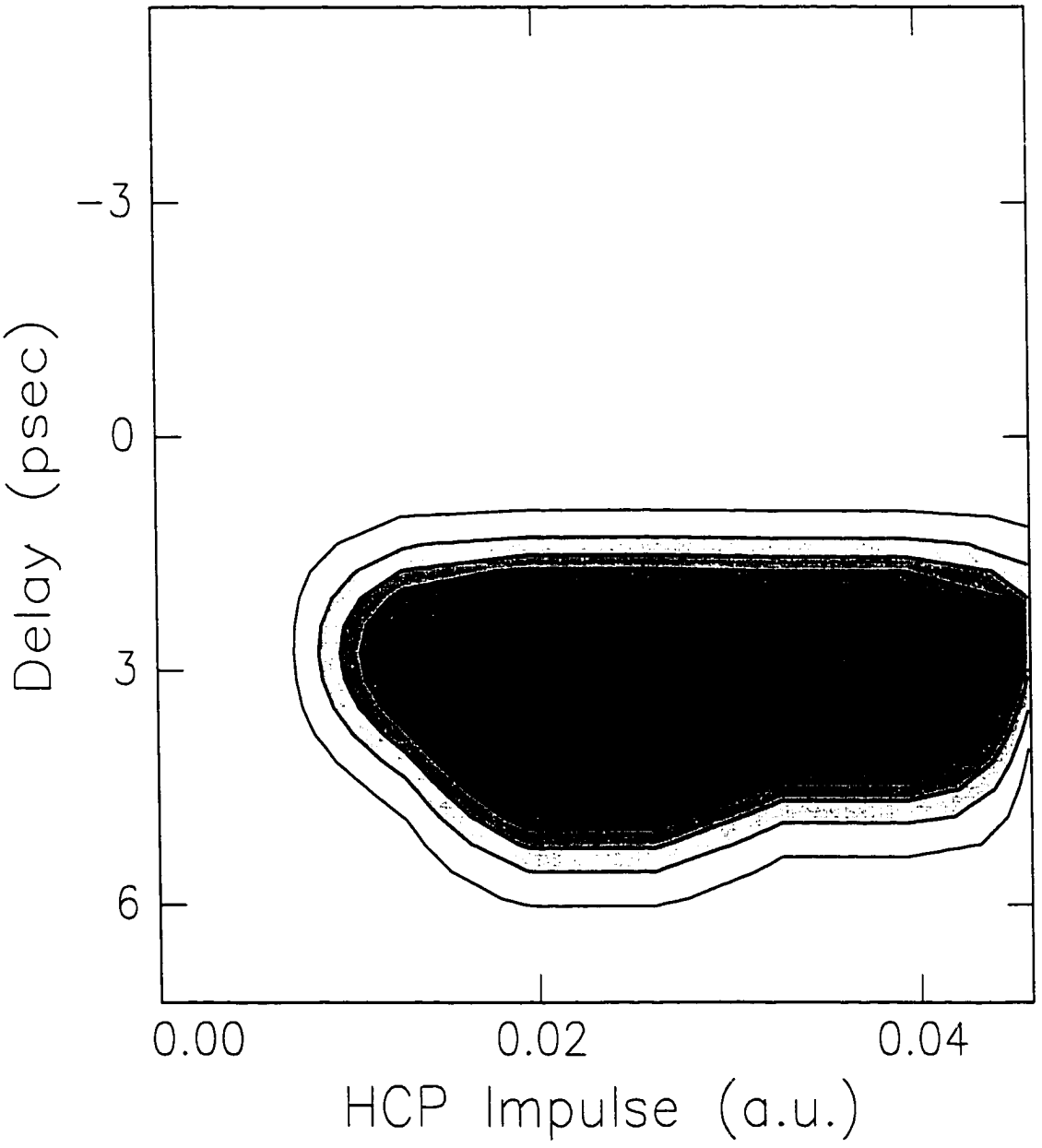

Figure 6.8: Calculated probability of HCP assisted electron-ion recombination for a 25 cm^{-1} wavepacket. Higher probability is indicated with darker shading.

The HCP remains vertically polarized throughout this exeriment. Two half-wave plates control the linear polarization of both the 423 nm, 5 nsec dye-laser pulse and the 393 nm short laser pulse. The amplitude of the HCP is fixed to deliver a $\sim$ 0.02 a.u. impulse to the photo-ionized wavepacket, maximizing the probability for recombination as discussed above. The single-shot detector provides real-time feedback of how much recombination occurs for a given HCP amplitude. The voltage delivered to the GaAs wafer is adjusted for a maximum recombination level. Although the recombination signal is maximized, the angular resolution is at a minimum. The momentum distribution is spread in the wavepacket and the $\vec{p}_o \cdot \vec{A}$ term of the final energy means a (somewhat) broad angular spread in initial momentum values which leads to recombination. Nonetheless, a clear angular dependence of HCP assisted re-attachment is observed. The polarization of the excitation lasers are adjusted identically in 4^o steps and the recombination signal is averaged and recorded. The HCP amplitude is not constant across the entire image, so the window is broken up into several bins, as discussed above, and the measurement is extracted from the central bin.

The angular dependence of electron-ion recombination is plotted in Figure 6.9A. The measurement is made in one angular quadrant, but properties of a wavepacket excited in zero field dictate that there are no top/bottom, left/right asymmetries. Hence, the data is extrapolated to the full 360^o. The continuum wavepacket is excited from a *p*-state, and conservation of orbital angular momentum indicates the wavepacket should have strong *d*-character, although there is a low ($\sim$ 10%) probability of *s*-state excitation. The plot on the right of Figure 6.9 is the expected angular wavefunction for a *d*-state, that has large lobes on the top and bottom and a small ring around the middle in the x-y plane. The measurement matches all of these

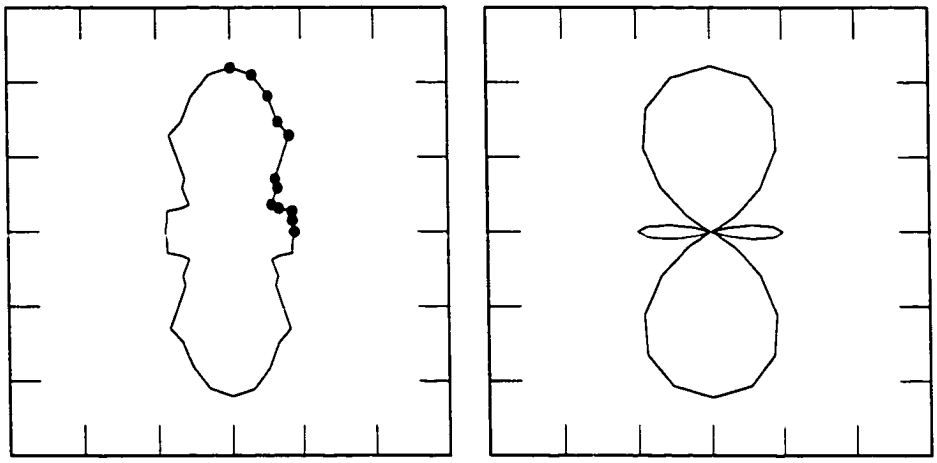

Figure 6.9: *Left*) Measured angular dependence of recombination of a 4*sd* wavepacket. Each dot represents a measurement and symmetry of the system allows this dependence to be rotated as shown. The distribution strongly resembles the *Right*) calculated angular distribution of a d-state, which is simply $Y_{2,0}$.

features, although angular resolution limitations and the presence of some s-state population prevent observation of nodes at around 45°. The recombination probability corresponds to the fraction of wavepacket population with $p \geq p_c$ along the HCP impulse axis. Given our restricted angular resolution, our measurement agrees with the expected angular recombination probability.

This measurement exemplifies the correspondence between classical and quantum mechanics in Rydberg atoms. The continuum wavepacket is classical in nature because there are no restrictions on energy levels. Similarly, the amplitude and delay of the HCP promoting recombination are determined by classical calculations of the motion of an electron leaving an ion. Quantum mechanics still reigns, however, because the continuum wavepacket must have d-character as dictated by selection rules. An elementary lesson one learns in quantum physics is the shape of electron orbitals. In this experiment, we have mapped out the d-state and explained the phenomena

using classical arguments.

6.3 Wavepacket Shaping

The experiments described above measure the probability for electron-ion recombination, but do not quantitatively determines into what states the recombined wavepacket falls. As stated above, the relative distance from the atomic core at which the electron is stopped becomes the outer turning point for its new orbit. Therefore, if the electron is stopped 5000 a.u. away from the parent ion, it resembles an $n = 50$ wavepacket. The excitation laser is tunable over a range between 390 nm and 394 nm, allowing us to produce continuum wavepackets with energies up to ~ 200 cm^{-1}.

The energy of the wavepacket determines its radial distance as a function of time, as found in this relation,

$$t = \sqrt{\frac{m}{2}} \int_{r_o}^{r} \frac{dr}{\sqrt{\frac{k}{r} - \frac{\ell^2}{2mr^2} + E}} [8], \tag{6.1}$$

where, in atomic units, $k = m = 1$, ℓ is the angular momentum, and E is the energy of the wavepacket. A plot of the distance from the core for electrons excited with a range of energies is plotted in Figure 6.10. The 200 cm^{-1} electron reaches the $n = 40$ outer turning point nearly a picosecond before the zero energy wavepacket.

Once a portion of the photo-ionized wavepacket is reattached, its anticipated evolution is interesting. A calculation of the evolution of an ensemble of classical continuum electrons irradiated with a HCP [7] shows that the recombined fraction of the electrons follows a trajectory that periodically produces large localized spatial probability spikes during its evolution. The mean energy of the ensemble is 30 cm^{-1}, and the electrons are in $\ell = 2$, $m_\ell = 0$ orbits that are uniformly launched from a hydrogenic core. Figure 6.11 shows the evolution of the ensemble at different time

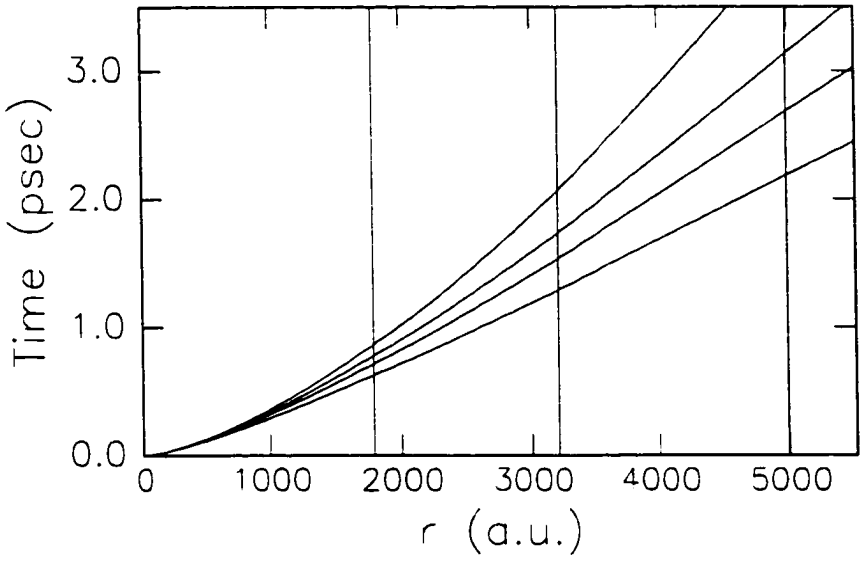

Figure 6.10: Plot of Eq. 6.1 for wavepackets with energies of 0 cm^{-1}, 50 cm^{-1}, 100 cm^{-1}, and 200 cm^{-1}. The three vertical lines indicate the outer turning point for the $n = 30, 40$ and 50 Rydberg orbits at 1800, 3200 and 5000 a.u., respectively. The zero energy wavepacket reaches the $n = 40$ outer turning point nearly 1 psec after the 200 cm^{-1} wavepacket.

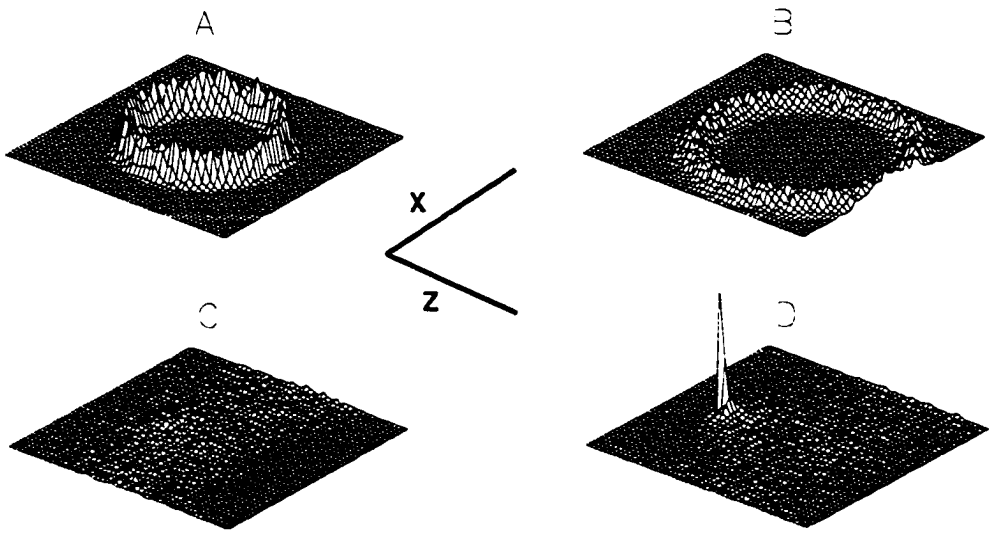

Figure 6.11: Evolution of a radial continuum wavepacket that is kicked by a HCP 10 psec after its launched. A fraction of the ensemble recombines with the host ion and its trajectory evolves into a highly localized charge distribution on one side of the atom. The frames are taken at (A) 10 psec, (B) 15 psec, (C) 47 psec, and (D) 70 psec [7].

steps after its interaction with the HCP. The distribution uniformly drifts in the $+z$ direction and spreads out during the first 50 psec. However, the reattached portion of the wavepacket converges to a very localized region approximately 70 psec into its evolution. The spatial distribution of charge around the nucleus collapses to a point and simply becomes a dense electron cloud positioned far to one side of the atom. The position of the probability spike is determined by the arrival time and amplitude of the HCP. One can imagine using HCP assisted recombination to arbitrarily place charge distribution in different regions around a nucleus, shaping wavepackets with half-cycle pulses.

6.4 Conclusions

HCP assisted recombination of well characterized free electron wavepackets and ions has been demonstrated. In doing so, we have directly observed the evolution of a low energy continuum wavepacket. The recombination probability is described very well with classical arguements, yet its angular distribution is a signature of the wavepacket's quantum nature. The classical model indicates the recombined fraction of the continuum wavepacket follows a unique trajectory, forming a dense electronic distribution on one side of the atom. Wavepackets localized in both polar and azimuthal angles have been studied before [9], but the potential capability of creating such a wavepacket with charge placed arbitrarily about the atom using successive HCPs makes this novel approach very exciting. Clearly, experiments in the near future must explore this phenomenon. Using impulsive momentum retrieval, a localized charge spike would appear as a collapse in the measured momentum-space probability distribution. The ability to arbitrarily place compact pockets of charge around an atom is an absolute demonstration of wavepacket manipulation with electromagnetic radiation.

Bibliography

[1] D. You *et al.*, *Opt. Lett.* **18**, 290 (1993). R.R. Jones, D. You and P.H. Bucksbaum, *Phys. Rev. Lett.* **70**, 1236 (1993).

[2] Yukap Hahn, *Rep. Prog. Phys.* **60**, 691 (1997), and references therein.

[3] F. Brouillard, *Atomic Processes in Electron-Ion and Ion-Ion Collisions*, Plenum Press, New York (1985).

[4] R.R. Jones, *Phys. Rev. Lett.* **76**, 3927 (1996).

[5] N.E. Tielking, T.J. Bensky and R.R. Jones, *Phys. Rev. A* **51**, 3370 (1995). The experiments described in this reference place the attenuating wafer very close to the atom/laser interaction region. The HCP and its non-unipolar components have already been collimated with the parabolic mirror before passing through the cleaning wafer, which may account for the differences between experiments.

[6] F. Robicheaux, *Phys. Rev. A* **60**, 431 (1999).

[7] The classical calculations are provided by Tom Bensky.

[8] Herberg Goldstein, *Classical Mechanics*, Addison-Wesley Publishing Company (1980).

[9] John A. Yeazell and C.R. Stroud. Jr., *Phys. Rev. Lett.* **60**, 1494 (1988). Bern Kohler *et al.*, *Phys. Rev. Lett.* **74**, 3360 (1995).

Chapter 7

Observation of Population Transfer Between Degenerate Bound-State Configurations in a $4p_{3/2}15d$ Autoionizing Wavepacket

7.1 Introduction

In the experiments discussed in Chapters 3, 4 and 5, it was assumed that only one of the two $4s$ valence electrons in calcium is involved in the wavepacket excitation, treating calcium like a one-electron alkali metal. In this Chapter, however, we consider the simultaneous excitation of both ground state electrons to high lying states.

Once one of the ground state electrons is promoted to a Rydberg state, the remaining $4s$ electron is excited to a new state using a short optical pulse via isolated core excitation (ICE) [1, 2]. Rapid excitation produces a non-stationary state of the two electron system. Total energy of the system is conserved, yet energy and momentum may be transferred from one electron to the other. Therefore, if the total energy of the system is greater than zero, one of the electrons will eventually get sufficient energy to leave the atom. The process of electron- electron energy transfer to produce an ion and a free electron is called autoionization [1]. The mechanics of the autoioinization

process is of great interest and has sparked a large amount of experimental and theoretical studies of such systems. Many experiments have considered the dynamics of 2-electron atoms [6, 5] and have probed the state configuration of such systems [7, 8], and even used an atomic streak camera [3] to probe the autionization process [4]. Measurements of these more complicated systems is an important step into learning how to manipulate electronic wavefunctions with radiation, bringing closer the reality of coherent control of atoms and molecules [9, 10].

A number of experiments, working in the frequency domain, monitor time-independent parameters to describe the eigenstates of the atom as a function of energy and angular momentum [1]. Absorption spectroscopy is a common method to determine all states accessible in the system. Careful measurements of the amplitude and width of spectral features for ICE transitions, combined with multi-channel quantum defect theory (MQDT) formalism provide the same temporal information as time-domain measurements [11]. Autoionization is a time-dependent process, and thinking of this ionization mechanism in the time domain as a classical scattering event between electrons provides a more accesible desciption of the electron dynamics.

The simplicity of a single electron orbiting an ionic core is lost to the complicated dynamics of the three-body problem of two optically excited electrons orbiting a doubly ionized atomic core. Each electron feels the combined field of the 2^+ ionic core and the repulsive field of the other electron. The experiment presented here takes a straightforward approach in monitoring specific scattering processes that occur in the rapidly autoionizing system. The oscillation between bound states is observed with time-domain measurements and are compared to an equivalent measurement made in the frequency domain.

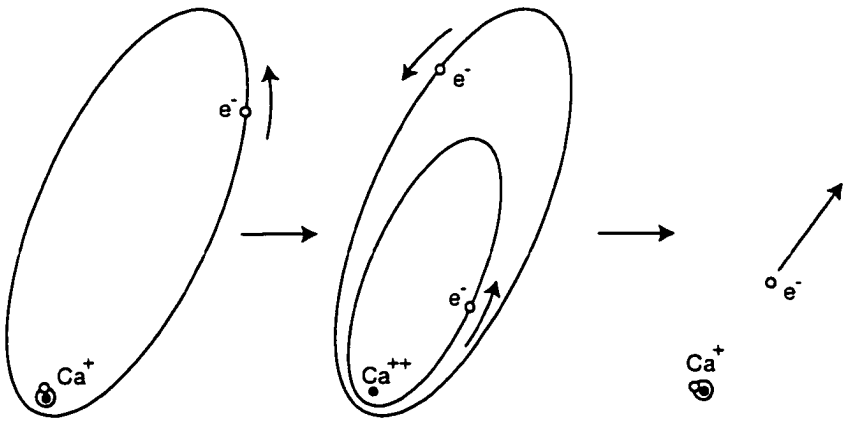

Figure 7.1: Schematic of the autoionization process in Ca. First, one electron is excited to a Rydberg state. Next, isolated core excitation of the remaining ground-state electron sends the atom into an autoionizing state. Finally, the electrons scatter off of one-another, sending one electron to the continuum and dropping the other into a lower bound state.

7.2 Autoionization

Ionization of an atom can occur in many ways. Usually, the most active electron in an atom is excited to the continuum by a direct interaction with an external source, whether it be a photon or an applied external electric field. In the autoionization process, the electron that leaves the atom gets its energy from a second excited electron in the atom. A simple picture of the autoionization process is shown in Figure 7.1. In calcium, one of the two active electrons is promoted to a Rydberg state. Through ICE [1, 2], the second ground state electron is excited to some high-lying state. Eventually, because the total energy shared by the two electrons is greater than the first ionization limit, scattering between electrons will ionize the atom, dropping an electron to a lower energy state.

Classically, autoionization occurs when the Rydberg electron scatters off the inner electron and absorbs enough energy to leave the atom. The scattering probability is a

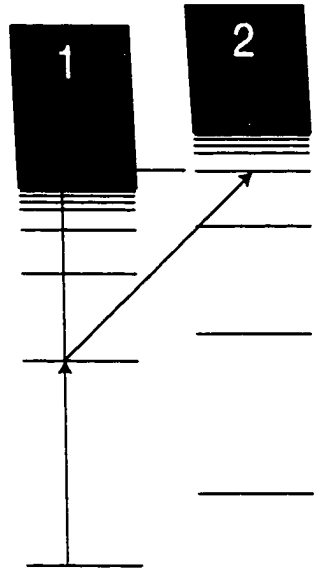

Figure 7.2: In the most simplified case, there is only one path to the continuum for an autoionizing state. A Rydberg state in (1) is sent to an autoionizing state in (2), but the only path to ionization is through (1). This Figure, and Figure 7.3 have been adapted from Figures in [1].

function of how often the electron returns to the core ($1/n^3$) [1] and how close it gets to the core, which depends on the angular momentum state, ℓ. The inner turning point for the electron varies as $r_i \approx \frac{\ell(\ell+1)}{2}$ [1], meaning lower angular momentum states get closer to the atomic core and have a higher probability of scattering into the continuum. We work with s-, p- and d-states, which, in calcium, all have a high probability of approaching the atomic core.

An energy level diagram of the autoionization process is shown in a simple system with two ionization channels in Figure 7.2. An electron in channel (1) can be excited directly to the continuum from the ground state with a combination of photons and applied fields. Conversely, the atom can be ionized by exciting a bound state in channel (2) which is degenerate with the continuum in channel (1). The overlap between the bound-state wavefunction in channel (2) and the continuum wavefunction of channel (1) determines how quickly the atom will ionize.

In actuality, there are several ionization channels in an atom. A scenerio where oscillation between bound state configurations can be seen in an example with three ionization channels as shown in Figure 7.3. A Rydberg state in channel (1) can be excited to an autoionization state in channel (2) that is degenerate with continuum, (1), or bound states, (3), in other channels. Population may transfer into bound states in channel (3) and ionize through channel (1) or return to channel (2). Each arrow represents a path by which state population can transfer between channels. The strength of the interaction between channels is determined by the overlap of the wavefunctions of the bound and continuum states [7]. A strong interaction to continuum states leads to a larger autoionization rate of the system. The interaction between two channels can be estimated with a dipole approximation, giving autoionization rates that have $1/n^3$ dependence [1].

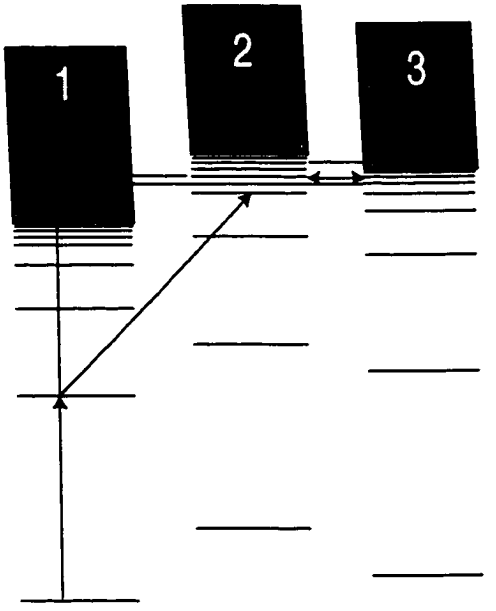

Figure 7.3: Slightly more complicated state configuration for an autoionizing state. An autoionizing state in (2) may be degenerate with the continua in (1) and (3) and ionize through either channel, or may be degenerate with a bound state in (3) from which ionization occurs through (1).

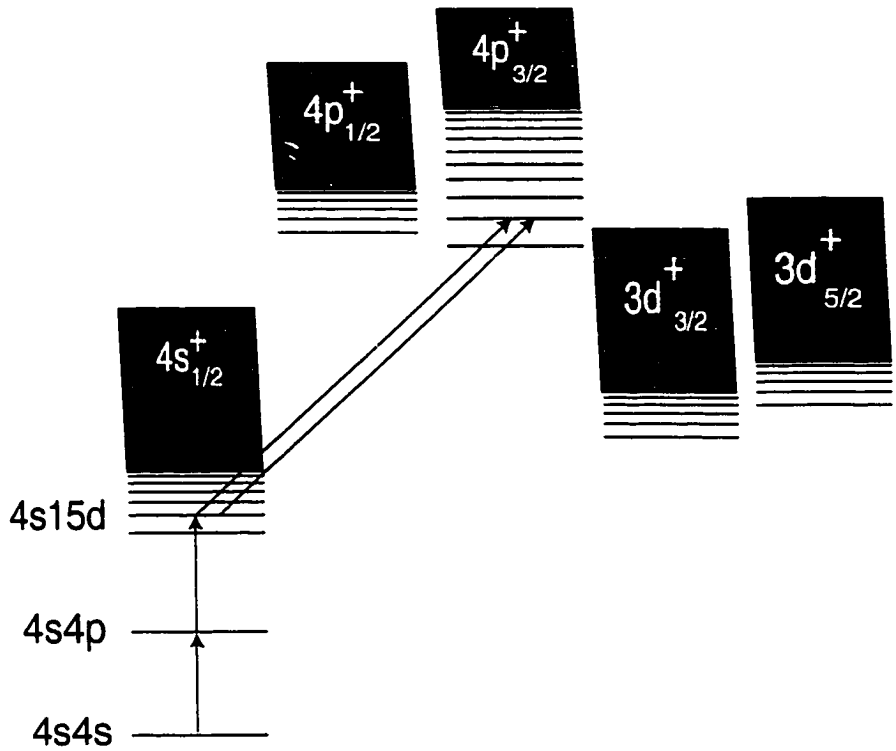

Figure 7.4: Diagram of the relevent energy levels in calcium. Each arrow represents an excitation laser pulse used in the experiment.

In calcium, the $4pnd$ state is coupled to the $4s$ continuum, as well as to bound and continuum states in other channels. Interseries interaction between different autoionizing series alters the direct ionization rate through the $4s$ channel. Figure 7.4 shows a more realistic state configuration for calcium. In the experiment, an autoionizing state is excited in the $4p^+_{3/2}$ channel. A few *nd* Rydberg states in this channel are nearly degenerate with bound states in the $4p^+_{1/2}$ channel. Population transfers into that channel, as well as ionizing directly into the continuum of the $4s^+$, $3d^+_{3/2}$, and $3d^+_{5/2}$ channels. The goal of this experiment is to directly observe a population depletion and revival of the $4p^+_{3/2}$ channel, as evidence of state mixing between bound channels.

7.3 Experiment

We monitor the evolution of an autoionizing wavepacket in a thermal beam of calcium atoms. A portion of the atoms in the $4s4s\ ^1S_0$ ground state are excited to the intermediate $4s4p\,^1P_1$ state, then to the $4s15d\ ^1D_2$ Rydberg state with 423 nm, 5 nsec and 398 nm, 5 nsec dye laser pulses, respectively. Shortly after Rydberg state excitation, a 200 fsec, 393 nm laser pulse drives the isolated core excitation (ICE) of the $4s$ electron, sending the atom to the $4p_{3/2}15d$ autoionizing state [11].

The short duration of the 200 fsec laser pulse drives excitation to *only* states with $4p_{3/2}15d$ character, ensuring minimal mixing between states during the pulse. The $4s15d$ electron lies $\sim$ 560 cm^{-1} from the continuum, meaning the 25445 cm^{-1} laser pulse puts the autoionizing state $\sim$ 3.1 eV above the first ionization limit of calcium. The large energy contained in the atom ensures rapid ionization.

The atom does not simply autoionize through its interaction with the $4s^+$ Rydberg channel. The energy level diagram for calcium shown in Figure 7.4 shows some of the states that interact with the $4p_{3/2}15d$ state. Because the short pulse has a broad frequency spectrum ($\sim$ 75 cm^{-1}), the autoionizing state is excited over a range of energies, producing a non-stationary two electron wavepacket. There are several different electronic configurations for the electron pair to scatter into, some of which are bound. There are several singly and double excited modes available to the wavepacket which converge to an ionic state, including Ca^+ $4s_{1/2}$, $3d_{2/3}$, $3d_{5/2}$, $4p_{1/2}$, and $4p_{3/2}$ channels. The ability to monitor the time-dependent population of each available two-electron configuration would completely describe the system, but the limits of currently available technology prevents us from doing this. By monitoring the initial state ($4p_{3/2}15d$) character of the wavepacket as a function of time, however,

we obtain a significant amount of information about the electron dynamics.

7.3.1 Optical Ramsey Method

The optical Ramsey method is used to monitor the population of a state in an atom as a function of time [14, 15, 13]. As a brief interlude, this method is described as it is used in monitoring the evolution of a radial wavepacket made up of several adjacent Rydberg states. A $4snd$ radial wavepacket, with mean principle quantum number $N = 25$, is excited in calcium using the excitation scheme described in Chapter 4. Using the impulsive momentum retrieval method, we observed breathing motion in the radial wavepacket's momentum distribution when the wavepacket is localized. The distribution is narrowest when the wavepacket is basically stopped at its outer turning point, and spread out when the wavepacket is moving quickly near the ionic core. Localization of the radial wavepacket is also observable using the optical Ramsey method, in which we detect how much the wavepacket resembles itself as it was just after excitation, when it was localized near the core. The technique uses two short, identical laser pulses. The first pulse excites a wavepacket and the second either excites another wavepacket or de-excites the original wavepacket [15]. The total Rydberg wavepacket population after the second pulse depends on the phase difference between the two pulses. Monitoring the population of the atom in the initial state provides the initial state character of the wavepacket as a function of time.

The interference between the two wavepackets occurs at the optical frequency of the short laser pulse that excites the wavepacket(s), which is about 2000× the orbital frequency of the wavepacket. Therefore, a continuous measurement of the time dependent $4snd$ wavepacket population throughout the lifetime of the wavepacket requires

a prohibitively large amount of data to be able to observe the interference fringes. There are several methods to determine the final probability of the wavepacket being in its initial state while simultaneously bypassing the need for a continuous measurement.

A non-linear root-mean-square (RMS) signal average taken at many time steps (large relative to the optical period, but small compared to the wavepacket's evolutionary time scale) can be used to extract temporal dynamics of the system [16], but is susceptible to large uncertainties in relative amplitudes between signal features because of the indistinguishability from noise in the signal. A second method involves phase-locking between the two excitation pulses, restricting measurements to be made only when there is a well defined phase difference between the two pulses [15], but this requires simultaneous phase measurements throughout the experiment, which can pose experimental difficulties and requires special equipment.

We are able to observe the long-term behavior of the wavepacket, however, by considering many high-resolution time scans over a small time range (micro-delays which are sensitive to optical frequency interference) that are separated by larger time steps [10] (macro-delays, which are sensitive to the wavepacket dynamics time scale). The strength of the interference pattern at each macro-step is directly related to how strongly the wavepacket resembles the initial $4snd$ wavepacket localized near the core. The Fourier transform of each micro-time scan provides the strength of the interference (hence resemblence of the wavepacket to its initial state) at the excitation frequency, and the record of the strength at each macro-delay generates an interferogram showing the temporal dynamics of the wavepacket [10].

The single-shot detector has been configured to make data acquisition over both time scales possible with simply a macro- delay-step scan [17]. As shown in Figure

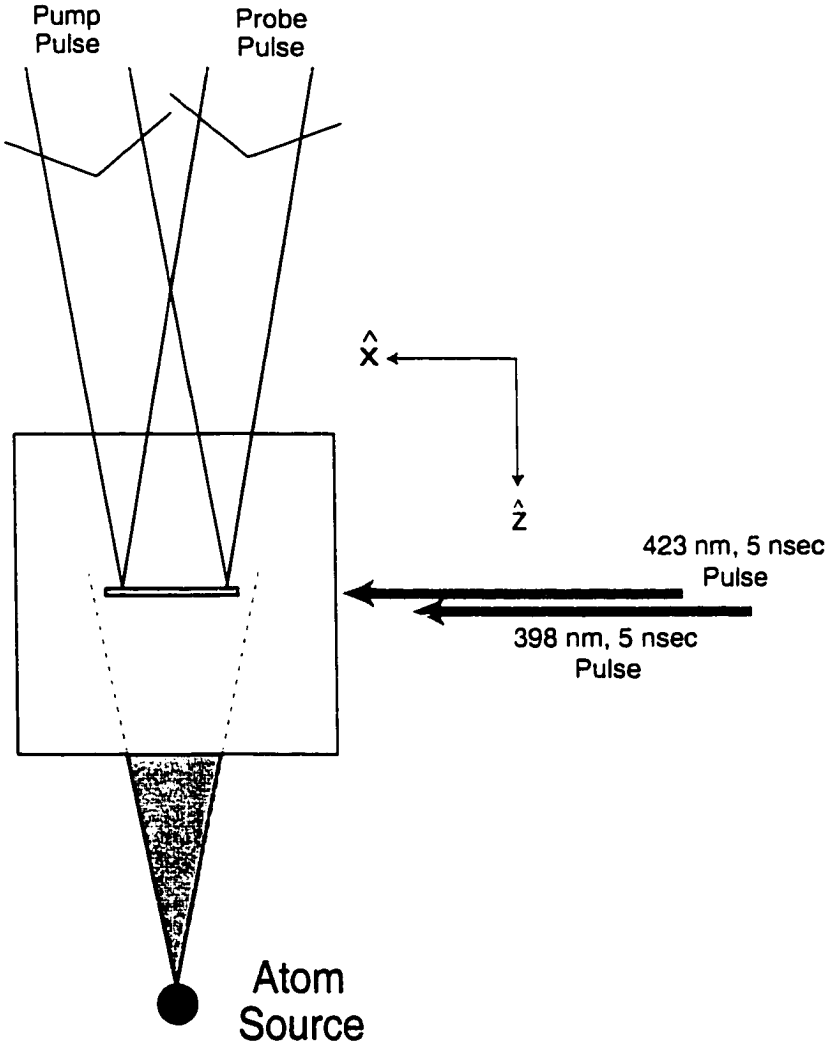

Figure 7.5: Experimental schematic diagram. The relative angle between the pump and probe beams is greatly exaggerated. In actuality, the beams are nearly co-linear, resulting in a ~ 5 fsec delay range for the window with each pump-probe pair.

7.5, a dye laser pulse propagating along the $\hat{x}$ axis, which follows the long dimension of the slit, uniformly excites a portion of the thermal calcium beam to the $4s4p^1P_1$ intermediate state. A $4snd^1D_2$ wavepacket, with $N = 25$, is excited with a 200 fsec, 393 nm laser pulse propagating along the $\hat{z}$. A second, identical short pulse traveling nearly parallel to the first short pulse excites a second wavepacket in the sample of calcium atoms. The two short pulses are the result of a single 786 nm, $\sim$ 120 fsec, $\sim$ 1 mJ optical pulse split into two portions with a Michelson interferometer and sent through a 2 cm $\times$ 1 cm $\times$ 1cm KDP doubling crystal. The interferometer is slightly mis-aligned, so the two short pulses enter the atom/laser interaction region with a very small relative angle of propagation. Atoms separated by 1 inch along the $\hat{x}$ axis have a relative delay difference between the two pulses of about 5 fsec. One leg of the Michelson interferometer is placed on a translation stage with its position controlled by a high-precision Burleigh stepper motor. For each macro time delay between the two short pulses as determined by the interferometer, we observe a micro-delay range with the imaging detector. The short pulses are sent through a diverging cylindrical lens to spread the beam intensity over the entire length of the slit.

A ($\sim$ 2.5 kV) high-voltage pulse is applied to the bottom field plate to ionize any Rydberg wavepacket population, sending the ions to the imaging detector with the relative spatial separation intact. The ionization levels over the 5 fsec delay range is recorded at each macro time step. A single line of the CCD video output is averaged 100$\times$ at each macro time step. The wavepacket excitation pulse is not uniformly bright across the micro-delay window. To account for this, the Rydberg state signal is recorded while one of the Michelson interferometer legs is blocked. A similar trace is recorded while the other leg is blocked and these two traces are averaged together to give the time-independent atomic response to the excitation pulses. Subsequent

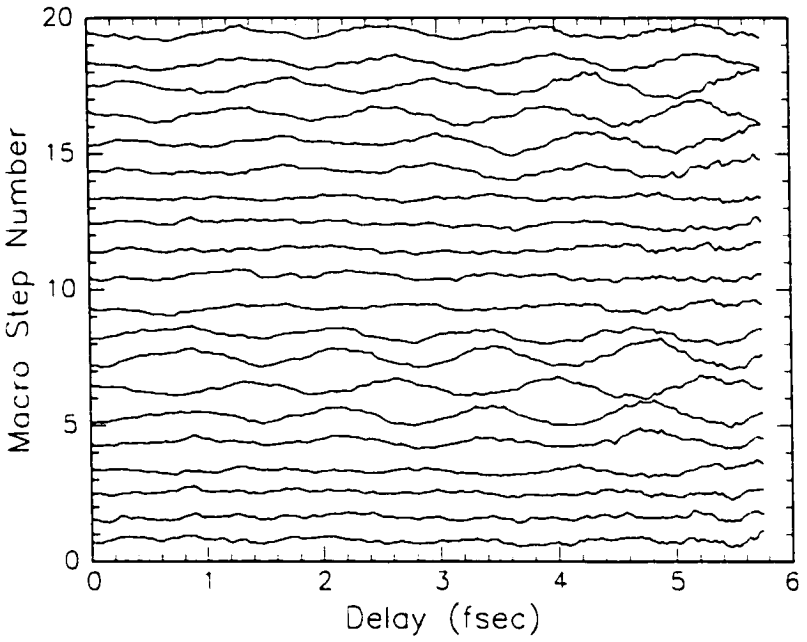

Figure 7.6: Ramsey fringe pattern at a sequence of macro delay steps separated by 0.1 psec. The Fourier transform is taken of each curve and the amplitude at the optical frequency is recorded at each macro step.

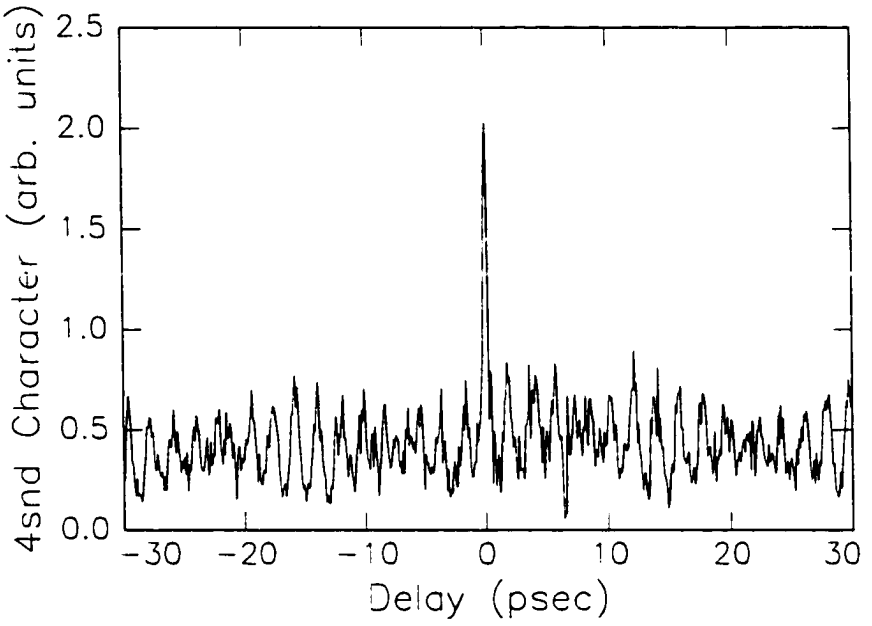

Figure 7.7: Interferogram for a radial wavepacket in calcium with three n-states significantly contributing, centered on $n = 25$. The oscillations represent the localized wavepacket moving towards and away from the ionic core.

measurements are then divided by the response trace, giving the true time-dependent atomic response to the pair of optical pulses.

The probability of Rydberg population oscillates with a period of $\sim$ 1.3 fsec, and the strength of the oscillation demonstrates how strongly the wavepacket excited at some time $t = \tau$ resembles the wavepacket at $t = 0$. Figure 7.6 shows the Ramsey interference pattern for a series of consecutive macro ($\sim$ 0.2 psec) time steps . The oscillations vary between strong and weak, depending on where the wavepacket is in its orbit when the second short pulse arrives. The average of four video images of the phosphor screen showing the wavepacket probability oscillations at the excitation frequency is shown in Figure 3.3.

An interferogram is generated over a large delay range by taking the Fourier transform of each micro-delay curve and tabulating the strength of the optical frequency

peak at each macro-delay step. The Fourier transform offers much better signal to noise than a RMS method because we automatically exclude the signal contributions to high and low frequency noise. Figure 7.7 shows a plot of the relative strength of the Ramsey fringe oscillations at the optical frequency of the wavepacket excitation pulse as a function of delay between the two pulses. The excitation pulses overlap in time for about 1 psec (producing the large spike at $t = 0$), therefore any Ramsey fringes observed at longer delays are the result of the atomic response of the calcium atoms to the optical pulse pair. The interference of two $4snd$ radial wavepacket is purely a quantum mechanical effect in an atom whose dynamic electronic probability distribution was described *very well classically* in Chapter 4. It should be noted that the strong interference pattern observed when the two pulses are overlapped in time has a period of the 2.6 fsec. This is the period of the optical pulses before they are frequency doubled in the KDP crystal.

The radial wavepacket has about 3 significantly contributing n-states, centered on $n = 25$, $n^* = 23.87$. Because its made up of only a few states, the wavepacket spends a large fraction of its lifetime localized in space. Oscillations at the Kepler period ($\tau_{Kepler} = 2.1$ psec) are prominent throughout the interferogram, with the relative height demonstrating the $4snd$ character of the wavepacket, basically showing $|\langle\Psi(t = 0)|\Psi(t = \tau)\rangle|^2$. A full revival of the wavepacket is observed near $t \approx \pm 14$ psec. In this experiment we probe the evolution of the wavepacket when it is near the atomic core, where the approximations used in the IMR method break down.

7.4 Autoionization Measurement and Analysis

Using the optical Ramsey Method described above, we monitor the $4p_{3/2}15d$ character of the autoionizing wavepacket as a function of time. In this experiment, a

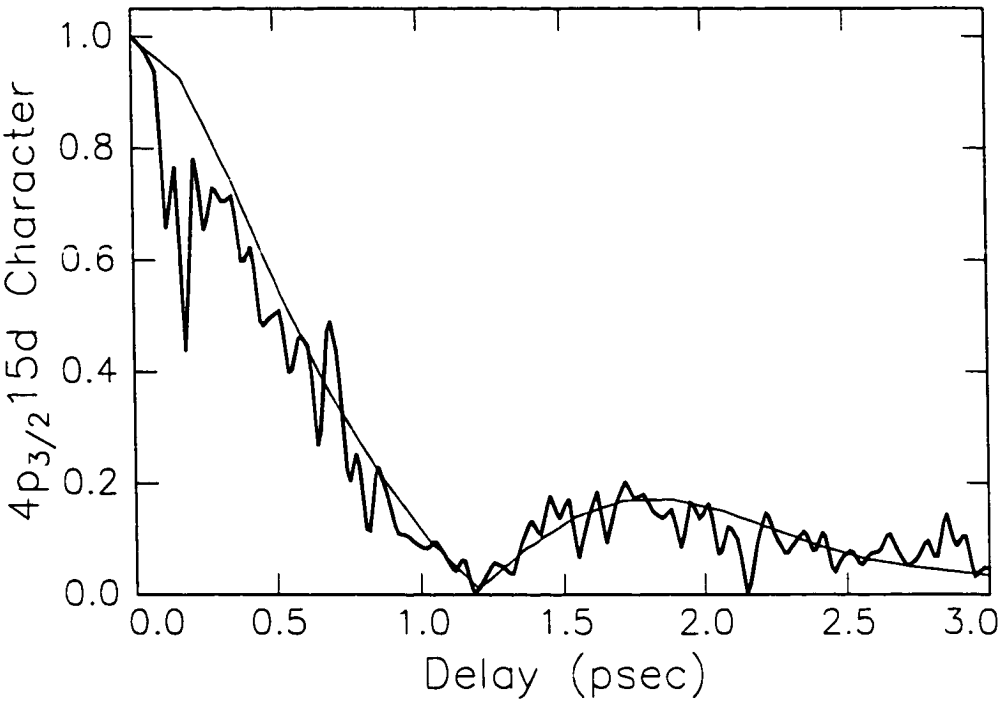

Figure 7.8: Time-dependent $4p_{3/2}15d$ character during the autoionization process. The bold line shows the optical Ramsey method interferogram, which matches the Fourier transform of the ICE transition spectrum. The initial state character drops to zero at $\tau = 1.2$ psec, but a 20% revival occurs at ~ 1.8 psec.

shorter 1 mm × 10 mm × 10 mm KDP doubling crystal is used, so the short optical pulse is $\sim$ 200 fsec long. This minimizes state configuration mixing to occur during wavepacket excitation, as well as minimizing the delay range over which the two pulses are overlapped in time. A $\sim$ 50 V pulse is applied to the bottom field plate to extract any ions formed by autoionization. A fringe measurement is made at each Michelson interferometer step of $5\mu m$, corresponding to a delay of 0.033 psec. To prevent a saturation in the signal which would destroy our ability to make relative fringe amplitude measurements we monitor the power in the short pulse, maintaining a power of ~ 80 μJ.

The Ramsey interference amplitude for the autoionizing wavepacket is plotted as

a function of delay between two pulses driving the ICE transition in Figure 7.8. The $4p_{3/2}15d$ character of the wavepacket drops to zero in 1.2 psec. and a $\sim$ 20% revival is observed at about 1.8 psec. There is a constant background subtracted off the interferogram which is a result of limited resolution in extracting the frequency components of the Fourier transform. An exponential decay of the $4p_{3/2}15d$ state to either the $4s$ or $3d_{3/2,5/2}$ continua would be expected if only one bound state configuration was available to the wavepacket. In calcium, however, there are multiple bound state configurations for the wavepacket to occupy before it ionizes. Once in a continuum channel, however, one electron rapidly leaves the atom, preventing any subsequent rescattering into bound modes.

Shortly after creation, the electrons scatter into other bound and unbound channels, quickly depleting the initial $4p_{3/2}15d$ character of the wavepacket. The $4p_{3/2}15d$ wavepacket couples with the degenerate $4p_{1/2}nd$ bound configurations, with n = 19 or 20. Because the wavepacket is localized, the initial state is entirely depleted at τ = 1.2 psec. A fraction of the population in the bound $4p_{1/2}nd$ configuration, however, transfers back into the $4p_{3/2}15d$ state. The 20% revival near 1.8 psec into the wavepacket's evolution demonstrates the return of the wavepacket to its initial state after spending time in other bound channels. Subsequent oscillations between bound state configurations are suppressed due to the rapid autoionization process, which lasts about 3 psec.

The time-domain measurement is compared to a measurement made in the frequency domain. It has been shown experimentally and theoretically that the Fourier transform of the frequency dependence of the excitation spectrum is equivalent to the time- domain bound state interferogram [12]. The measurements quantitatively agree at times greater than 200 fsec, at delays when the two optical pulses are not directly

overlapped. The finite 'turn-on' of the wavepacket means there is a small probability of having the character of other channels present in the wavepacket at $t = 0$.

The frequency measurement is made by exciting the $4s15d$ Rydberg state with a pair of dye-lasers, then scanning a third dye-laser (which has a bandwidth of ~ 1 cm^{-1}) over the $4p_{3/2}15d$ autoionizing state. In this case, it seems careful measurement of the frequency spectrum of the autoionizing state is simpler technique than working in time-domain. Measurements of more complicated systems, however, (such as wavepacket excitation of the first electron before ICE), depend on the ability to work in the time-domain.

7.5 Conclusions

Using the optical Ramsey method, we have directly observed the oscillation of electron population between bound autoionizing states. Electron population excited to the (nearly) pure $4p_{3/2}15d$ autoionizing state transfers into the $4p_{1/2}n'd$ ($n' = 19, 20$) bound states due to the coherent mixing between bound states. This is apparent in the interferogram with the distinct drop to zero and 20% revival of the $4p_{3/2}15d$ character. Temporal beating between bound states has previously been observed in the time, but not when the beating is quickly damped out by the occurence of strong mixing with continuum states.

The ability to monitor the dynamics of a two electron wavepacket in the time domain has been greatly facilitated with the use of the single-shot delay-range imaging detector. The experiments described in this Chapter were actually the first experiments to be performed with the detector, and quantitative agreement between its time-domain measurements with frequency domain measurements gave us great confidence in its capabilities. Again, the real-time feedback of the interference pattern

accelerates the experimental process, making it easy to optimize the alignment of the wavepacket excitation lasers to fix a proper micro-delay window. This real-time capability in studying wavepacket dynamics of complicated two-electron systems is a great benefit in the goal of quantum control of atoms and molecules. The work presented in this Chapter prompted further studies of controlling electron dynamics in a rapidly autoionizing atom with its response to short laser fields [18]

We have basically considered the quantum nature of calcium atoms in this Chapter, barring the simplistic image of the autoionization process. The localized radial wavepacket discussed in Chapter 4 was viewed as a classical particle orbiting the nucleus in a $1/r$ potential. We considered the quantum characteristics of a radial wavepacket when considering its complex state amplitudes, but we generally focussed on a classical description. Here, we monitor the dynamics of a wavepacket by beating two identical wavepackets together in a single atom. Using a purely quantum mechanical effect, the wave nature of electrons, we observe the dynamics of Rydberg wavepackets. Which we then, in turn, explain with insightful classical descriptions. Throughout the study of Rydberg wavepackets, the descriptions of atomic phenomena are referred to as semi-classical, meaning quantum restrictions are applied to classical particles. The scattering of two electrons in an atom producing a free electron and ion in the autoionization process is no exception.

Bibliography

[1] Thomas F. Gallagher, *Rydberg Atoms*, Cambridge University Press (1994).

[2] W.E. Cooke, T.F. Gallagher, S.A. Edelstein and R.M. Hill, *Phys. Rev. Lett.* **40**, 178 (1978).

[3] G.M. Lankhuijzen and L.D. Noordam, *Phys. Rev. Lett* **76**, 1784 (1996).

[4] J.B.M. Warntjes, C. Wesdorp, F. Robicheaux and L.D. Noordam, *Phys. Rev. Lett.* **83**, 512 (1999).

[5] M. Strehle, U. Weichmann and G. Gerber, *Phys. Rev. A* **58**, 450 (1998).

[6] W.E. Cooke and C.L. Cromer, *Phys. Rev. A* **32**, 2725 (1985). B.J. Lyons, D.W. Schumacher, D.I. Duncan, R.R. Jones and T.F. Gallagher, *Phys. Rev. A* **57**, 3712 (1998). S.A. Bhatti, C.L. Cromer and W.E. Cooke, *Phys. Rev. A* **24**, 161 (1981).

[7] D.W. Schumacher, D.I. Duncan, R.R. Jones and T.F. Gallagher, *J. Phys. B: At. Mol. Opt. Phys* **29**, L397 (1996).

[8] D.W. Schumacher, B.J. Lyons and T.F. Gallagher, *Phys. Rev. Lett* **78**, 4359 (1997).

[9] Warren S. Warren, Herschel Rabitz and Mohammed Dahleh, *Science* **259**, 1581 (1993).

[10] Michael W. Noel and C.R. Stroud, Jr., *Phys. Rev. Lett.* **77**, 1913 (1996).

[11] R.R. Jones, *Phys. Rev. A* **58**, 2608 (1998).

[12] R.R. Jones, D.W. Schumacher, D.I. Duncan, T.F. Gallagher and P.H. Bucksbaum, *J. Phys. B: At. Mol. Opt. Phys* **28**, L405 (1995). R.R. Jones and L.D. Noordam, *Advances in Atomic, Molecular and Optical Physics* **38**, 1 (1997).

[13] L.D. Noordam and R.R. Jones, *J. Mod. Opt.* **44**, 2515 (1997).

[14] R.R. Jones, C.S. Raman, D.W. Schumacher and P.H. Bucksbaum, *Phys. Rev. Lett.* **71**, 2575 (1993).

[15] N.F. Scherer, A.J. Ruggiero, M. Du and G.R. Fleming, *J. Chem. Phys* **93**, 856 (1990).

[16] B. Broers, J.F. Christian, J.H. Hoogenraad, W.J. van der Zande, H.B. van Linden van den Heuvell and L.D. Noordam, *Phys. Rev. Lett* **71**, 344 (1993).

[17] M.B. Campbell, T.J. Bensky and R.R. Jones, *Optics Express* **1**, 197 (1997).

[18] R. van Leeuwen, M.L. Bajema and R.R. Jones, *Phys. Rev. Lett.* **82**, 2852 (1999).

Chapter 8

Conclusions

The creation and detection of electronic wavepackets is a topic of great interest because of its relevence to understanding the response of atoms to intense radiation fields, exploring the quantum-classical boundary, and manipulating electronic wavefunctions. A summary of the experimental results from studying a variety of Rydberg wavepackets in calcium atoms and a brief discussion of future projects is presented here.

Single-Shot Detector

The developoment of the delay-range imaging detector has proven experimentally invaluable. Not only has this detector reduced data acquisition time by a few orders of magnitude, real-time feedback of wavepacket dynamics has greatly facilitated day-to-day maintenance of each project. The recent addition of a detector-CPU interface with real-time frame grabbing adds to the detector's experimental capabilities. A range of two experimental parameters can be observed with each laser shot using two-dimensional video image processing, indicating more complicated atomic systems can be studied.

Radial Wavepackets

Radial wavepackets are very well understood dynamic systems and serve as atomic laboratories to study our measurement techniques. We have extracted the time-dependent probability distribution of a radial wavepacket using the impulsive momentum retrieval (IMR) method. This method assumes the interaction between a half-cycle pulse (HCP) and the wavepacket is classical [1]. Because of the inherent simplicity of a radial wavepacket, we have directly observed the limitations of the IMR method by contrasting our measurement with both quantum and classical simulations. The probability distribution is accurately determined over most of the wavepacket's trajectory but is distorted when the wavepacket is highly localized and moving quickly by the atomic core. Near the core, the wavepacket does not have its usual Rydberg characteristics, and it would be easy to think the discrepency between our measurement and the actual distribution results from the quantum nature of the wavepacket. However, a classical calculation demonstrates the probability distribution resembles our measurement when a finite width HCP "impulse" is considered.

We have also determined the quantum state of a Rydberg wavepacket, which is a complete measurement of the system. The evolution of the wavepacket is recovered using the complex amplitudes of the constituent eigenstates in conjunction with the well known Rydberg eigenfunctions. Our capability to measure wavepacket dynamics with a single firing of the laser system indicates it should be possible to retrieve the quantum state of an electronic wavepacket in real time [2].

Stark Wavepackets

Knowing the capabilities and limitations of the IMR method, we have measured the full time-dependent momentum-space probability distribution for a complicated elec-

tronic dynamic system, a Stark wavepacket. Radial and orbital-angular momentum precessions, a periodic up-down asymmetry in the probability distribution, as well as strong oscillations in the electric dipole moment of the wavepacket are directly observed for the first time. We interpret the behavior of the wavepacket to explain the underlying physics of the system. Basically, a localized charge distribution feels an angular impulse at its the outer turning point of its orbit, which results in a cyclical "churning" of the charge distribution in the wavepacket. Our interpretation is supported by a classical calculation of the probability distributions of different angular momentum states. Again, we use classical reasoning to describe the behavior of a Rydberg wavepacket.

Oscillations in the electric dipole moment of the wavepacket at the Kepler frequency imply Stark wavepackets are potentially useful as sources of short pulses of THz radiation. A work in progress described in Appendix A uses Rydberg atoms as sensitive receivers of the FIR radiation [3] emitted by a sample of Stark wavepackets.

Continuum Wavepackets

The simple evolution of a wavepacket excited directly into the continuum with a short laser pulse has been monitored with HCPs. The impulse applied by a short, uni-polar electric pulse changes the momentum distribution of the continuum wavepacket and assists in the recombination of a fraction of the distribution with the parent ion. We have measured the recombination dependence on HCP amplitude and delay to find that the continuum wavepacket quickly moves away from the atomic core at a rate equal to a classical electron leaving a hydrogenic core in an unbound orbit. We have also measured the angular dependence of electron-ion recombination. The electron distribution has obvious *d*-state character, reminding us that the system (that is

described very well classically) has a wave nature explained by quantum mechanics.

Although quantum mechanical simulations of HCP assisted recombination and subsequent wavepacket dynamics are feasible [4], a classical picture is also appropriate. Classical calculations [5] show the probability distribution evolution of the recombined wavepacket periodically becomes highly localized in three dimensions. Arbitrary placement of charge about an atom is the essence of wavepacket manipulation [6], and our study of the interaction of continuum wavepackets with HCPs indicates we have developed a method to do just that using a sequence of HCP pulses. Future experiments can use a HCP probe to verify the interesting behavior of the recombined wavepacket.

Autoionizing Wavepackets

Autoionizing states are inherently dynamic systems and studying the evolution of an autoionizing wavepacket provides physical insight not necessarily available using MQDT. To this end, we consider an autoionizing wavepacket as a classical three-body system and ionization results from an electron-electron scattering event. The two valence electrons in calcium participate in the autoionization process. One valence electron excited to a Rydberg eigenstate, and the second electron is excited into a non-stationary state with a short laser pulse using isolated core excitation. The energy of the system is much greater than the single ionization limit, and energy and momentum is transferred between the two excited electrons until one of the electrons gains enough energy to leave the atom. Before complete ionization of the wavepacket population occurs, we observe population transfer between bound states, indicating population scatters to several degenerate states and not merely to the continuum. The measurement is made in the time domain and is compared to an equivalent measurement made in the frequency domain. The agreement between techniques

has prompted similar time domain measurements for more complicated autoionizing systems [7].

Quantum calculations will always describe these atomic systems well, but tabulating the huge number of relevent eigenstates is usually a difficult and cumbersome task and generally does not provide significant physical insight. Classical arguments, although incomplete, provide insightful pictures of interesting non-stationary atomic systems. Overall, the experiments presented in this thesis have added to the solid foundation of the understanding of the excitation of dynamic systems in atoms and the detection of their subsequent motion. Whether considering short optical pulses, applied static fields or HCPs of THz radiation, several aspects of this research are potentially useful in controlling atomic systems with electromagnetic radiation.

Bibliography

[1] R.R. Jones, *Phys. Rev. Lett.* **76**, 3927 (1996).

[2] The quantum-state of an electronic has been determined using a well-characterized reference wavepacket as described by T.C. Weinacht, J. Ahn and P.H. Bucksbaum, *Phys. Rev. Lett.* **80**, 5508 (1998), but the complexity of their technique makes real-time measurements unlikely.

[3] Theodore W. Ducas, William P. Spencer, A. Ganesh Vaidyanathan, William H. Hamilton and Daniel Kleppner, *Appl. Phys. Lett.* **35** 382 (1979). C. Raman, M.F. DeCamp, and P.H. Bucksbaum, *Optics Express* **1**, 186 (1997). J.H. Hoogenraad, R.B. Vrijen and L.D. Noordam, *Phys. Rev. A* **57** 4546 (1998).

[4] F. Robicheaux, *Phys. Rev. A* **60**, 431 (1999). F. Robicheaux and J. Shaw, *Phys. Rev. A* **56**, 278 (1997).

[5] Tom Bensky, private communication.

[6] M.W. Noel and C.R. Stroud, Jr., *Phys. Rev. Lett.* **77**, 1913 (1996).

[7] R. van Leeuwen, M.L. Bajema and R.R. Jones, *Phys. Rev. Lett.* **82**, 2852 (1999).

Appendix A

Using Stark Wavepackets as Short THz Pulse Generators

A.1 Introduction

The measurement of the time-dependent probability distribution for a Stark wavepacket described in Chapter 5 allowed us to directly observe rapid oscillations in the electric dipole moment of the wavepacket at the Kepler frequency. Any oscillating electric dipole emits radiation, implying a sample of Stark wavepackets is potentially a novel source of THz radiation.

The frequency spectrum of the radiation emitted by a Stark wavepacket is centered on the wavepacket's Kepler frequency. In our case the eigenstates of the wavepacket are centered on $n = 28$, $n^* = 26.8$, and the dipole moment oscillates over ~ 4 full cycles, producing a ~ 10 psec far-infrared (FIR) pulse centered on 0.33 THz = 11 cm^{-1}. Figure 5.19 shows the full frequency spectrum of the FIR pulse generated by the Stark wavepacket.

Because of the close spacing between nearby eigenstates, Rydberg atoms are good candidates as FIR radiation detectors. Several experiments have shown that population can be redistributed from a Rydberg eigenstate into nearby Rydberg states with

FIR radiation [1]. However, sources of short pulses of FIR radiation are not common. A photoconductive switch (a biased GaAs wafer) illuminated by a temporally shaped optical pulse produces a $\sim$ 150 psec pulse with a frequency centered at 12 cm^{-1} [2]. This technique is appealing because the radiation source is small and accessible, although the bandwidth is limited by the 150 psec duration of the pulse. Alternatively, a free-electron laser is capable of producing strong, continuously tunable picosecond FIR pulses over a frequency range between 3 THz (90 cm^{-1}) and 60 THz (2000 cm^{-1}) [3]. Despite their attractive capabilities, the accessibility of free-electron lasers is limited, and a "table-top" source of broadband FIR pulses is desirable.

We have considered using population redistribution from Rydberg eigenstates to probe the THz emission from Stark wavepackets. It is prudent to consider the likelihood of success of this endeavor. Each Stark wavepacket in a volume of atoms is emitting THz radiation, and we estimate the density of Stark wavepackets necessary to transfer population between two Rydberg eigenstates. First, the radiated field of a single oscillating electric dipole is calculated (in MKS units) using

$$E(r,\theta,t) = \frac{\mu_o}{4\pi}\ddot{p}(t)\frac{\sin\theta}{r}\hat{\theta}[4], \tag{A.1}$$

where p_o is the dipole moment and r is the distance away from the dipole. Taking out the time and angular dependence, we get,

$$E = \frac{\mu_o \omega^2 p_o}{4\pi}\frac{1}{r}. \tag{A.2}$$

Assuming p_o = 50 a.u., $\omega = \frac{2\pi}{\tau_{Kepler}}$ = 0.33 THz and r = 10 cm, the radiated field from a single Stark wavepacket is $E = 1.4 \times 10^{-11}$ V/cm/atom.

Second, we need to calculate the field strength for a π-pulse that will transfer population between two closely spaced Rydberg eigenstates, the $4s20s\ ^1S_0$ and the

$4s20p\ ^1P_1$ states. These two states were chosen because their separation in energy is similar to the energies in the THz pulse produced by the Stark wavepacket.

The field is found with.

$$\tau = \frac{\pi}{Z_{1,2}}. \tag{A.3}$$

where τ is the duration of the pulse and $Z_{1,2}$ is the perturbation matrix element of the pulse field strength.

$$Z_{1,2} = < 20p|E_o z|20s > = \frac{3}{2} E_o n\sqrt{n^2 - \ell^2}. \tag{A.4}$$

For a $\tau = 10$ psec pulse, we find $E_o \approx 65$ V/cm.

The total number of Stark wavepackets an average of 10 cm away from a volume of $4s20s$ Rydberg atoms necessary to completely transfer the population to the $4s20p$ eigenstate is $\sim 5 \times 10^{12}$ atoms. This is a very large number of Stark wavepackets, but is potentially attainable.

A.2 Experiment

Encouraged by these theoretical estimates, we attempted to observe THz emission from Stark wavepackets directly. Two atom-laser interaction regions are used in this experiment. One is housed between two elongated (15 cm × 5 cm) electric field plates and is the region in which a volume of Stark wavepacket is excited. The second is a region defined by two square (7.5 cm × 7.5 cm) electric field plates. Rydberg atoms are excited in this region and detected with a micro-channel plate detector positioned above the top field plate. Two atom-laser interaction regions are used because it's necessary to excite the Rydberg eigenstates in zero field and excite the Stark wavepackets in a strong electric field. Large Stark wavepacket population requires each interaction region to have its own atom source. Rydberg eigenstates

are produced in an effusive beam of calcium atoms emitted from a resistively heated stainless steel oven, as described in Chapter 2. A typical atom density from this source is $\sim 10^9$-10^{10} atoms/cm^3. Stark wavepackets are produced in a dense volume of calcium atoms ejected from a different oven arrangement. Calcium shot is packed into a resistively heated stainless steel tube, similar to the other oven, but this tube has seven equally spaced pinholes along one side from which the atoms are sprayed. The oven runs parallel to the long electric field plates of the Stark wavepacket interaction region and is separated by about 5 cm. These changes are made in an attempt to increase the atom density between the field plates.

The number of Stark wavepackets produced is equal to the atom density times the volume of atoms excited into a wavepacket. A 5 nsec dye-laser pulse, propagating along the long dimension of the field plates, excites the calcium atoms from the $4s^2$ state to the $4s4p$ state. A 2 mm diameter 392 nm, 1.5 psec laser pulse drives the atoms into a $4snd$ wavepacket. A schematic of the experimental setup is shown in Figure A.1

Stark wavepackets are excited over a $\sim$ 10 cm span along the interaction region, meaning a 1 cm^3 volume of atoms is used. The wavepacket density must be $\sim 5 \times 10^{12}$ atoms/cm^3 in the volume to attain the required emitted field amplitude. The volume of Stark wavepackets may be considered as acting like a single-pass amplifier, which reduces the estimated atom density. The dipole moment has begun oscillating in the atoms originally excited in the region before the excitation pulse has passed through the entire region. The 0.33 THz oscillations of the first excited wavepackets promote strong oscillations at the same frequency in the other Stark wavepackets, resulting in an increase in power in the FIR beam along the wavepacket excitation laser propagation axis. Assuming the radiation of each atom is emitted primarily

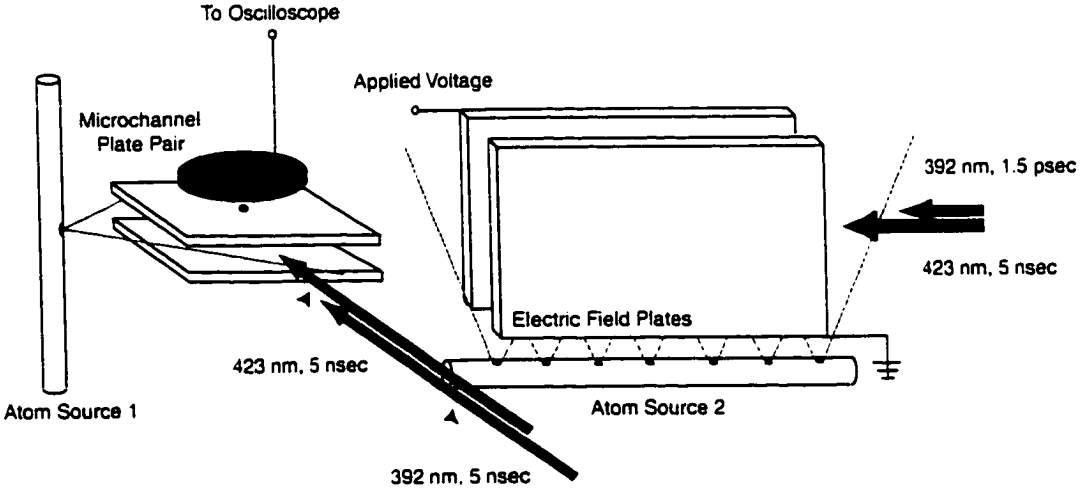

Figure A.1: Schematic of the experiment seeking Rydberg state population redistribution due to THz radiation emitted from Stark wavepackets. Two atom sources are necessary to reach high atom densities.

along the excitation laser axis, the net power along that axis increases by a factor of 4π.

The number of atoms emitted by the stainless steel oven increases non-linearly with temperature. Therefore, we estimate the atom density increases by at least a factor of ten when the current running through the stainless steel oven is increased 10-20%, bringing the density to a level where we expect to observe population redistribution in the sample of Rydberg eigenstates.

The laser beams exciting the Stark wavepacket pass through the second interaction region and we are able to measure the real amplitudes of the constituent eigenstates in the Stark wavepacket using state-selective field ionization (SSFI). The wavepacket

is centered on $n = 28$, so we are able to simultaneously observe $n = 20$ eigenstate population excited with two 5 nsec dye-lasers entering the interaction region from one side. The Stark wavepacket is excited approximately 10 nsec after the Rydberg eigenstates are populated.

We are able to resolve the $n = 20$, s, p and d eigenstates using SSFI by stretching the field ionization pulse and detecting electrons instead of ions. In an attempt to irradiate the Rydberg atoms with the strongest FIR pulse possible, we check to make sure both Rydberg state dye-laser pulses and the 1.5 psec pulse interact with the same volume of atoms. A blank index card is rotated between the two interaction regions to block the Stark wavepacket excitation laser pulses from entering the Rydberg state population. This filter should pass the THz radiation. Higher n-states of the wavepacket arrive at the detector at earlier times, and decrease the overall signal size of the $20s$ peak. The change in the Rydberg state population did not depend on any fields applied to the Stark wavepacket interaction region and may result from a lower amplification of the second burst of electron flux by the micro-channel plate pair. We have tested the power transmission of HCPs through index cards and have observed no decrease. We feel confident that the card will cleanly allow any THz radiation to pass to the Rydberg state sample.

With $4s20s$ eigenstates populated in the region beneath the detector, a 180 V/cm electric field is applied to the wavepacket interaction region. A high density of Stark wavepackets should emit enough radiation to observe some population redistribution in the $20s$ state. However, no redistribution was observed that could be attributed to radiation emitted by the Stark wavepacket sample.

Several changes were made to the experiment in the attempt to observe state redistribution. Two changes are very straight forward, yet equally unfruitful. First,

different initial Rydberg eigenstate were excited, ranging from the $4s18s$ to the $4s21d$. There may be more direct transitions at the frequency we are generating with the Stark wavepacket for different eigenstates. Nevertheless, we never saw Rydberg state redistribution. Second, an increase in atom density in both interaction regions was created by simply turning up the current flowing through each stainless steel oven. By raising the number of transmitters and emitters, we hoped to amplify any signs of population redistribution. A small level of redistribution appeared, but had no correlation to the electric field associated with the Stark wavepacket. Collisions and interactions between Rydberg atoms promotes redistribution as the density of the atoms increases, and this is all we observed.

A.3 Discussion

It is not clear why we did not observe population transfer out of a Rydberg eigenstate due to THz radiation emitted by a Stark wavepacket. The atom density in the region where Stark wavepackets are excited is very large and it would be difficult to believe we did not have a density between 10^{10} and 10^{11} atoms/cm^3. At one point a mini calcium stalactite formed on the metal heat shield above the Stark wavepacket interaction region and grew until it made contact with the biased field plate and shorted it out. Any furthur oven temperature increases resulted in high pressures in the vacuum chamber. The pressure in the vacuum chamber would rise to $\sim 3 \times 10^{-5}$ torr when the current through atom source two was greater than 75 Amps, and it's not clear whether this increase is due to a *really* large density of calcium atoms in the chamber or due to oxides and other materials "burning" off objects in the chamber from the hot oven temperature.

Clearly, with such a large volume of calcium atoms in the chamber, the index

card may have quickly become coated with the alkali earth metal and destroyed its ability to transmit any THz radiation. Other improvements to the experiment include changing the atom used for Rydberg state population. This allows for all laser beams to enter the Rydberg state interaction region and eliminates the need for the index card. Also, this experiment relies on strong electric dipole oscillations in the Stark wavepacket. In the configuration discussed above there is no way to determine if we are exciting exactly the wavepacket we desire. However cumbersome, a second vacuum chamber arranged to probe wavepacket dynamics with HCPs may be necessary to characterize the Stark wavepacket.

The physical simplicity of this experiment became overburdened with experimental pitfalls. Hopefully someone down the road will re-investigate the redistribution of Rydberg state population with THz radiation emitted by Stark wavepackets and have full success.

Bibliography

[1] Theodore W. Ducas, William P. Spencer, A. Ganesh Vaidyanathan, William H. Hamilton and Daniel Kleppner, *Appl. Phys. Lett.* **35**, 382 (1979). C.W. Fehrenbach, S.R. Lundeen and O.L. Weaver, *Phys. Rev. A* **51**, R910 (1995). N.E. Tielking and R.R. Jones, *Phys. Rev. A* **52**, 1371 (1995). G.M. Lankhuijzen, M. Drabbles, F. Robicheaux and L.D. Noordam, *Phys. Rev. A* **57**, 440 (1998).

[2] C. Raman, M.F. DeCamp and P.H. Bucksbaum, *Optics Express* **1**, 186 (1997).

[3] J.H. Hoogenraad and L.D. Noordam, *Phys. Rev. A* **57**, 4533 (1998). J.H. Hoogenraad, R.B. Vrijen and L.D. Noordam, *Phys. Rev. A* **57**, 4546 (1998).

[4] David J. Griffiths, *Introduction to Electrodynamics*, Prentice Hall, Englewood Cliffs, New Jersey (1989).